

**Reduction of CT dose for CT-based PET attenuation
correction**

Ting Xia

A dissertation
submitted in partial fulfillment of the
requirements for the degree of

Doctor of Philosophy

University of Washington

2012

Reading Committee:

Paul Kinahan, Chair

Matt O'Donnell

Bruno De Man

Adam Alessio

Program Authorized to Offer Degree:

Bioengineering

© Copyright [2012]

Ting Xia

University of Washington

Abstract

Reduction of CT dose for CT-based PET attenuation correction

Ting Xia

Chair of the Supervisory Committee:

Prof. Paul Kinahan

Department of Radiology

One important goal of quantitative imaging using positron emission tomography (PET) combined with X-ray computed tomography (CT) is to accurately measure a tumor's characteristics both before and during therapy to determine as early as possible the efficacy of the treatment. The transmission CT scans in the dual modality PET/CT are used for attenuation correction of the PET emission data.

Two significant challenges for quantitative PET/CT imaging come from respiratory motion in lung cancer imaging and estimation of the attenuation coefficients for high atomic number materials in bone imaging. Longer duration respiratory-gated CT has been proposed for attenuation correction of phase-matched respiratory-gated PET and motion estimation. Dual energy CT (DECT) has been proposed for accurate CT based PET attenuation correction (CTAC) for bone imaging. However, for both methods, the radiation dose from the CT scan is unacceptably high with the current CT techniques. This directly limits the clinical application of the quantitative PET imaging.

Ultra-low dose CT for PET attenuation correction is studied for lung cancer imaging. Selected combinations of dose reduced acquisition and noise suppression methods are investigated by taking advantage of the reduced requirement of CT for PET CTAC. The impact of these methods on PET quantitation is evaluated through simulations on different digital phantoms. When CT is not used for diagnostic and anatomical localization purposes, it is shown that ultra-low dose CT for PET/CT is feasible.

The noise and bias propagation from DECT acquisitions to PET or SPECT are studied for bone imaging, and related dose minimization are investigated. It is shown that through appropriate selection of CT techniques, DECT could deliver the same radiation dose as that of a single spectra CT and provide accurate attenuation correction for PET imaging containing high-Z materials.

Finally, phantom-based measured experiments are performed to characterize the simulation and provide spectra validation.

TABLE OF CONTENTS

List of Figures.....	viii
List of Tables.....	xii
Chapter I: Motivations and significance.....	1
1.1 PET/CT for cancer imaging	1
1.2 PET quantitation in oncology	3
1.2.1 Limitations of conventional techniques for evaluation of early response to therapy	3
1.2.2 Evaluation of response to therapy for lung cancer	5
1.2.3 Evaluation of response to therapy for bone cancer	6
1.3 Factors confounding PET quantitation.....	6
1.3.1 Impact of respiratory motion on quantitative lung imaging	7
1.3.2 Impact of dense materials on quantitative bone imaging	8
1.3.3 The need for longer duration CT or dual energy CT for PET attenuation correction	10
1.3.4 Concerns about CT radiation dose during PET/CT imaging .	13
1.4 Other modalities used in clinical for cancer imaging	17
1.4.1 Ultrasound	17
1.4.2 Endoscopic Ultrasound (EUS)	19

1.4.3. X-ray CT	21
1.4.4 MRI	22
1.4.5 SPECT and SPECT/CT	24
1.5 Organization of this dissertation	25
Chapter II: Background	27
2.1 PET physics.....	27
2.1.1 Major components of a PET/CT system	27
2.1.2 Positron Annihilation coincidence detection.....	29
2.1.3 Photon attenuation and correction in PET	31
2.1.4 PET processing steps other than for attenuation	35
2.1.5 Radiopharmaceuticals used for PET oncologic imaging	39
2.2 CT physics.....	40
2.2.1 Major components of a CT system	41
2.2.2 X-ray generation and detection.....	45
2.3 CT based PET attenuation correction.....	48
2.3.1 Principles of CT based PET attenuation correction for PET	50
2.3.2 Methods for CT based attenuation correction (CTAC).....	52
2.4 Radiation Dose	56
2.4.1 Terminology and the measurement standards.....	57
2.4.2 Biological effects of X-ray and PET radiation.....	62

Chapter III: Tool development.....	67
3.1 Introduction of CT simulator.....	67
3.2 Introduction of PET simulator	69
3.3 Development of tools for CATSIM	69
3.3.1 Generation of material files for CT contrast agent (iohexol) ..	70
3.3.2 Improvement of beam hardening correction function for multiple detector rows.....	72
3.3.3 Improvement of Poisson random number generator in FreeMat	72
3.3.4 Simulation of CATSIM with NCAT integration and contrast agent enhancement in the phantom	73
3.3.5 Modifications to CATSIM structure used for efficient generation of i.i.d. realizations	73
3.3.6 Sinogram pre-processing with CATSIM	76
3.4 Summary and desired future functionalities.....	77
Chapter IV: Ultra-low dose CT for PET attenuation correction.....	80
4.1 Introduction.....	80
4.1.1 Extended duration CT scans for PET/CT imaging requires ultra-low dose CT techniques	80
4.1.2 Constraints on CT system for CT radiation dose reduction...	83
4.1.3 General strategies for CT radiation dose reduction and	

bias/noise suppression	83
4.2 Materials and Methods	87
4.2.1 Simulation tool	87
4.2.2 Test objects	89
4.2.3 Data flow and parameters	90
4.2.4 Metrics	93
4.3 Results	96
4.3.1 The impact of acquisition parameters and spectral shaping on CT radiation dose reduction	96
4.3.2 The impact of CT sinogram smoothing	102
4.4 Discussion	111
4.5 Conclusion	117
Chapter V: Dual energy CT used for PET attenuation correction.....	119
5.1 Introduction.....	119
5.1.1 Problems of Interest.....	119
5.2 Materials and methods	121
5.2.1 Basis material decomposition (BMD).....	121
5.2.2 Analytical approximation to estimate noise properties in dual-energy derived sinograms	125
5.2.3 Simulation tools.....	126

5.2.4 Study of energy dependent noise and bias properties	130
5.2.5 DECT noise suppression and dose minimization for attenuation correction	131
5.2.6 Comparison of PET attenuation correction with dual- and single kVp– derived attenuation map	132
5.3 Results	136
5.3.1 Analytical approximation to estimate noise properties in dual-energy derived sinogram	136
5.3.2 Impact of beam conditioning and basis material coefficients	136
5.3.3 Study of energy dependent noise and bias properties	137
5.3.4 DECT noise suppression and dose minimization for attenuation correction	139
5.3.5 Comparison of PET attenuation correction with DECT and single kVp –derived attenuation map.....	140
5.4 Discussion	144
5.5 Conclusion.....	149
Chapter VI: Phantom-based measured experiments on spectra validation	150
6.1 Introduction.....	150
6.1.1 Problems of Interest.....	150
6.1.2 Investigation of spectra generators	151
6.2 Materials and Methods	153

6.2.1 Overview of the study	153
6.2.2 Phantom preparation	155
6.2.3 Experiment flow	159
6.2.4 Data processing and analysis	163
6.3 Results	166
6.3.1 Spectra comparison	166
6.3.2 Experiment results on spectra validation	168
6.3.3 Simulation results on spectra validation	169
6.3.4 Comparison of the two sets of spectra data	169
6.4 Discussion	171
6.5 Conclusion	172
Chapter VII: Summary and future work	174
7.1 Summary of contributions	174
7.2 Potential future directions	178
7.2.1 Simulation tool improvement for dose estimation	178
7.2.2 Simulation tool improvement with more accurate low-dose CT noise model	178
7.2.3 Evaluation of standard CT dose reduction techniques for various object sizes with simulation	180
7.2.4 Development of more advanced dose minimization and	

noise suppression strategies	180
7.2.5 Design practical protocols enabling low dose longer duration CT scans for quantitative PET imaging	181
Appendix A: Calculation and generation of CT contrast agent material files.....	196
Appendix B: Modified water-only beam hardening correction for multi-row CT detector	204
Appendix C: Measured experiments on low dose CT noise characterization.....	207

List of Figures

Figure 1.1 Respiratory motion effects on PET/CT.....	8
Figure 1.2 Effects of respiratory motion blurring on PET quantitation.	8
Figure 1.3 Example of patient's response to therapy.	9
Figure 1.4 Patient study showing the impact of extending the duration of the CINE CT scan	11
Figure 2. 1 Physics of positron decay and annihilation	29
Figure 2.2 Diagram of a basic PET detection system	30
Figure 2.3 Illustration of the three main coincidence event types.....	31
Figure 2.4 Example of PET scan with/without attenuation correction	32
Figure 2.5 Attenuation detection in PET	34
Figure 2.6 Attenuation in PET	34
Figure 2.7 Schematic illustration of data processing steps in X-ray CT systems.....	45
Figure 2.8 Anecdotal illustrations of the three transmission methods used for measured attenuation correction for PET	49
Figure 2.9 Mass attenuation coefficients for different materials as a function of energy	51
Figure 2.10 Using transmission X-ray CT imaging for attenuation correction of PET emission data.	51
Figure 2.11 Dual modality PET/CT structure.....	52
Figure 2.12 Multi-linear conversion of CT image values to linear attenuation coefficients for CT-based attenuation correction	54
Figure 2.13 A measured CT number can be invariant for changes in density vs. atomic properties	56

Figure 3.1 Chemical structure of iohexol.....	70
Figure 3.2 Overview of desired structure of CATSIM for multiple realizations.....	74
Figure 3.3 Original CATSIM structure flow.....	75
Figure 3.4 Modified CATSIM structure flow	76
Figure 4.1 Data processing flow used for the simulation studies	90
Figure 4.2 Sample images of the NCAT phantom	93
Figure 4.3 Spectra for three CT acquisitions with mean energy and relative photon flux transmission efficiency.....	97
Figure 4.4 CT and PET image roughness noise vs. CT absorbed radiation dose.	99
Figure 4.5 CT and PET image bias vs. CT absorbed radiation dose... ..	100
Figure 4.6 CT and PET image mean and RMSE of the water cylinder phantom.....	101
Figure 4.7 Detailed profile of sinogram after dark current subtraction in each processing step	104
Figure 4.8 Comparison of CT and PET bias as a function of CT tube current with and without sinogram smoothing	105
Figure 4.9 Profile through the reconstructed noise-free PET NCAT phantom.....	106
Figure 5.1 Normalized variance vs. synthesized energy for interested energy range.....	120
Figure 5.2 Dual energy CT processing step.....	122
Figure 5.3 Schematic illustration and simulation of x-ray image of step wedge used for BMD calibration.	130
Figure 5.4 ROIs of elliptical cylinder phantom with 30 cm × 20 cm cross-section.....	131
Figure 5.5 Modified version of the bilinear transformation used in the	

study	134
Figure 5.6 Data flow for evaluating use of DECT for PET attenuation correction.....	135
Figure 5.7 Normalized noise vs. synthesized energy of monoenergetic attenuation image	138
Figure 5.8 Isocontour plot of the radiation dose	139
Figure 5.9 Isocontour plot of coefficient of variation of DECT-derived attenuation map	139
Figure 5.10 Comparison of attenuation image at 511 keV.....	142
Figure 5.11 Comparison of PET images using DECT and single-kVp CT-based attenuation correction (AC) methods.....	143
Figure 5.12 Profile comparison of the reconstructed noise-free PET images	143
Figure 6.1 Graphic User Interface of SpekCalc program	153
Figure 6.2 The overview of the spectra validation study flow.....	154
Figure 6.3 PMMA phantom slabs.....	156
Figure 6.4 Aluminum phantom slabs.....	156
Figure 6.5 Heavy phantom holder.....	157
Figure 6.6 A series of counterweights used	158
Figure 6.7 The whole PMMA phantom aligned in the scanner bore....	161
Figure 6.8 Screen shot of the graphic user interface for visualization of the preprocessed raw data	164
Figure 6.9 Comparison of normalized spectra	167
Figure 6.10 Mean projection value vs. PMMA phantom thickness.....	168
Figure 6.11 Mean projection value vs. Al phantom thickness	169

Figure 6.12 The calculated relative error for the old spectra for PMMA phantom..... 170

Figure 6.13 The calculated relative error for the new spectra generated with Xspect for PMMA phantom..... 170

Figure 6.14 The calculated relative error for the old spectra for Al phantom..... 171

Figure 6.15 The calculated relative error for the new spectra generated with Xspect for Al phantom. 171

List of Tables

Table 1.1 Radiation doses from PET/CT and CT scans	13
Table 2.1 Key specifications of current commercial PET/CT scanners. .	28
Table 2.2 Overview of radiopharmaceuticals used for oncological PET studies	40
Table 2.3 Comparison of the three transmission methods used for measured attenuation correction for PET	49
Table 2.4 Conversion factors for effective dose estimation from DLP for different anatomies	62
Table 3.1 Contrast agent Omnipaque 300 ® diluted in water solution with varying concentrations.....	71
Table 4.1 Typical radiation doses from PET/CT and CT scans.....	82
Table 4.2 Potential methods for reducing CT radiation dose for CT-based attenuation correction.....	84
Table 4.3 Potential methods for CT noise and bias suppression.....	84
Table 4.4 ROI specification	94
Table 4.5 Mean energy and transmission efficiency comparison.	97
Table 4.6 At 5% PET bias, corresponding CT bias, CT image roughness noise, PET image roughness, and mean absorbed dose...	101
Table 4.7 The effects of different smoothing levels on the CT images of the NCAT phantom	107
Table 4.8 The difference images of the NCAT phantom simulated above with the noise-free no sinogram smoothing CT images	108
Table 4.9 Noisy PET reconstructed images and the Normalized RMSE (%) are shown for each category	109
Table 4.10 The difference image between noisy PET reconstructed images and the noise-free truth PET image.....	110
Table 4.11 Bias and noise results for increasing CT sinogram	

smoothing levels for the NCAT object.....	111
Table 5.1 Photon energies of common isotopes used in PET/CT and SPECT/CT Imaging.	121
Table 5.2 Comparison of bias and RMSE in the DECT and SCT derived attenuation images at 511 keV for the NCAT phantom.	142
Table 5.3 Comparison of noisy PET images with DECT and single kVp based attenuation correction (AC)	144
Table 6.1 The measured average thicknesses of each PMMA slab.....	158
Table 6.2 Details of protocol used for phantom scanning.....	163

ACKNOWLEDGEMENT

First of all, I would like to express my indebtedness and deep gratitude to my advisor, Prof. Paul Kinahan, without whom none of this dissertation would have been possible, for his kindness, guidance and continuous support. His unique insights into medical imaging and his great personality have taught me much more beyond the technical subject and will never be forgotten. I also wish to thank Dr. Adam Alessio, whose enthusiastic support in every possible aspect has helped me a lot.

During the entire research period, I have had the privilege of numerous discussions with Dr. Bruno De Man from the GE Global Research Center, whose illuminating ideas, technical assistance and kind support were of invaluable importance to me and are sincerely acknowledged. I appreciate the help from Prof. Matthew O'Donnell, for his valuable time and suggestions. I would like to thank the rest of my committee, Prof. James Bassingthwaite, and Prof. David Cobden for their precious time and help.

This work was part of an academia-industrial collaboration between the University of Washington and GE Global Research Center. During this collaboration, I had many discussions with many talented scientists and engineers from GE, to whom I would like to thank: Drs. Ravindra Manjeshwar, Evren Asma, Paul Fitzgerald, Jed Pack and Hwei Gao. I would also like to thank Drs. Patrick L Riviere, Jiang Hsieh, Jeffrey Fessler, James Colsher, Paul Segars and Bruce Whiting for their help.

I am grateful to Dr. Larry Pierce for his kind help and critical review of my previous papers for publication. This entire dissertation has been proof-read by

him. The phantom-based experiment was completed with the assistance from Mr. Darrin Byrd and Mr. Dan Schindler. I appreciate the help from other members in Imaging Research Laboratory at University of Washington as well, including Drs. Tom Lewellen, Lawrence MacDonald, Robert Miyaoka, Robert Doot and Robert Harrison.

Last but not the least, I would like to express my appreciation to my family for their spiritual support and unconditional love. I would especially like to thank my mother, Benyu Xu, who passed away in July 2011, after having fought with lung cancer for more than 3 years in China. However, even at the most difficult time before her passing, she encouraged me to focus on studies and strive for the healthcare of human beings. Her perseverance, optimism, and love impressed me deeply and will continue to inspire me through all my life. I would like to thank my father, Shengxi Xia, who took care of my mother in the most difficult times. I am grateful to my husband, Guangsheng Gu, for his love, help and saying “never give up” when I was confronted with challenges while so far away from my family.

This research was financially supported by NIH grants R01-CA115870, R01-CA160253, and the GE Global Research Center.

DEDICATION

This dissertation is dedicated to God, my parents and my husband. May the work in this dissertation bring glory to God's name.

Chapter I: Motivations and significance

The first chapter of this dissertation addresses the motivation and significance of this study.

1.1 PET/CT for cancer imaging

Positron emission tomography (PET) is a nuclear medicine imaging technique that permits visualization and measurement of physiologic and biochemical processes within various human organs. It was first invented in the early 1970s (Phelps *et al.*, 1975), as a tool mainly for neurological and cardiological, and later oncological research. The clinical application of PET in cancer was limited until increased computation capabilities permitted the rapid acquisition of tomographic whole-body PET images and the use of glucose analog, 18F-fluorodeoxyglucose (FDG) provided glucose metabolic imaging. However, the wide clinical adoption of PET in oncology was slow because the medical community was accustomed to staging and monitoring cancer progression by morphological imaging techniques. This situation changed dramatically with the introduction of integrated PET/CT imaging in the late 1990s (Weber *et al.*, 2008).

The integration of PET and CT provides precise localization of the lesions on the FDG PET scans within the anatomic reference frame provided by CT. In addition, the transmission CT scans are used for attenuation correction of the PET emission data (Kinahan *et al.*, 1998). This dual modality PET/CT scanning approach has shown great benefits since its inception. First of all, patients can receive a comprehensive diagnostic anatomical and

glucose-metabolic whole-body survey in a single imaging session with a significantly shorter duration than a standalone PET scan (Halpern *et al.*, 2004). The transmission scan is much slower in a standalone PET scanner than PET/CT scanner. Second, it allows oncologists and imaging specialists to navigate between structural and metabolic information without having to visually correlate separately acquired information from two modalities or use software-based image fusion algorithms (Kim *et al.*, 2005). Third, the combination of PET and CT provides diagnostic information of greater accuracy than PET or CT alone (Czernin *et al.*, 2007), which leads to improved patient management and outcomes. PET/CT offers sensitive detection of both nodal and distant forms of metastatic diseases, which is important for accurate staging, restaging, and treatment monitoring. The ever-growing body of evidence shows that PET/CT is a valuable tool in head and neck cancer, thyroid cancer, solitary lung nodules, lung cancer, breast cancer, esophageal cancer, colorectal cancer, lymphoma, melanoma and other tumor types. PET/CT improves the delineation of target tissues, which could be invaluable for patient-specific radiation treatment planning.

Newly developed tracers for monitoring cell proliferation and apoptosis allow PET/CT to provide unique insights into molecular pathways of diseases, which constitute a strong basis for an individually tailored therapy for tumor patients (Powles *et al.*, 2007). Its ability for quantitative imaging to assess individual response to therapy has received attention recently since it is critical to determine the best patient-specific treatment plan in a timely manner (Herrmann *et al.*, 2009; Wahl *et al.*, 2009).

1.2 PET quantitation in oncology

Since PET/CT imaging can measure metabolic changes, which are an effective indicator of response to therapy, there are increasing interests in PET quantitation in oncology (Herrmann *et al.*, 2009; Wahl *et al.*, 2009). Quantification of tumors is often measured as the standard uptake value (SUV) of FDG in the lesion of interest. Studies have indicated that FDG uptake value after completion of therapy is a strong predictor of patient survival in several solid tumors. Particularly in responding tumors, FDG uptake decreases markedly within the first chemotherapy cycle (i.e. 3–4 weeks after the start of therapy). Conversely, the absence of a measurable decrease in tumor FDG uptake after the first chemotherapy cycle has been found to predict lack of tumor shrinkage and poor patient survival (Weber, 2006). Thus, quantitative assessment of therapy-induced changes in tumor ¹⁸F-FDG uptake may allow the prediction of tumor response and patient outcome very early in the course of therapy. Treatment may be adjusted according to the chemosensitivity and radiosensitivity of the tumor tissue in an individual patient. Thus, ¹⁸F-FDG PET/CT quantitation has an enormous potential to reduce the side effects and costs of ineffective therapy for patients and to boost the efficiency of evaluating clinical trials of new therapies for pharmaceutical departments as well (Weber, 2005).

1.2.1 Limitations of conventional techniques for evaluation of early response to therapy

Evaluating the efficacy of anti-cancer treatment is important for medical decisions in practice as well as in clinical trials. However, a widely used standard for monitoring the effects of cancer therapy on solid tumors is the

evaluation of size changes measured from CT images. According to the Response Evaluation Criteria in Solid Tumors (RECIST) (Eisenhauer *et al.*, 2009; Kusaba and Saijo, 2000; Watanabe *et al.*, 2009). "Partial Response" corresponds to at least a 30% decrease in the sum of diameters of target lesions, taking as reference the baseline sum diameters. However, the fundamental approach of RECIST remains grounded in the anatomical, rather than functional, assessment of disease, so it has several limitations. Firstly, there would be long time lag after therapy (six months or more) necessary for anatomical changes to become evident. By then, if there is no response, time may have run out for other treatment options for the patient. Secondly, the patient may have undergone several months of ineffective but toxic therapy. In addition, morphologic evaluation can be inaccurate because of peritumoral scar tissue formation and edema, which can mask tumor regression (Weber, 2005). Besides that, sometimes, effective treatment may not directly lead to the shrinkage of tumor size, in which case tumor size is not a good measure of response.

Histopathological response often is used as the gold standard for the evaluation of imaging techniques. However, complete resection of the tumor is necessary for a valid histopathological response evaluation. Analysis of biopsy specimens does not provide reliable results because of tumor heterogeneity (Mandard *et al.*, 1994; Becker *et al.*, 2003). Thus, histopathologic response can usually be determined only after the completion of therapy and cannot be used to modify treatment.

While RECIST guidelines and histopathology provide important

standards for evaluating response, more effective methods by noninvasively and quantitatively imaging biochemical changes at an early stage provided by PET are needed to improve patient management especially with increasing therapeutic choices.

1.2.2 Evaluation of response to therapy for lung cancer

Lung cancer is the most common cause of death from cancer in both men and women in developed countries. The annual number of deaths from lung cancer is greater than the numbers of deaths from breast, colon, and prostate cancers combined. More than 150,000 patients died of lung cancer in 2004 (Bunyaviroch and Coleman, 2006). The 5-year survival rates currently are 16% in the United States and 5% in the United Kingdom. The use of PET has much promise as an aid to the noninvasive evaluation of lung cancer. There is now considerable evidence in the literature that ¹⁸F-FDG PET has added value to early assessment of lung tumor response to chemo- and radiotherapy (Weber, 2005; Hoekstra *et al.*, 2005). It is feasible to predict response and patient outcome after one course of induction chemotherapy during therapy. Studies have shown that the overall survival and progression-free survival were correlated highly with a metabolic response in PET, and a measurable change in tumor ¹⁸F-FDG uptake after the first cycle of chemotherapy is associated with a palliative effect of therapy (Weber, 2005). Thus, PET quantitative imaging for lung cancer is significant in determining the best patient-specific treatment plan in a timely manner and in sparing patients the morbidity and cost of ineffective treatments.

1.2.3 Evaluation of response to therapy for bone cancer

Bone is a common place for cancer to spread to, such as breast cancer, prostate cancer and lung cancer. Bone metastases cause pain and compromise the quality of life for a large portion of cancer patients (Nielsen *et al.*, 1991). Bone metastases are found in one third of all patients with recurrent disease. The incidence of bone metastases is significantly higher in well-differentiated and estrogen receptor–positive tumors (Alexieva-Figusch *et al.*, 1988; Coleman and Rubens, 1987; Kamby *et al.*, 1991; Schirrmeister *et al.*, 1999). At autopsy, bone metastases were found in 47% to 85% of patients who died from breast cancer (Schirrmeister *et al.*, 1999; Houston and Rubens, 1995). Early accurate detection and monitoring bone response to therapy has a significant effect on clinical management (Schirrmeister *et al.*, 1999). Both fluoride-18 and [18F]fluorodeoxyglucose can be used for PET evaluation of metastatic bone disease. F-18-Fluoride accumulates in areas of bone remodeling, and [18F]FDG is specific to tumor tissue (Clamp *et al.*, 2004). Quantitative PET has shown promise in monitoring bone metastasis response to therapy, which has been challenging to monitor with conventional modalities such as bone scans and MRI (Clamp *et al.*, 2004). It has been reported that the percentage change in FDG uptake with therapy showed strong correlation with the percentage change in tumor marker value for breast cancer bone metastases (Stafford *et al.*, 2002).

1.3 Factors confounding PET quantitation

As is already known, accurate quantitation of positron emission tomography (PET) tracer uptake levels in tumors is crucial for evaluating

response to therapy (Alessio and Kinahan, 2006). However, there are factors confounding PET quantitation for lung cancer imaging and bone imaging (Goerres *et al.*, 2003a; Bujenovic *et al.*, 2003; Nakamoto *et al.*, 2003; Nakamoto *et al.*, 2002; Visvikis *et al.*, 2003; Nehmeh *et al.*, 2003).

The biggest hurdle for accurate PET/CT quantitation in lung cancer imaging is caused by patient's respiratory motion, while the biggest hurdle in bone imaging is caused by estimation of the attenuation coefficients for high atomic number materials such as bone, metal, and contrast agents.

1.3.1 Impact of respiratory motion on quantitative lung imaging

Respiratory motion has an impact on PET/CT quantitation in lung imaging through two mechanisms: (1) Artifacts from mismatches between PET data and CT-based attenuation correction; (2) Respiratory motion blurring. Figure 1.1 and Figure 1.2 show the impact of respiratory motion on PET quantitation. Studies using phantom experiments with known true tumor maximum SUV value in motion-free images have shown that the maximum SUV value can be underestimated by as much as 75% and recovery coefficient can be as low as 0.2 in motion blurred images, depending on lesion size and motion amplitude (Park *et al.*, 2008; Pevsner *et al.*, 2005). It has been reported that by computer simulations, driven by ~1300 patient real-time positioning and respiratory monitoring (RPM) traces, respiratory motion could cause on average an underestimation of maximum SUV value by ~28%, and an overestimation of lesion volume by over 2-fold (Liu *et al.*, 2009).

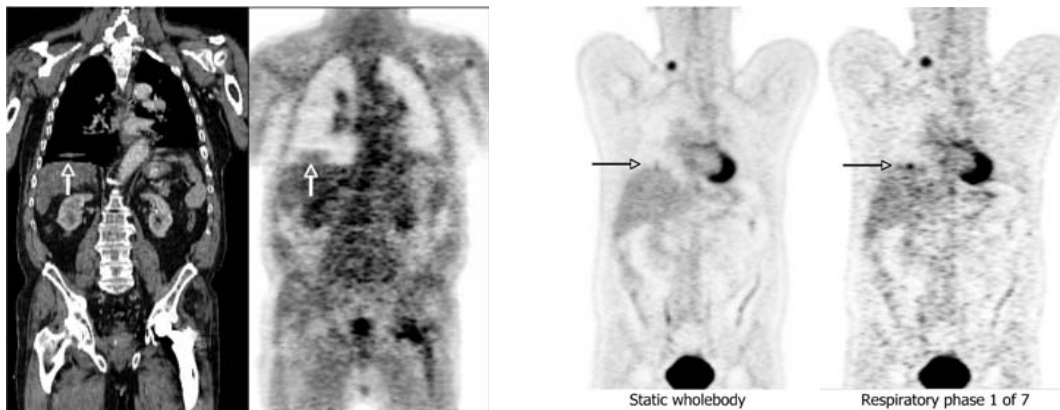


Figure 1.1 Respiratory motion effects on PET/CT. (Left) Artifacts in the CT image and/or mismatches between the CT and PET images propagates into PET image through CT based attenuation correction. (Image courtesy of Dr. Paul Kinahan)

Figure 1.2 Effects of respiratory motion blurring on PET quantitation. Respiratory motion blurs the PET image and reduces apparent tracer uptake levels in the PET image. (Image courtesy of Dr. Paul Kinahan)

1.3.2 Impact of dense materials on quantitative bone imaging

Attenuation coefficients for high atomic number materials such as bone, metal, and contrast agents from CT images could impact the PET quantitative accuracy. There are cases where quantitation (estimation) errors/bias arise with CT-based attenuation correction, which will propagate into the attenuation corrected image in a complex non-linear manner (Bai *et al.*, 2003a) While in many cases these errors/bias may not significantly affect diagnostic utility (Cohade *et al.*, 2003; Dizendorf *et al.*, 2003), they can affect decisions or therapies that depend on accurate estimation of tracer uptake value. Illustrative examples are given in Figure 1.3. Figure 1.3 is an example of the change in glucose metabolism and fluoride incorporation in bone-

dominant metastatic breast cancer of a patient before and after hormonal therapy. It shows that for F-18-fluoride, evaluation of response to therapy is largely dependent on the PET quantitation. Thus, accurate estimation of tracer uptake in the bone adjacent to tumor sites (e.g., [F-18]-fluoride imaging) is essential. There are similar issues in the application of FDG PET/CT to bony infections such as infections adjacent to total hip arthroplasty (Zhuang *et al.*, 2001; Chacko *et al.*, 2002; Zhuang *et al.*, 2002). Furthermore, in the presence of contrast agents and/or metallic implants near bony area, minimizing the bias from dense materials would be essential to ensure PET quantitative accuracy.

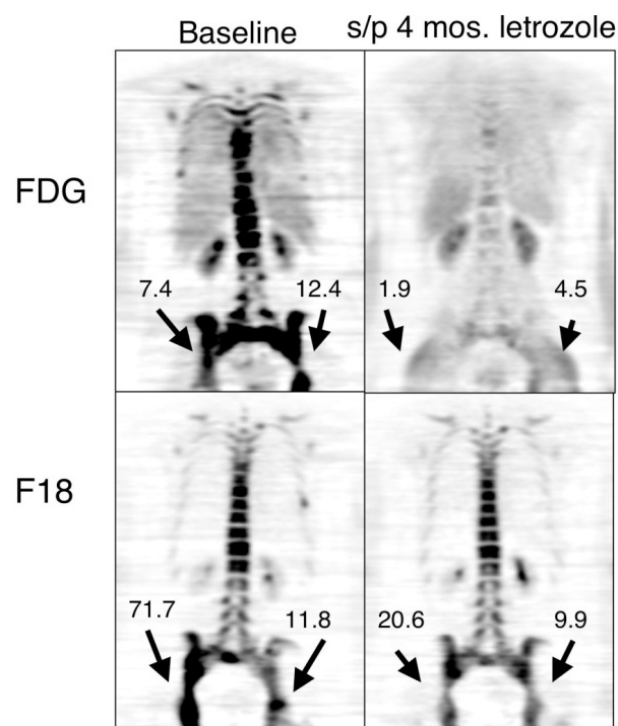


Figure 1.3 Example of patient's response to therapy. Images show glucose metabolism (FDG) and bone fluoride incorporation (F18) in a patient with widespread bony metastases from breast cancer before (left) and (right) after hormonal therapy. Numbers shown are tracer uptake values. The distribution of bony abnormalities is

different between FDG PET and fluoride PET. Response to therapy is qualitatively and quantitatively apparent in the FDG PET images (top), but the qualitative appearance of the fluoride image remains stable during the course of treatment. This demonstrates the importance of quantitative accuracy in PET/CT imaging in bone for evaluation of response to therapy (Kinahan *et al.*, 2006a).

1.3.3 The need for longer duration CT or dual energy CT for PET attenuation correction

As mentioned in previous section, PET data are taken over an averaged stage of respiration, whereas CT (e.g., usually helical CT in PET/CT scanner) data takes a snapshot of some state during respiration. The difference in the temporal resolution results in quantitative inaccuracies of the PET data.

To address the PET/CT quantitation problems caused by respiratory motion for lung imaging, several methods have been proposed. One of these methods is to use breath-hold PET Imaging (Kawano *et al.*, 2008; Pevsner *et al.*, 2005). However, the breath-hold PET imaging method is poorly tolerated by a large fraction of the population (Kawano *et al.*, 2008), particularly ill individuals. Other methods based on free-breathing principles for PET/CT imaging have been developed to manage respiratory motion (Nehmeh and Erdi, 2008), such as respiratory gated 4D PET/CT (Nehmeh *et al.*, 2004a; Abdelnour *et al.*, 2007; Dawood *et al.*, 2007; Guckenberger *et al.*, 2007; Nehmeh *et al.*, 2004b; Pan *et al.*, 2004), post processing methods (Dawood *et al.*, 2006), and motion corrected PET reconstruction (Lamare *et al.*, 2007; Li *et al.*, 2006; Qiao *et al.*, 2007; Qiao *et al.*, 2006). All of these methods depend on

accurate respiratory-gated CT images that are phase-matched with respiratory-gated PET images. However, when the CT data are acquired and reconstructed in a different respiratory phase than the PET data, quantitative accuracy of PET will be degraded. Thus, longer duration respiratory-gated CT are needed to phase-match with respiratory-gated PET images for accurate CT-based attenuation correction and motion correction for PET (Kinahan *et al.*, 2006b; Thielemans *et al.*, 2006). Figure 1.4 shows an example of the necessity to increase CT duration to phase-match with PET data. Even though from Figure 1.4 one would think that acquiring a series of CT scans during one very deep in and out breathing would cover the entire required patient real-time respiratory position signal amplitudes, the reliability of this method to capture the patient's respiratory motion during PET scanning for long duration is limited.

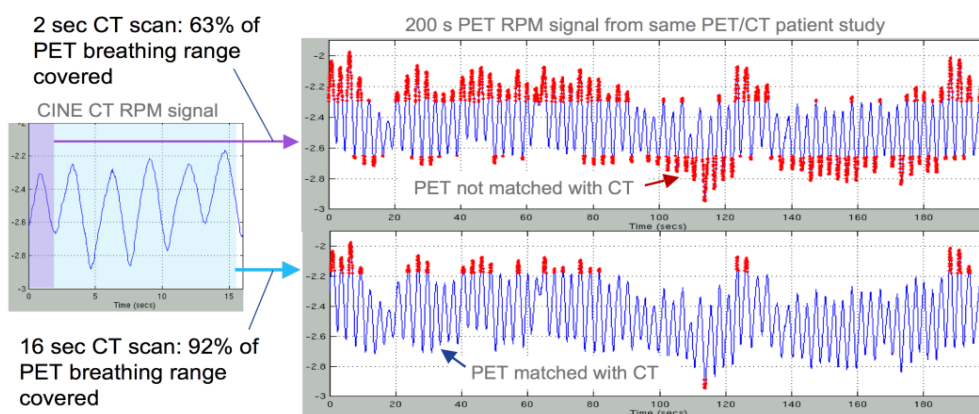


Figure 1.4 Patient study showing the impact of extending the duration of the CINE CT scan on the ability to match PET scan data for both motion and attenuation correction. In all three plots, the y axes are the patient RPM (REAL-TIME POSITION MANAGEMENT, Varian Medial Systems, Palo Alto, CA) signal amplitude in the unit

of centimeter, and x axes are time in the unit of second. In this example, if only 2 seconds CT is acquired, only 63% of PET breathing range can be covered; however, if the CT duration can be increased to 16 seconds, almost 92% of PET breathing range can be covered (Image courtesy of Dr. Paul Kinahan).

To address the problems of PET/CT bias for bone imaging, dual energy CT¹ (DECT) has been proposed for accurate CT based attenuation correction (CTAC) (Kinahan *et al.*, 2006a; Abella *et al.*, 2012). Dual energy CT imaging has been widely used for numerous medical applications such as bone mineral density measurements (Greenfield, 1992), as well as nonmedical applications. DECT has also been explored to form monoenergetic attenuation map at 140 keV for accurate SPECT/CT imaging (Hasegawa *et al.*, 1993). For PET quantitation, by collecting two CT scans using X-ray beams with different energy spectra and by estimating the energy dependence of attenuation coefficients in terms of a Compton scattering component and a photoelectric absorption component (Alvarez and Macovski, 1976; Alvarez and Seppi, 1979), an accurate estimate of the linear attenuation coefficients at 511 keV for PET energy can be obtained (Kinahan *et al.*, 2006a). Thus, dual-energy CTAC would allow for accurate attenuation correction in PET/CT imaging that involves high-Z materials, including bone, contrast agents, and metals. However, dual kVp scanning is needed for this purpose.

¹ It is more accurate to use the term dual-kVp CT, since each CT acquisition is polyenergetic, not monoenergetic. However, the term dual-energy CT is already in wide use.

1.3.4 Concerns about CT radiation dose during PET/CT imaging

Recently, radiation dose from medical examinations has received growing concern in both the medical community and the public. The recent estimates of radiation exposure published by the National Council of Radiation Protection show that in the past 25 years, the per capita dose from medical exposure (not including dental or radiotherapy) in the USA had increased almost 600% to about 3.0 mSv per year (NCRP, 2009). Approximately 70 million computed tomography procedures are performed per year. These CT scans account for only 17% of the procedures that use ionizing radiation, however, they account for approximately 50% of the collective dose from all procedures (Mettler *et al.*, 2008). Studies show that the increasing use of CT and radiation burden may lead to a significant increased incidence of cancer in the US population estimating that the current CT usage may be responsible for 1.5-2% of all cancers in the US (Brenner and Hall, 2007). A detailed investigation of radiation doses from PET/CT and CT scans is shown in Table 1.1.

Table 1.1 Radiation doses from PET/CT and CT scans. C+A+P = CT scan range of chest, abdomen, and pelvis, roughly equivalent to 'whole-body' range used in PET/CT.

Scan	Techniques	Effective Dose	References	Comments
PET	average administrated ¹⁸ F-FDG for adults vary from 259 – 740 MBq, or 5.18 - 8.14 MBq/kg	4.9 – 14.1 mSv *	Graham, 2011	based on survey of 15 U.S. academic medical centers with 20 PET/CT scanners
	average administrated ¹⁸ F-FDG of 390 MBq (range, 113 – 685 MBq) for a 75 kg patient	7.4 mSv * (range 2.1 – 11.1 mSv)	Beyer, 2011	based on international survey of 104 sites with 192 PET/CT scanners
	Recommended administration 190 MBq ¹⁸ F-FDG (in 3D mode)	3.6 mSv *	Boellaard, 2010	EANM guidelines
Diagnostic CT	110,120 or 140 kVp.; 80 – 400 mA, 0.5 – 2 s/rotation, 1 – 4 slices/rotation, 0.8 – 3 pitch scan coverage: 641 mm (380 – 945 mm)	17.9 ± 11.7 mSv (range 5.3 – 52.5 mSv)	2000 NEXT Survey, 2007 Table 1.59	based on survey in 29 hospitals and other facilities in U.S.
	similar as above, but includes 16 slices MDCT scan coverage: C+A+P	9.9 ± 4.0 mSv	Shrimpton, 2006 Table 7	based on survey at 118 hospitals with a total of 126 scanners in UK
	similar as above, wide clinical range of settings scan coverage: C+A+P	17.0 mSv (range 7.0 – 43.0 mSv)	NCRP Report No. 160, 2009 Table 4.2 data based on Mettler, 2008; McCollough, 2008, Brix, 2003.	based on results from multiple sources, e.g., a survey in Germany of a total of 113 scanners, and estimated from a national survey in U.S./UK

Scan	Techniques	Effective Dose	References	Comments
Diagnostic CT	GE 64 slice DSTE, 120 kVp or 140 kVp, 0.5 s rotation, 100 – 350 mA, helical with 0.984 pitch, scan coverage: base of skull to the upper thighs	7.2 – 26.0 mSv	Huang, 2009 Table 3	based on measurements of a humanoid phantom with thermoluminescent dosimeters (TLDs) from a GE scanner, and converted to effective dose according to ICRP report 103
	Diagnostic CT with contrast agent, 120 – 140 kVp, 111 – 200 mAs, 1.5 – 5.0 slice collimation, 1.0 – 1.5 pitch scan coverage: 851 – 890 mm	14.1 – 18.6 mSv	Brix, 2005 Table 2	based on measurements of a humanoid phantom with TLDs on 4 German hospital scanners, and converted to effective dose according to ICRP report 60
Lowdose CT for PET (anatomical)	110 – 120 kVp, 30 – 60 mAs, 0.75 – 6.5 slice collimation, 1.25 – 2 pitch scan coverage: 851 – 910 mm	1.3 - 4.5 mSv Geometrical mean 2.4	Brix, 2005 Table 2	based on measurements of a humanoid phantom with TLDs on 3 German hospital scanners, and converted to effective dose according to ICRP report 60
Lowdose CINE CTAC protocol (6s)	120 kVp, 10 mA, 8 x 2.50 mm collimation, 0.5 s rotation, 6 s cine duration Cine CT scan coverage: 200 mm thorax area	2.7 mSv ^a (5 mGy reported from Pan).	Pan, 2006 IMPACT software v.1.0.4	Recalculated here using IMPACT based on reported PET/CT scanner
Lowdose CINE + low dose helical CTAC	added whole body helical scan: 120 kVp, 300 mA, 0.5 s rotation, 1.35 pitch, 8 x 1.25 mm collimation helical scan coverage: 900 mm cine scan coverage: 200 mm thorax area	Total: 2.7 (cine) + 2.4 (helical) = 5.1 mSv (all CT) ^a .	Chi, 2007 IMPACT software v.1.0.4	Recalculated here using IMPACT based on reported CT scanner
Extended CINE duration (15 s) and 2x axial scan coverage	same as Pan 2006, with 15 s cine duration scan coverage: 400 mm thorax area helical scan coverage: 900 mm	13.5 (cine-CT) + 2.4 (helical) = 15.9 mSv (all CT) ^a	IMPACT software v.1.0.4	Calculated here

^a Range based on (1.9E-02 mSv /MBq) ICRP report 106, 2008 (Table C.9.4)

^b Recalculated from IMPACT based on ICRP 103 Table 3

From Table 1.1, we can see that for 18F-FDG PET/CT scans with diagnostic-quality CT, a typical total effective dose is expected to be much higher than 10 mSv. If diagnostic-quality CT is not required, a standard PET/CT exam with a CT for attenuation correction only imparts a whole body effective dose of at least 6 mSv.

However, for quantitative PET lung imaging, with current CT techniques available in the clinic, longer duration CT that aims to improve respiratory matching between the PET and CT implies an even higher radiation dose, while the radiation dose from respiratory CT imaging is already high. For example, if we increase Cine mode CT duration to 15 seconds and extend the axial scan coverage to about 400 mm, the radiation dose from CT increases dramatically to 15.9 mSv.

For quantitative PET bone imaging with dual energy CT for attenuation correction, two kVp CT scans (or fast kVp switch scans) are required, which imparts a higher radiation dose than conventional single CT scan for attenuation correction.

In summary, for both cases, radiation dose from the CT scans could be unacceptably high with current CT techniques, which inhibits the clinical application of quantitative PET imaging methods. Thus, there is a strong motivation to reduce the CT dose for quantitative PET imaging as much as possible without degrading PET image quality. This is possible,

since the requirement of CT in PET/CT is mainly for attenuation correction rather than diagnostic purpose.

1.4 Other modalities used in clinical for cancer imaging

Though PET imaging was firstly developed for neurological and cardiac research, now a large body of PET applications are for oncology since the recognition of importance of FDG-PET imaging in the evaluation of cancer and the integration of PET and CT into one system. It is already known that PET/CT is a powerful tool in oncological imaging. For oncological imaging, there are different purposes, such as screening, diagnosis and staging, guiding cancer treatment, evaluation of response to therapy, and monitoring for cancer recurrence. Besides PET/CT, there are many other medical imaging modalities, such as X-ray CT, ultrasound (US), magnetic resonance imaging (MRI) and single photon emission computed tomography (SPECT), etc. This section will briefly discuss other major medical imaging modalities, including their limitations for applications in oncology.

1.4.1 Ultrasound

Ultrasound imaging takes advantage of mechanical energy to image the acoustic properties of the biological tissue. It entails moving a hand held probe over the patient and using a water-based gel to ensure good acoustic coupling. The probe contains one or more acoustic transducers and sends pulses of sound into the patient. Whenever a sound wave encounters a material with different acoustical impedance, part of the sound wave is reflected which the probe detects as an echo. The time it takes for the echo to travel back to the probe is measured and used to calculate the depth of the

tissue interface causing the echo. The greater the difference between acoustic impedances, the larger the echo is. A computer is then used to interpret these echo waveforms to construct an image (Jensen, 2007). It is excellent for non-invasively imaging and diagnosing a number of organs and conditions, without ionizing radiation.

Ultrasound imaging has a wide application in oncology. Ultrasound has been reported for breast lesion detection to distinguish between solid tumors and fluid-filled cysts (Houssami *et al.*, 2005), for prostate cancer detection (Beissert *et al.*, 2008), for laryngeal carcinoma assessment (Loveday *et al.*, 1994), for vaginal, ovarian and uterine cancer screening and detection (Bhosale and Iyer, 2008), for pancreatic cancer (Hanbidge, 2002) diagnosis, for lymph node metastases detection (Adams *et al.*, 1998) etc.

For breast cancer detection, it is documented that ultrasound has a mean sensitivity around 85.7% (range from 80.4% to 89.9%), and mean specificity around 96.2% (range from 95.4% to 97%) (Pan *et al.*, 2010). It is suggested that ultrasound may be most useful when abnormal, but normal values cannot exclude the presence of active disease. For head and neck cancer, sonography of the cervical region has been applied for the detection of lymph node metastases with accuracy between 70% and 89% (van den Brekel, 2000; Adams *et al.*, 1998). For prostate cancer, transrectal ultrasound (TRUS) has only moderate accuracy in the detection of prostate carcinoma, but is very useful in the estimation of prostate volume (De Visschere *et al.*, 2010). Ultrasound has a sensitivity of 90% to 94% in detecting pancreatic cancer, but there are also reported sensitivities below 70% (Hanbidge, 2002).

For gynecologic malignancy, ultrasound is the first-line imaging modality of choice and is used to discriminate between benign and malignant adnexal masses and for characterizing adnexal tumors such as dermoid cyst, endometrioma, hemorrhagic corpus luteum, etc. (Bhosale and Iyer, 2008). Transvaginal ultrasound is the preferred technique for initial evaluation of ovarian tumor because of its availability, high resolution, and lack of ionizing radiation.

Ultrasound imaging is a relatively inexpensive, real-time and ionizing-radiation-free imaging modality. It is often used as the first modality for screening disease and can be used repeatedly without any worry about clinical radiation exposure. Ultrasound can show tumors, and can also guide doctors in performing biopsies or treating tumors. Recent preclinical research about ultrasound and microbubbles shows exciting possibilities of this modality for the early detection of cancer at the molecular level (Willmann *et al.*, 2010). However, the results of current clinical ultrasound imaging are quite dependent on the sonographer's skill level and experience, and it is not able to distinguish between reactive enlarged lymph nodes and enlargement due to metastatic disease. Distant metastasis assessment is not feasible by ultrasound. In addition, there are not many publications regarding the clinical application of quantitative evaluation of response to therapy with ultrasound imaging.

1.4.2 Endoscopic Ultrasound (EUS)

By installing the ultrasound transducer on the tip of a special endoscope, the endoscopic ultrasound (EUS) can be used in clinic to obtain

high quality ultrasound images of the organs inside the body upper or the lower digestive tract or in mediastinum. EUS has been reported useful for local staging of esophageal, gastric, duodenal, lung and rectal cancer using the TNM (tumor, node, metastases) system, as well as for the diagnosing and staging of pancreatic lesions (Keter and Melzer, 2008).

EUS is highly sensitive in the detection of small tumors and invasion of major vascular structures. It is reported that EUS staging accuracy is similar among all luminal GI tract and pancreatic cancers, with an approximate T-stage accuracy of 85% and N-stage accuracy of 75% (Keter and Melzer, 2008). Thus, EUS is superior to spiral CT, MRI and PET in the detection of small tumors (Miura *et al.*, 2006) and it can also locate lymph node metastases and vascular tumor infiltration with high sensitivity (Miura *et al.*, 2006; Muller *et al.*, 1994; Legmann *et al.*, 1998). The main indications to endoscopic ultrasonography can be explained by its ability to visualize the wall as a multi-layer structure corresponding to histological layers. Other important indications derive from its capability of displaying, very closely, the structures and lesions surrounding the gut wall, such as the pancreatic-biliary area, masses and lymph nodes. Studies of esophageal cancer staging with EUS have demonstrated strength in T and N staging accuracy (Walker *et al.*, 2010; Rosch, 1995), prediction of patient survival (Pfau *et al.*, 2001), and cost-effectiveness (Harewood and Wiersema, 2002). Recently, EUS has seen successful by using it conjunction with fine needle aspiration (FNA). The addition of EUS-guided FNA has improved the ability to detect malignant lymph node invasion (Keter and Melzer, 2008).

However, a significant weakness of EUS staging alone is that it cannot provide the most important factor in staging—the presence or absence of metastatic disease. Thus, EUS should be used after CT or MRI scan has shown no distant metastatic disease. Besides, in some cases insufficient visualization of lesions and the presence of inflammatory cell infiltration and/or fibrosis are sources of inaccurate diagnosis. In addition, the accuracy of EUS has been shown to be operator-dependent (Keter and Melzer, 2008). Also, EUS is not suitable for quantitative evaluation of response to therapy.

1.4.3. X-ray CT

X-ray Computerized Tomography (CT) scan was developed in 1970. The CT scan has become an important advancement relative to X-ray radiography, which is only a projected view of the object without depth information. The CT scan uses multiple X-ray beams projected at many angles in conjunction with computer resources to create three-dimensional cross-sectional images. The advent of helical multi-detector scanner in medicine has shortened the scanning times and computers provided the reconstructed images in less time. Each image or picture reveals a different level of tissue that resembles slices. Basic physics and major components of X-ray CT can be found in the later sections of this proposal.

CT acquisition is fast and the image resolution is high. In addition, the contrast between soft tissue and bone is high. Thus CT has been used in oncology for screening, staging, restaging and monitoring treatment. It may be used to examine structures and tumors in the abdomen and pelvis (e.g., liver, gallbladder, pancreas, spleen, intestines, reproductive organs), in the chest

(e.g., heart, aorta, lungs), and in the head (e.g., brain, skull, sinuses). It also can be used to detect abnormalities in the neck and spine (e.g., vertebrae, intervertebral discs, spinal cord) and in nerves and blood vessels. CT is the most common modality in lung cancer imaging. For pancreatic adenocarcinoma, CT has a positive predictive value tumor detection of greater than 90%. For gynecologic malignancy, CT is often the first technique with which ovarian cancer is detected (Iyer and Lee, 2010). It is the preferred technique in the pretreatment evaluation of ovarian cancer to define the extent of disease and assess the likelihood of optimal surgical cytoreduction.

In summary, CT is widely available, fast and with high reliability in detecting abnormalities. With the fast development of CT techniques, it plays an increasing role in oncology. However, the major limitation of CT is that it uses ionizing radiation, which should be minimized when possible. CT is further limited due to the fact that it relies only on morphological data and does not give functional information, which is a limitation for evaluation of response to therapy in oncology.

1.4.4 MRI

Magnetic Resonance Imaging (MRI) is achieved by using a strong magnetic field, typically 1.5 or 3 Tesla for human scanners, which aligns the hydrogen nuclei to make them spin in a direction parallel to the magnetic field. A Radio Frequency (RF) pulse is applied to the object, which causes the nuclear spins to acquire enough energy to tilt and precess, where an RF receiver can record the resulting signal. After the removal of the RF pulse, the spins realign parallel to the main magnetic field with a time constant of T₁,

which is tissue dependent. Signal strength decreases in time with a loss of phase coherence of the spins. This decrease occurs at a time constant T2 which is always less than T1. Magnetic gradients are used to localize spins in space, enabling an image to be formed. The difference in spin density, T1 and T2 among different tissues enables the excellent tissue contrast of MRI (Kherlopian *et al.*, 2008).

MRI is free of ionizing radiation. MRI has superior soft tissue contrast compared to X-ray CT, which could improve tumor localization and nodal staging. MRI has a wide application in oncology for diagnosing and staging various cancers (Wallis and Gilbert, 1999). It has been used in clinical settings for imaging tumors in the brain and other anatomical sites (e.g., breast, prostate, pelvis, head and neck, extremities, abdomen, etc.) due to its high soft tissue contrast. For prostate cancer, where FDG PET/CT is challenged, MRI shows great potential (Beissert *et al.*, 2008). For pancreatic cancer, MRI has accuracy similar to that of CT for detecting and staging, with published accuracies of 90% to 100% (Hanbidge, 2002). For breast imaging, MRI has higher sensitivity than ultrasound, with mean of 95% but lower specificity. Compared with 18F-FDG PET/CT scan, it has been documented that 18F-FDG PET/CT mammography may be more accurate than MRI mammography in pretherapeutically differentiating breast lesions as unifocal, multifocal, or multicentric (Heusner *et al.*, 2008).

In summary, MRI has tremendous applications in oncology due to its superior soft tissue contrast and lack of ionizing radiation. Like CT, it is predominately used for imaging morphological information in the body. It

could play an important role in radiation oncology treatment planning. MRI could be useful in assessing the response to neoadjuvant chemotherapy; however, it may underestimate the residual tumor due to decreased vascularity and permeability after chemotherapy (Shah and Greatrex, 2005). Though dynamic contrast-enhanced (DCE)-MRI could evaluate tumors with respect to their state of the functional microcirculation, quantitation of these techniques needs further improvement (Padhani, 2002). Other major limitations of MRI are that it takes longer time than a CT acquisition, may suffer more from motion artifacts than CT, and it is not suitable for all patients, including those with metallic implants and claustrophobia.

1.4.5 SPECT and SPECT/CT

Single photon emission computed tomography (SPECT) is a nuclear medicine tomographic imaging technique using gamma rays. SPECT uses radiopharmaceuticals labeled with a single-photon emitter, a radioisotope that emits one gamma-ray photon with each radioactive decay event. By using a gamma camera to acquire multiple 2-D images (also called projections), from multiple angles, the SPECT images can be reconstructed from the 3D data set.

Like PET/CT, SPECT can be integrated with X-ray CT into one imaging system, and the combination of both types of imaging data could provide functional and anatomical information inside the body. In addition to functional cardiac and brain imaging, SPECT can also be used in oncology. Since FDG for PET/CT is expensive and has a short half-life, SPECT/CT can be more flexible because it has more abundant radiotracers than PET/CT does, and its

tracers are cheaper, easier to acquire, and, in certain tumors, sometimes more accurate than FDG (Rahmim and Zaidi, 2008). It has been reported that SPECT/CT can be applied to radioimmunoscinigraphy (RIS) and sentinel lymph node (SN) scintigraphy for the assessment of various types of cancer. It is useful for identifying prostate cancer, breast, oral, skin cancer (Tagliabue and Schillaci, 2007), and is of value in increasing the diagnostic accuracy of bone scanning.

However, SPECT is less quantitative than PET in several aspects. For example, the attenuation of emitted photon in SPECT is location dependent due to its single-photon emission nature, making it more challenging than PET for attenuation correction. SPECT/CT has lower spatial resolution and more artifacts than PET/CT. For oncological imaging, PET/CT seems more reliable than SPECT/CT. Thus, currently PET/CT is superior to SPECT/CT in oncology for quantitative evaluation of response to therapy.

1.5 Organization of this dissertation

Until now, the motivation and significance of the study performed for this dissertation have been briefly discussed. The overall goal of this thesis is to reduce the CT radiation dose as low as possible for PET attenuation correction for quantitative PET imaging. It has two major applications. For quantitative PET lung imaging, the goal is to reduce CT dose dramatically, to develop ultra-low dose CT techniques only for attenuation correction without degrading PET image quality. For quantitative PET imaging of cancer in bone, dual energy CT technique is used, in which CT is used for accurate attenuation correction and localization purposes.

Chapter II provides the background for this dissertation, in which, the basic physics of PET and CT are introduced, methods for CT based PET attenuation correction are briefly described, and different metrics for dose measurements are explained

Chapter III discusses the tools used and developed in the simulation studies for this dissertation. Both PET and CT simulation tools are introduced, and some further improvements of the current simulation tools are also explained and provided.

The simulation studies for ultra-low dose CT used for PET attenuation correction are presented in Chapter IV. The results presented in Chapter IV could enable respiratory motion compensation methods that require extended duration CT scans and reduce radiation exposure in general for all PET/CT imaging.

Chapter V provides simulation studies of dual energy CT for PET attenuation correction for quantitative bone imaging with PET/CT.

Chapter VI discusses the phantom-based measured experiment on a CT scanner for spectra validation.

Chapter VII summarizes the work and contribution of this dissertation, and points out the possible future directions.

The codes of the developed tools and some additional experiment data are collected and provided in the appendices for future references.

Chapter II: Background

2.1 PET physics

2.1.1 Major components of a PET/CT system

In a broad view, there are three major components of a PET/CT system: (1) a PET scanner, (2) a CT scanner, and (3) a patient table with a patient handling system. The PET component contains detector blocks, electronics and an acquisition system. The CT component is a standalone CT system. The patient table with patient handling system provides patient transport over the two fields of view with limited table deflection variation.

Since the commercial introduction of PET/CT in 2001, there has been rapid application of the technology. Improvements in CT and PET instrumentation can be incorporated directly into PET/CT, such as new scintillation crystals, time-of-flight (TOF) techniques, novel image reconstruction algorithms and multi-slice CT (MSCT). Today, the five main vendors (GE Healthcare, Hitachi Medical, Philips Healthcare, Toshiba Medical Corporation and Siemens Medical Solutions) worldwide offer over 20 different PET/CT designs. Table 2.1 provides some key specifications for most of the current commercial PET/CT systems.

Table 2.1 Key specifications of current commercial PET/CT scanners.

Abbreviations: FOV, field of view; AC, attenuation correction; 2D, two-dimensional; 3D, three-dimensional; 4D, four-dimensional; TOF, time of flight; N/A, not applicable. Data from General Electric Healthcare (www.gehealthcare.com); Siemens Medical solutions (www.medical.siemens.com); Philips Healthcare (www.healthcare.philips.com); and Imaging Technology News (www.itnonline.net).

Company	GE	GE	GE	GE	GE	SIEMENS	SIEMENS	PHILIPS	PHILIPS
Model/product name	Discovery PET/CT 600	Discovery PET/CT690	Discovery VCT	Optima 560	Discovery STE	Biograph TruePoint	Biograph mCT	Gemini TF big bore(PET/CT)	Gemini TF(PET/CT)
Scanner									
Patient port diameter(cm)	70	70	70	70	70	70	78	OpenView Gantry 85	OpenView Gantry 70
Min room size(ft)	13*25	13*25	14*25	13*25	14*24	15*24	15*24	13*23	14*24
Transmission source	CT AC	CT AC	CT AC	CT AC	CT AC	Spiral CT	Spiral CT	CT	CT
Bed type	double cantilever	double cantilever	double cantilever	double cantilever	double cantilever	fixed sliding support	fixed sliding support	single cantilever with center support	single cantilever with center support
Coscan length(cm)	170	170	170	200	160	190	198	190	190
Max bed load(lbs)	500	500	450	500	400	450/500(B1 6)	500	500	430
PET component									
Detector material	BGO	BGO	BGO	BGO	BGO	LSO	LSO	LYSO	LYSO
Acquisition mode	3D,4D	3D,4D	2D,3D,4D	3D static multi-static	2D,3D,4D	3D	3D	3D, 4D TOF (Respiratory Gating)	3D, 4D TOF (Respiratory Gating)
Number of crystals	12288	13824	13440	12288	13440	24336/3244 8with trueV	24336/3244 8with trueV	28336	28336
Detector diameter(cm)	ring 81	81	88.6	88.6	88.6	84.2	84.2	90	90
Crystal dim(mm)	4.7*6.3*30	4.7*6.3*25	4.7*6.3*30	4.7*6.3*30	4.7*6.3*30	4.4*20	4.4*20	4.4*22	4.4*22
Trans*axial*thick	24	24	24	24	24	39/52 with trueV	39/52 with trueV	28	28
Number of rings	47*3.27	47*3.27	47*3.27	47*3.27	47*3.27	81/109*2.0 with trueV	81/109*2.0 with trueV	45/90*2/4	45/90*2/4
Image planes	47*3.27	47*3.27	47*3.27	47*3.27	47*3.27	with trueV	with trueV	with trueV	with trueV

2.1.2 Positron annihilation coincidence detection

PET imaging detects positron annihilation events, where a positron and electron are annihilated in the process of converting their combined masses into the energy of a pair of 511 keV photons that are emitted from the annihilation location at nearly opposite directions relative to each other. Figure 2.1 illustrates the physics of positron decay and annihilation, which results in two 511 keV gamma rays. If both of these annihilation photons interact with detectors, a coincidence event will be recorded by the detection system, which is illustrated in Figure 2.2. A recorded coincidence indicates an annihilation occurred somewhere along the line connecting the two detectors, which is also referred to as line of response (LOR). To reconstruct a complete cross-sectional image of the object, data from a large number of these LORs are collected at different angles and radial offsets that cover the field of view of the system.

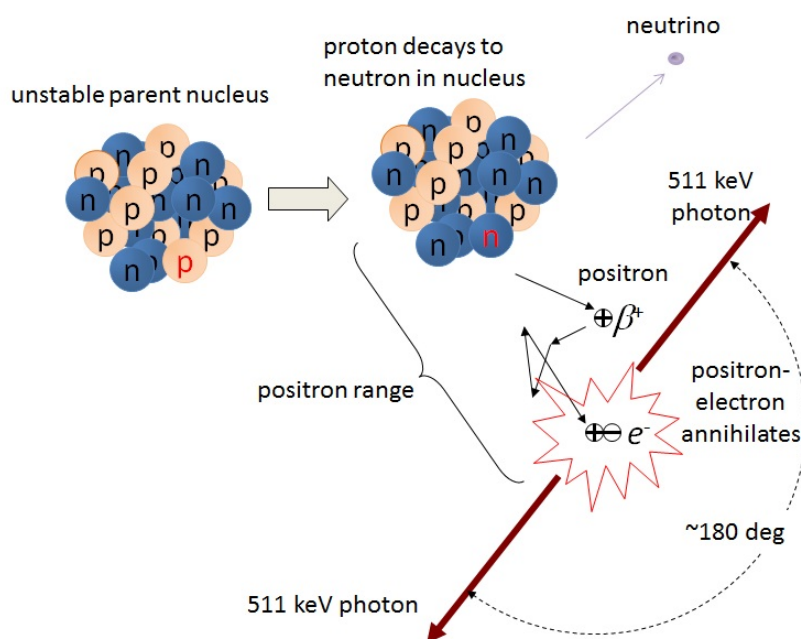


Figure 2. 1 Physics of positron decay and annihilation, which results in two

511 keV gamma rays.

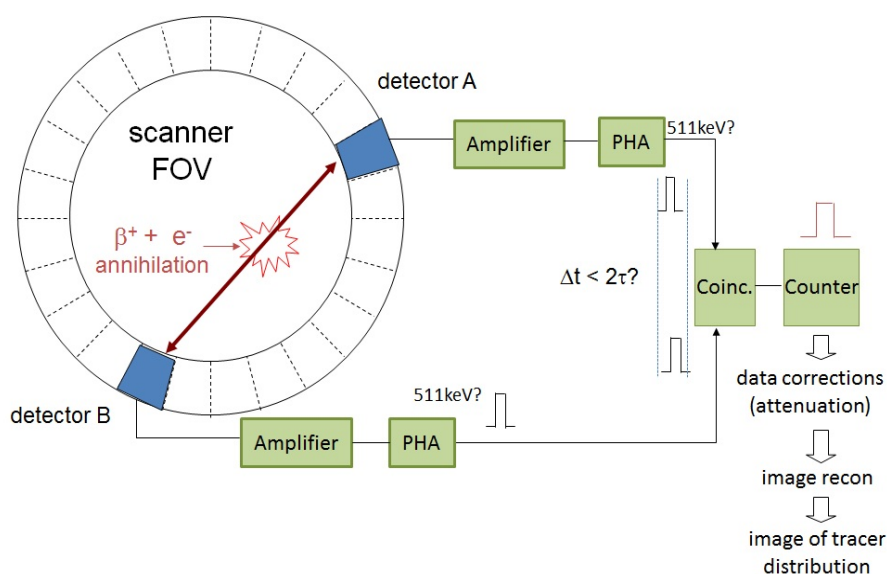


Figure 2.2 Diagram of a basic PET detection system. The two scintillation detectors are connected to individual amplifiers, and pulse height analyzers (PHA). As soon as a photon interacts in either of the detectors, the signals are amplified and analyzed to determine if the energy satisfy a certain criterion. The PHA will generate a logic pulse if the measured energy is above a pre-determined threshold. The coincidence module (Coinc.) analyzes the time differences between the two pulses and determines whether the two pulses are within a time window to be registered as an annihilation event. Then the signal undergoes data correction and image reconstruction to form the tracer distribution image.

Ideally, only events where the two detected annihilation photons originate from the same radioactive decay and have not changed direction or lost any energy will be detected. However, in practice, the detectors are not ideal and the 511 keV photons will interact in the body before they reach the detector, the true coincidences measured are contaminated with undesirable events, such as random and scattered coincidences, as shown in Figure 2.3.

Many methods have been successfully applied to correct and minimize of these undesired events. The high degree of confidence in estimating random and scatter contributes to the detection of the true events. The incorporation of physical effects into system matrix for image reconstruction makes PET imaging one of the most quantitative imaging modalities and well poised to quantify changes in activity concentrations of tracer in targeted tissue in clinical trials.

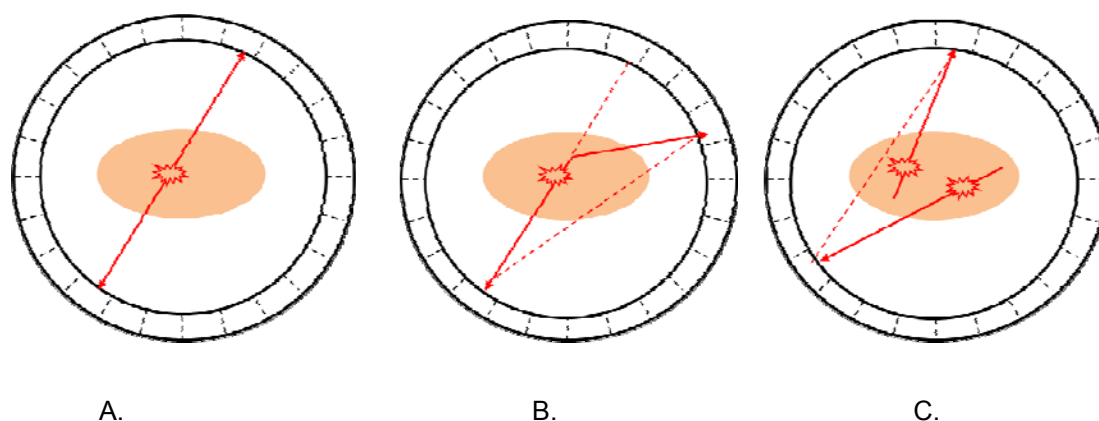


Figure 2.3 Illustration of the three main coincidence event types. A. True coincidence. B. Scattered coincidence. C. Random coincidence.

2.1.3 Photon attenuation and correction in PET

At 511 keV, there is a relatively high probability that one or both annihilation photons will interact in the subject, largely through Compton interactions. These interactions lead to the removal or attenuation of primary photons from a given LOR and the potential detection of scattered photons in a different LOR. Photon attenuation is the most important effect that needs to be corrected, and it can affect both the visual quality and the quantitative accuracy of PET data. Figure 2.4 is an example of ^{18}F -FDG PET scan in which lesion detection is significantly degraded in the image reconstructed

without compensation for photon attenuation (Figure 2.4 left) in comparison with the image reconstructed with attenuation correction (Figure 2.4 right).

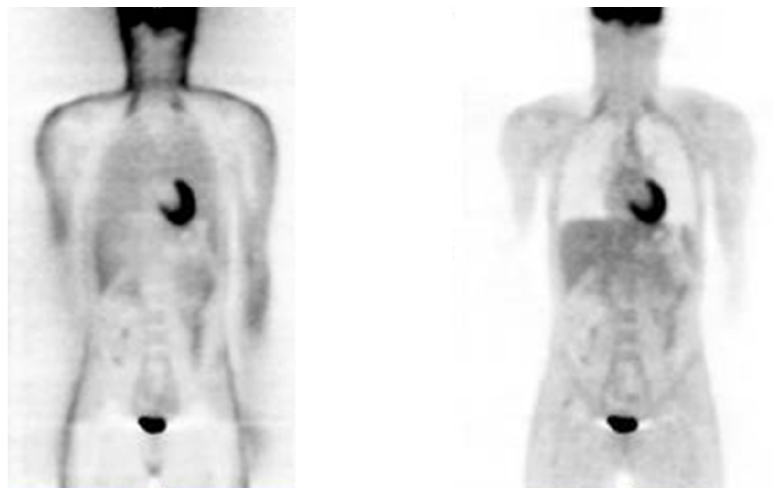


Figure 2.4 Example of ^{18}F -FDG PET scan without attenuation correction (AC) (left) and with attenuation correction (right). It can be seen that compensation for photon attenuation is important.

The interaction (absorption or scattering) of 511 keV photons by matter can be described according to well-known Bouger-Lambert-Beer law:

$$I(x') = I_0 \exp\left(-\int_0^{x'} \mu(x) dx\right) \quad (2.1)$$

where I_0 is the intensity of the original 511 keV photons interacting with the medium, x' is the thickness of the medium, and $I(x')$ is the intensity of 511 keV photons after passing through the material, and μ is the linear attenuation coefficient that is defined as the probability per unit path length that the photon will interact with the attenuating material (e.g., tissue).

Consider a point source located at an unknown depth x in an attenuating medium as illustrated in Figure 2.5. If the thickness of the object is

along the LOR, then the probability that the annihilation photon 1 will be registered by detector 1 is:

$$p_1 = \exp\left(-\int_0^{x'} \mu(x)dx\right), \quad (2.2)$$

and the probability that the annihilation photon 2 will be registered by detector 2 is:

$$p_2 = \exp\left(-\int_{x'}^d \mu(x)dx\right) \quad (2.3)$$

The total probability that the pair of the annihilation photons being detected is:

$$p = p_1 \cdot p_2 = \exp\left(-\int_0^d \mu(x)dx\right) \quad (2.4)$$

Thus, the attenuation of the photons is independent of the location of the source and only dependent on the total thickness of the object along the LOR and the attenuation coefficient of the object.

The corrected PET emission projection data can be described mathematically as:

$$p(x', \varphi) = \left[\exp\left(-\int_{-\infty}^{\infty} \mu(x, y)dy'\right) \right] \cdot \int_{-\infty}^{\infty} f(x, y)dy' \quad (2.5)$$

The exponential term in the above square brackets represents the attenuation along the LOR at detector position x' and projection angle ϕ (Figure 2.6). The goal of PET imaging is to estimate the distribution of tracer uptake $f(x, y)$ from the set of acquired projection data $p(x', \varphi)$ through image reconstruction. The task of attenuation correction is to calculate the

attenuation correction factor to compensate for attenuation effects

$$a(x', \varphi) = \exp\left(\int_{-\infty}^{\infty} \mu(x, y) dy'\right) \quad (2.6)$$

by multiplying equation (2.5) with equation (2.6).

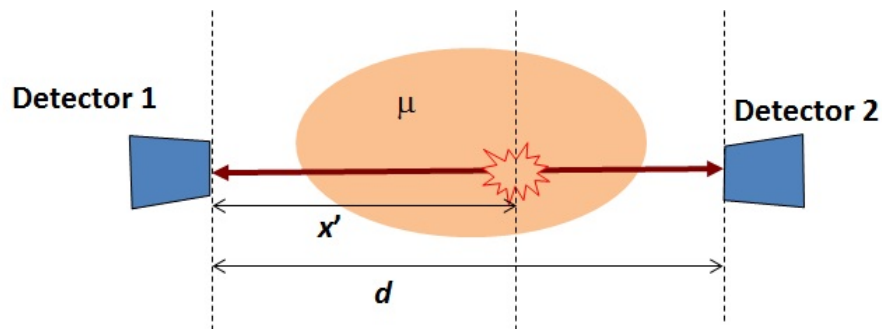


Figure 2.5 Attenuation detection in PET. The attenuation correction does not depend on where along the LOR the annihilation happens.

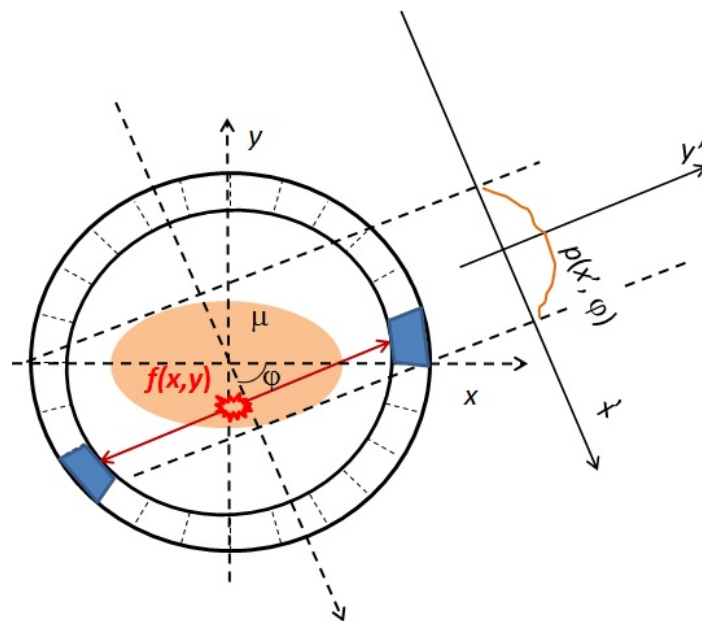


Figure 2.6 Attenuation in PET. The acquired projection signal is tracer distribution corrupted by photon attenuation.

A discussion of various PET attenuation corrections is given in section 2.3, with an emphasis on methods of CT based PET attenuation correction.

2.1.4 PET processing steps other than for attenuation

Random correction

Random coincidences in PET imaging lead to additional events being recorded in lines of response (LORs) (Hoffman *et al.*, 1981). These events are not spatially dependent, and are distributed almost uniformly across the field of view. They impact the image contrast and quantification if not properly corrected. There are two main approaches for random correction. The first one is to estimate the random counting rate from the singles counting rate for a given detector pair and coincidence time window, and subtracting the number of random events for every detector pair in the scanner. The second approach is to measure the random coincidences by using a delayed time window (Cherry *et al.*, 2003). Then the number of random events recorded in the delayed time window is subtracted from the number of events recorded in the un-delayed window. This approach usually suffers from an increase in the statistical noise level for the measurement, especially when the random coincidences are high. Compared to the second approach, the first approach produces a statistically superior estimate of the number of random events but may suffer from systematic, additional measurement errors in determination of the coincidence time window.

Scatter correction

Scatter events in PET imaging result in an incorrect background in the

reconstructed images (Cherry *et al.*, 2003). If not corrected, scatter effects decrease image contrast and PET quantitative accuracy. The fraction of scattered events in PET is in the range of 10% - 15% for a 2D scan with the inter-plane septa in place, and in the range of 30%- 40% for a 3D mode brain imaging (Phelps, 2006). In fact, scatter and attenuation are very closely related physical effects: when one of the annihilation photons scatters, the event is removed from its original LOR (attenuation), and it may still be detected in a different LOR (scatter). Thus, in principle, scatter correction should be performed ahead of attenuation correction.

There are generally two approaches for scatter correction. The first approach is to use analytical methods, based on the fact that scatter is a low-frequency phenomenon containing little structure information. Then the amount of scatter is estimated by examination of projection profiles immediately outside the object. Scattered data is extrapolated from the tails of the projection profiles using simple smoothly varying functions across the projection, and is subtracted from the projections prior to image reconstruction. This approach is straightforward, fast and measurement-based, and can account for scatter from activities outside the field of view. However, it is only an approximation of the true scatter distribution, and has limitations when the object occupies the whole field of view or when the scatter distribution is complex due to multiple scattering. The second approach is to use simulation to estimate scatter by first reconstructing image without scatter correction (Phelps, 2006). Together with the attenuation image and computer modelling, the scatter distribution can be estimated (e.g., using

a simple single scatter model, or a Monte Carlo simulation). This approach is more accurate but requires more computation time due to the additional image reconstruction and estimation.

Normalization

Normalization correction is applied to compensate non-uniformities between different lines of response (LORs) in the PET system due to individual detector efficiencies, geometrical variations, and so on. Thus, individual detector efficiencies and any geometrical efficiency variations need to be measured to generate normalization correction. Detailed information can be referred to (Phelps, 2006).

Dead time correction

In most PET systems, the dead time effect comes from the processing of each event in the detector front-end electronics. Dead time correction is necessary to rectify the underestimation of radioactivity concentration at high counting rates, especially for studies near the bladder or with very short-lived radiotracers. Dead time correction is accomplished by using empirical dead time models in which the observed count rate as a function of radioactivity concentration is measured for a range of object sizes and at different energy thresholds (Cherry *et al.*, 2003).

Decay correction

Decay correction is necessary to correct the data for the radioactivity decay nature of the isotope. Decay correction is needed to restore the activity of each data set to that which would have been measured at the reference

time. Decay correction is usually completed by keeping record of the time elapsed between some reference time (e.g., radiotracer injection time) and each study and then by multiplying the acquired data by the decay factor.

Image reconstruction

Good reviews of image reconstruction for PET can be found in references (Tong *et al.*, 2010a; Wernick and Aarsvold, 2004). In general, there are two types of image reconstruction: analytical image reconstruction and iterative image reconstruction. Analytical reconstruction methods assume that the data is deterministic while iterative methods often assume that the data follows a random distribution, such as Poisson, in order to model the data noise properties. Analytical reconstruction methods assume that the collected sinogram data consist of line integrals of the object distribution, and do not consider the randomness of the gamma-ray counting process. This type of reconstruction method requires little computation time, but has poor noise performance that leads to characteristic streaking artifacts for noisy data. On the other hand, iterative methods have the capability to incorporate more sophisticated models of the imaging system with consideration of the physics of the imaging process. Thus, iterative reconstruction methods could generate images with better noise reduction, and more accurate physical modelling. However, iterative methods require more computation power and are thus time-consuming compared to analytical methods.

Dose calibration

Dose calibration is applied after image reconstruction. In dose

calibration, the measured counts per unit time in each pixel are converted to the radioactivity concentration in each pixel. This is done by a linear mapping: dividing each image pixel value with the calibration factor CAL which is defined as:

$$\text{CAL} = \text{couns per pixel} / \text{radioactivity concentration in cylinder} \quad (2.7)$$

This calibration factor is obtained by scanning a cylinder containing a uniform solution of a known radioactivity concentration.

2.1.5 Radiopharmaceuticals used for PET oncologic imaging

Many different PET tracers are available to researchers to study various aspects of cell metabolism, receptor binding, and other biochemistry and physiology in oncology. These tracers are labeled with positron-emitting radionuclides, such as carbon-11, nitrogen-13, oxygen-15, or fluorine-18, which are produced by bombardment of specific stable radionuclides with accelerated protons or deuterons in a cyclotron. Table 2.2 summarizes tracers that have been used so far for oncological PET studies, with updates to reference (Weber *et al.*, 1999).

This dissertation focuses on the tracer ¹⁸F-fluorodeoxyglucose (FDG), which is widely used for functional imaging of most cancers clinically. The use of this glucose analog tracer in the study of cancer is based on the observation that glucose use by tumor cells is accelerated (Nelson *et al.*, 2000) due to the Warburg Effect (Warburg, 1956; Kim and Dang, 2006) where tumor cells have switched to an altered energy metabolism that favors less efficient anaerobic glycolysis over the more efficient aerobic respiration used

by normal cells. FDG is an ideal tracer for detecting areas of aberrantly high glucose uptake in some cancers because FDG becomes trapped in tissue for the duration of the PET imaging studies after being phosphorylated by the glycolytic enzyme hexokinase. This selective targeting of cancerous tissue by FDG has lead the US Centers for Medicare and Medicaid Services (CMS) to approve reimbursement of FDG PET scans for use in patients with certain types of cancer (Doot, 2008).

Table 2.2 Overview of radiopharmaceuticals used for oncological PET studies (cited and modified from (Weber *et al.*, 1999))

Compound	Physical half-life(min)	Targeted process
F-18-fluorodeoxyglucose (FDG)	110	Glucose metabolism
C-11-methionine (MET)	20	Amino-acid transport and metabolism
F-18-fluoride	110	Bone remodeling
C-11-thymidine	20	DNA synthesis
F-18-fluormisonidazole (FMISO)	110	Hypoxia
O-15-water	2	Perfusion
F-18-fluorthymidine (FLT)	110	DNA synthesis (thymidine phosphorylation)
F-18-fluorethyltyrosine	110	Amino-acid transport
C-11-choline	20	Choline metabolism
F-18-fluormethyltyrosine	110	Amino-acid transport
I-124-iodo-fluoro-deoxy-arabino-furanosyl-uracil (FIAU)	110	Herpes simplex thymidine kinase gene expression
F-18-Fluoro-I-Dihydroxyphenylalanine (FDOPA)	110	amino acid transport and formation of dopamine

2.2 CT physics

Unlike the emission imaging modality of PET, CT uses transmission imaging via an X-ray source to measure the attenuation properties of the body. This section briefly describes the CT system, data processing chain in CT and some major physical effects in CT imaging.

2.2.1 Major components of a CT system

A generic block diagram of a typical third generation CT system can be found in Chapter 6 of the Book by Hsieh (Hsieh, 2009). In General, a CT system contains an X-ray generation unit, X-ray detection unit, operational control unit, data acquisition unit, patient handling unit, and an image generation and display unit. Here is a brief review of some important components of a CT system.

X-ray tube

A typical X-ray tube contains an evacuated envelope, a cathode assembly and a rotating anode situated opposite to the cathode. The electrons are released from the cathode filament by thermionic emission governed by Richardson-Dushman equation (Buzug, 2008). The electrons are accelerated by the applied high voltage to 30% to 65% of the speed of light and bombard a small region on the anode target. X-rays are generated by Bremsstrahlung during this process, in which only 1% of the electron energy is converted into photon energy, and 99% of the electron energy becomes heat. To further increase the impact area and dissipate heat more quickly, the rotating anode is designed to allow a focal track (Hsieh, 2009). The size and shape of the focal spot contribute to the resolution of the system. The spatially variant resolution in CT is largely due to the location-dependent appearance of the focal spot size and shape. The polychromatic X-ray beam hardness, i.e., its penetration capacity can be varied by changing the tube voltage, and the beam intensity can be controlled via the tube current.

X-ray generator and control circuits

The X-ray generator is the energy source that supplies high voltage to accelerate electrons in the X-ray tube. The X-ray beam is controlled through adjustment of tube voltage, tube current and exposure time through control circuits.

Collimators and bowtie filter

To reduce unnecessary radiation dose to the patient and to ensure good image quality, collimators are usually used, both pre-patient and post-patient. Pre-patient collimation is used to restrict the wide range X-ray flux to a narrow region in the z (axial) direction. Post-patient collimations are usually employed to reject scattered X-ray photons. The bowtie filter is a shaped filter used between the X-ray source and patient to modify the X-ray beam intensity across the Field of view (FOV) to reduce the patient dose peripherally.

Gantry, slip ring and brushes

The gantry is the backbone of a CT system. For modern CT scanners, the gantry performance should be stable within a fraction of millimeter for all projection angles with a large load on the rotating part. The slip ring takes care of data transmission, using a Radio Frequency (RF) signal. The power is transmitted through brushes.

Detector

Generally, there are three types of X-ray detectors: high-pressure inert gas (usually xenon), solid state scintillators coupled with photodiodes (e.g., CdWO₄, Gd₂O₂S, etc.), and newly developed semiconductor direct-conversion (e.g., Se, CdTe, or CdZnTe, etc.) detectors. For third generation

CT scanners, the most commonly used detectors are solid state scintillators due to their high quantum detection efficiency (QDE) and high count rate performance. For solid state detectors, an incident X-ray photon undergoes a photoelectric interaction with the scintillator. Then, the generated photoelectron travels a short distance in the scintillator and excites electrons in other atoms. These excited electrons return back to the ground states by releasing characteristic radiation in the visible or UV light spectrum. The decay process is characterized by the primary speed of the scintillator. The primary speed of the detector may affect the reconstructed image resolution. There are several key parameters describing detector performance, such as quantum detection efficiency, gain, thermal stability and primary speed. Details about detector can be found in reference (Bushberg, 2002).

Data Acquisition System (DAS)

In CT, the measured signal is a combination of the detector's analog signal and the digital signal obtained from the data acquisition electronics. Unlike the photon counting performed on the nuclear medicine scanners, the sampled projection in CT represents the energy-integrated X-ray photon flux over the sampling period. Thus, DAS works as an integrator over energies and time.

Data conditioning and reconstruction

The measured data, which represents the line integral of the attenuation coefficient of object along particular ray path for each view, is recorded as a sinogram. Then, a series of conditionings, such as channel-by-

channel calibration, logarithmic conversion, and correction steps are performed on the measured data. Finally, image reconstruction, such as filtered back projection will be used to reconstruct the attenuation image for display. There are various algorithms proposed for image reconstruction, as described in references (Buzug, 2008; Krestel, 1990).

Data visualization

The final value of the X-ray CT image is represented as CT number, given in Hounsfield Units or HU. The definition of the CT number is

$$CT_{number} = \frac{\mu - \mu_{water}}{\mu_{water}} \times 1000 \quad (2.8)$$

On this scale, a CT number of -1000 is assigned to air and a value of 0 HU to water. The CT values of water and air are independent of the X-ray tube voltage. Lung tissue and fat exhibit negative CT values due to their lower density. Most other body tissues (muscle, connective tissues, and most soft tissue organs) exhibit positive CT values, largely due to the increased physical density compared to that of water. The CT values of bone or contrast media are more strongly dependent on X-ray energy due to the dominated photo-electric absorption for these materials at the X-ray CT energy range, in addition to the physical densities of these materials. The CT Hounsfield value has a large range (e.g., -1024 to 3071 HU), and cannot be evaluated or differentiated in a single view, neither on a monitor nor by documentation on film (Kalender, 2000). Typically, only a maximum of 60-80 gray levels can be discerned up by human observers. Therefore, proper windowing of the color scale is important when displaying the reconstructed CT images.

2.2.2 X-ray generation and detection

From X-ray generation to the final image representation, the data processing flow in each stage can be illustrated in the following Figure 2.7.

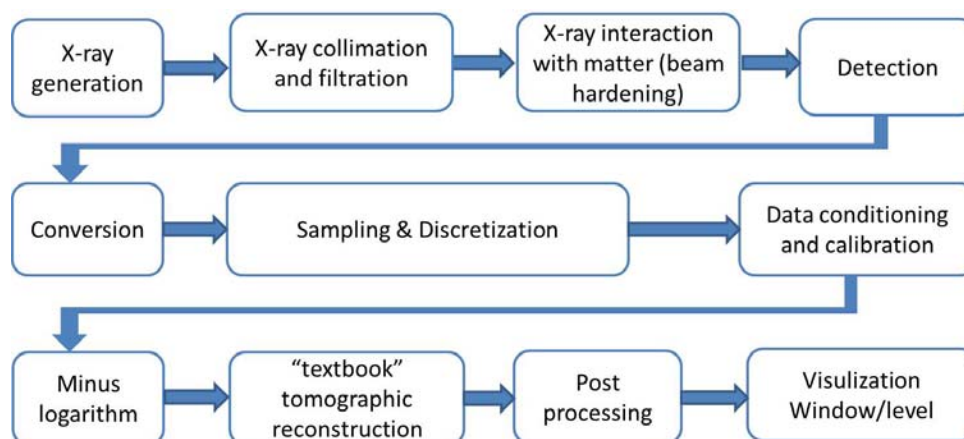


Figure 2.7 Schematic illustration of data processing steps in X-ray CT systems.

During X-ray generation and detection, there are some important physical effects, such as beam hardening, scatter, noise, detector afterglow and crosstalk. Here is a brief discussion of these major physical effects. More details can be found elsewhere (Hsieh, 2009; Buzug, 2008; Bushberg, 2002).

Bremsstrahlung

Bremsstrahlung is the physical effect responsible for the generation of X-ray radiation by the deceleration of a charged particle (electron) when deflected by another charged particle (the atomic nucleus of the tungsten anode).

Attenuation

Some of the X-ray photons are absorbed or scattered through

interactions (photoelectric, Compton and coherent scatter) when they pass through objects. That is to say, X-ray photons are attenuated. The primary goal of X-ray CT imaging, in essence, is to measure material attenuation. Detailed descriptions of X-ray attenuation can be found in other subsections in this chapter.

Beam hardening effects

Beam hardening effects are caused by the polychromatic nature of the X-ray source spectrum and energy dependence of the linear attenuation coefficient. When polychromatic X-rays pass through materials, lower energies photons will preferentially be attenuated. This causes the X-ray spectrum to have, on average, higher photon energies. This is referred to as beam hardening. Mathematically, the Bouger-Lambert-Beer law would be written as:

$$I(x') = I_0 \int_0^{E_{\max}} \Omega(E) \exp\left(-\int_0^{x'} \mu(E, s) ds\right) dE \quad (2.9)$$

Where $\Omega(E)$ represents the incident X-ray spectrum, the area under $\Omega(E)$ equals unity, and I_0 and I represent the total incident and transmitted intensities, respectively. Beam hardening could induce artifacts, such as cupping (Brooks and Di Chiro, 1976; Weidenmaier and Christ, 1985; Alles and Mudde, 2007).

Scatter

As mentioned in the previous section, there are two main mechanisms that account for X-ray photon attenuation: photoelectric absorption and

Compton scattering. Because of Compton scatter, not all of the X-ray photons that reach the detector are primary photons. Scattered photons make the detected signals deviate from the true measurement, cause either CT number shifts or shading/streaking artifacts in the reconstructed image (Endo *et al.*, 2001; Ning *et al.*, 2000; Siewerdsen and Jaffray, 2001; Glover, 1982) and add noise. Scatter can lead to reduced image contrast and a reduction in the signal to noise ratio of the final image.

Noise

In CT imaging, in general, the noise is defined as (pseudo-)random fluctuations. There are three possible sources of image noise. The first source of noise is quantum noise, determined by detected X-ray flux. The second source of noise is electronic noise, determined by inherent physical limitations of the system. The third source of noise is quantization noise, determined by the data processing steps.

Detector afterglow

The detector afterglow effect is due to the longer decay time constant needed in the X-ray detectors when excited electrons return to their ground states to produce light. Detector afterglow contributes to image artifacts such as shading and rings, because of the channel-to-channel variation in the afterglow characteristics (Hsieh *et al.*, 2000).

DAS crosstalk

Crosstalk is the amount of signal that leaks between adjacent detector channels and can be one of three types: x-ray, optical or electronic crosstalk.

Crosstalk may impact the spatial resolution and produce artifacts. Current CT designs are specified to reduce the level of crosstalk below an acceptable level.

2.3 CT based PET attenuation correction

As mentioned in the previous chapter, an important synergy of PET/CT scanners is the use of the CT images for attenuation correction of the PET emission data (Kinahan *et al.*, 1998). All manufacturers of PET/CT scanners incorporate X-ray CT based attenuation correction algorithms in their systems, and for some PET/CT scanners, it is the only option offered (Kinahan *et al.*, 2003; Alessio *et al.*, 2004; Messa *et al.*, 2004).

Compared with methods using positron sources or gamma-ray sources (for example, ^{137}Cs) to acquire transmission data for PET attenuation correction, CT based attenuation correction methods offer significant advantages (Kinahan *et al.*, 2003). First of all, compared with transmission data acquired with radionuclide sources, the data acquired with X-ray CT will have much lower statistical noise. Second, the X-ray CT scan requires much shorter time for acquisition than a standard PET transmission scan. Third, the X-ray CT scan enables collecting of uncontaminated post-injection transmission scans. Radionuclide-based transmission scans suffer contamination from emission photons unless the transmission data are acquired before the PET agent is administered to the patient. In contrast, CT transmission scans can be acquired anytime after the PET tracer is injected due to the fact that the X-ray photon flux is orders of magnitudes higher than

the emission photon flux. This is an important practical consideration, which shortens the time spent by a patient on the scanner bed and provides more efficient use of scanner time by allowing overlapping of patient protocols. Last but not the least, the need for PET transmission hardware and the periodic replacement of $^{68}\text{Ge}/^{68}\text{Ga}$ positron sources can be eliminated by using X-ray CT scan. A detailed comparison of PET attenuation correction methods is given in Figure 2.8 and Table 2.3 (Kinahan *et al.*, 2003).

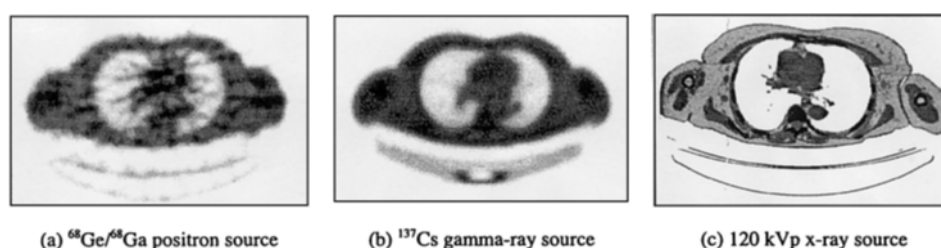


Figure 2.8 Anecdotal illustrations of the three transmission methods used for measured attenuation correction for PET. In these images, darker regions correspond to higher density (ie, bone) (Kinahan *et al.*, 2003)

Table 2.3 Comparison of the three transmission methods used for measured attenuation correction for PET (scan times are approximate and estimated for an axial range of 75 cm) (Kinahan *et al.*, 2003).

Source	Positron	Single Photon γ Ray	X-Ray
Photon energy (keV)	511	662 (for ^{137}Cs)	polyenergetic: ~30 to 140
Patient scan time (min)	~15-30	~5-10	~1
Transmission noise	highest	high	insignificant

Potential for bias/artifacts	low	some	highest
------------------------------	-----	------	---------

2.3.1 Principles of CT based PET attenuation correction for PET

The goal of CT-based attenuation correction is to use a polychromatic X-ray spectrum to estimate the attenuation coefficient at the PET monochromatic energy. There are two major considerations for CT based attenuation correction.

First, there are large differences between source energies from transmission CT scan and emission PET scan. The CT source uses wide band polychromatic spectra ranging from 40 keV to 140 keV, while PET uses the monochromatic energy of 511 keV.

Second, the attenuation effect of materials at CT energy spectra is the combination of photoelectric absorption and Compton scattering. Especially for bone, photoelectric absorption dominates in the low CT energy ranges. However, at the higher energy of 511 keV, the contribution of photoelectric absorption is essentially negligible for all biological materials (Bushberg, 2002). Figure 2.9 shows a plot of the mass attenuation coefficient for different materials and the corresponding energy range for CT and PET.

Thus, when used to correct PET emission data for photon attenuation, attenuation coefficients measured with X-ray CT must be converted to the appropriate values at 511 keV.

Once the attenuation map, $\mu(x, y, z)$, at the correct energy is obtained,

the attenuation correction factor, $\alpha(x', \phi)$, for an individual sinogram element is calculated by numerically integrating $\mu(x, y, z)$, along the LOR corresponding to the emission sinogram element (Eq. 2.6). Figure 2.10 summarizes the use of CT for PET attenuation correction.

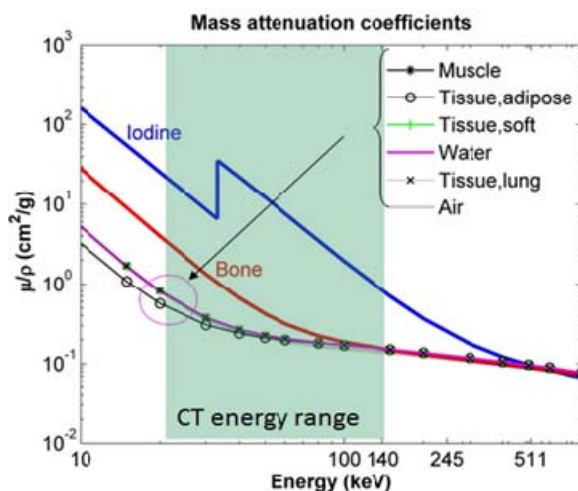


Figure 2.9 Mass attenuation coefficients for different materials as a function of energy. Note that the light green region is the X-ray CT energy range.

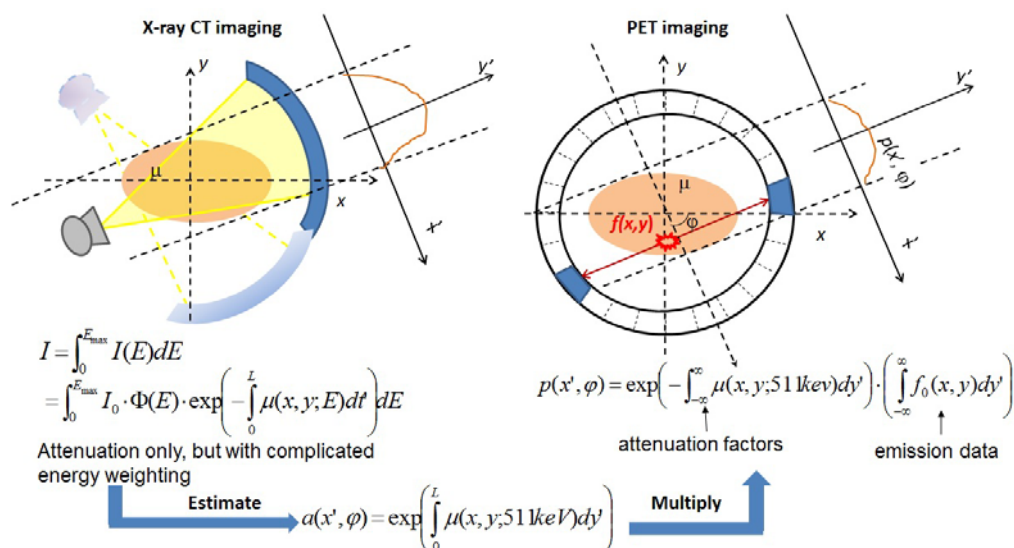


Figure 2.10 Using transmission X-ray CT imaging for attenuation correction of PET emission data.

2.3.1.1 Data flow for CT based attenuation correction

The data flow for CT based attenuation correction is shown in Figure 2.11.

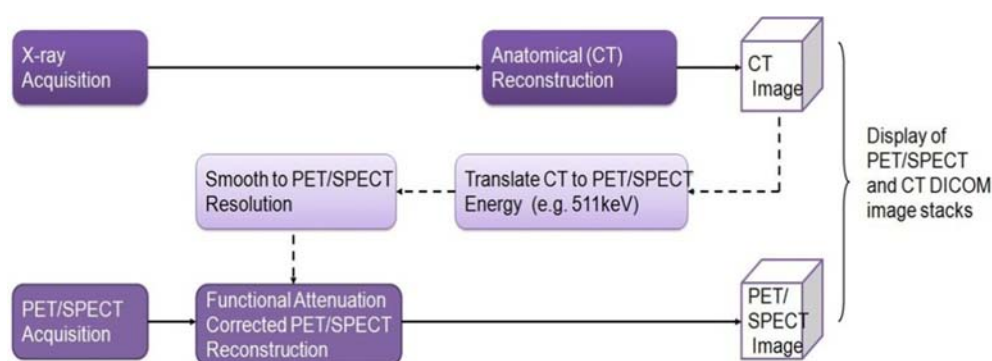


Figure 2.11 Dual modality PET/CT structure (also shown is SPECT/CT structure, which is similar to PET/CT)

2.3.2 Methods for CT based attenuation correction (CTAC)

In general, there are three methods considered for converting a CT image to attenuation coefficients at 511 keV: segmentation, scaling, and dual-energy X-ray scans. This section provides a brief discussion of each method. Detailed descriptions of each method can be found in the review paper by Kinahan (Kinahan *et al.*, 2003) and in Chapter 11 of the book (Wernick and Aarsvold, 2004).

Segmentation

The segmentation method can be used to separate the CT image into regions corresponding to different tissue types, which are then replaced with appropriate attenuation coefficients at 511 keV. There are some limitations of the segmentation method. First, some tissue regions with continuously-varying densities will not be accurately represented by a discrete set of

segmented values (Robinson and Kreel, 1979). Second, the increased noise of low-dose CTAC scans can result in misclassification of voxels, with incorrect attenuation coefficients being assigned. For these reasons, segmentation methods have not been adopted for CTAC transforms, although they may have some application for the correction of focal accumulations of CT contrast agents (Nehmeh *et al.*, 2003).

Scaling

For low Z materials, it is possible to use a simple linear scaling method. The attenuation map of the patient at 511 keV can be estimated by multiplying the entire CT image by the ratio of attenuation coefficients of water (representing soft tissues) at the photon energies of CT and PET. For high atomic number materials and dense materials such as bone, however, linear scaling only provides a poor approximation, because photoelectric absorption dominates Compton scatter at the lower range of CT energies (Lacroix *et al.*, 1994; Blankespoor *et al.*, 1996). Bilinear scaling was used by Blankespoor *et al.* (Blankespoor *et al.*, 1996) to convert CT images to 140 keV for attenuation correction of SPECT data. In this method, different scaling factors (for water and air mixtures, and for water and bone mixtures respectively) are used to calculate the attenuation values for CT numbers H for which $-1000 < H < 0$, and for $H > 0$. This approach was proposed for PET by several groups (Burger *et al.*, 2002b; Bai *et al.*, 2003b). In the hybrid scaling method (Kinahan *et al.*, 2003) the attenuation map at 511 keV is estimated by first using a threshold to separate out the bone component of the CT image. Then separate scaling factors for the mass attenuation coefficients of the bone and

non-bone components are used. Both the bilinear scaling and hybrid methods have been shown to give reasonable results for low-Z biological materials in practice (Beyer *et al.*, 2000b; Charron *et al.*, 2000; Beyer *et al.*, 2002; Burger *et al.*, 2002a; Kamel *et al.*, 2002; Nakamoto *et al.*, 2002). For high-Z materials such as contrast agent, however, there are some different opinions in the published literature. Some papers report no significant errors introduced by high-Z materials if scaling methods were used (Dizendorf *et al.*, 2003), while others have reported significant quantitative errors (Antoch *et al.*, 2003; Bujenovic *et al.*, 2003; Goerres *et al.*, 2003b; Nakamoto *et al.*, 2003; Visvikis *et al.*, 2003; Nehmeh *et al.*, 2003). Figure 2.12 shows an example of a multi-linear scaling function.

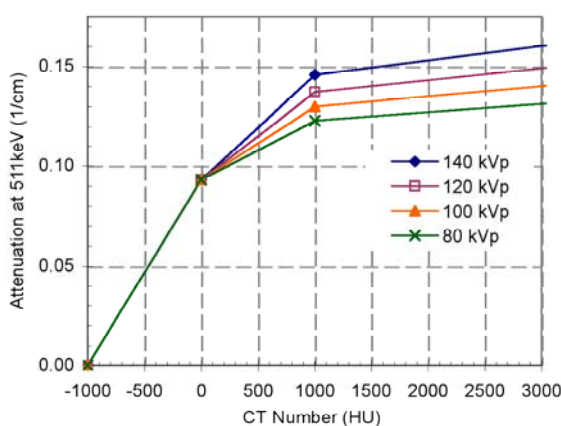


Figure 2.12 Multi-linear conversion of CT image values to linear attenuation coefficients for CT-based attenuation correction (CTAC).

Dual energy CT

As mentioned in section 2.3.1, the X-ray source generates a polychromatic wide band spectrum. The measured attenuation value for a material is a weighted average of attenuation in this X-ray energy range as

shown in Figure 2.9. Thus, a measured CT number can be invariant for changes in density and atomic properties of materials, which can be seen in Figure 2.13 (Schneider *et al.*, 2000). This means that different combinations of material density and atomic properties can result in the same CT value. This will be problematic for PET attenuation correction of materials with high atomic number. For example, with the bilinear/trilinear scaling methods described in the previous section, it would cause estimation bias if both bone and contrast agent are present for PET attenuation correction.

Dual energy CT can be used for accurate attenuation correction of PET data involving materials with high atomic number (Kinahan *et al.*, 2006a). In this method, the attenuation coefficient of any material is regarded as a weighted sum of photoelectric absorption and Compton scattering probabilities (Alvarez and Macovski, 1976), in essence a system with two components (Lehmann *et al.*, 1981). If we were able to determine the individual photoelectric and Compton components by two kVp CT scans, they could be scaled separately to any energy and then added to obtain the total attenuation coefficient at that arbitrary energy. Such a quantitative CT imaging process was developed by Alvarez and Macovski and further extended for attenuation correction in SPECT/CT by Hasegawa (Hasegawa *et al.*, 1993; Guy *et al.*, 1998).

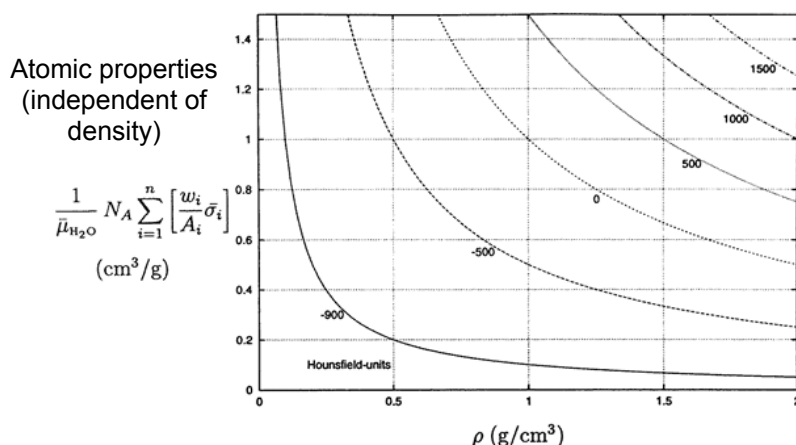


Figure 2.13 A measured CT number can be invariant for changes in density vs. atomic properties (Schneider *et al.*, 2000).

2.4 Radiation Dose

The total PET/CT radiation dose is the sum of the doses from PET and CT procedures. The radiation dose delivered to a patient during a CT exam varies widely, depending on the patient size, the machine characteristics, technical factors used for the examination, and the type of procedure (organs scanned) (Wernick and Aarsvold, 2004). The radiation dose to the patient during the PET part of the procedure does not depend directly on the PET scanner, but only on the injected radiopharmaceutical. Estimates of effective dose for ^{18}F -FDG PET scanning can be found in many publications. It has been reported that a mean effective dose of ^{18}F -FDG is 0.029 ± 0.009 mSv/MBq (Deloar *et al.*, 1998; ICRP, 1998). A comprehensive report on ^{18}F -FDG absorbed dose estimates using the Medical Internal Radiation Dose model alternative may be found in Hays *et al.* (Hays *et al.*, 2002). Table 1.1 provides a detailed summary of Radiation doses from PET/CT and CT scans. This section will first give terminologies for radiation dose measurement,

especially CT radiation dose measurement, and then give the background about biological effects of radiation.

2.4.1 Terminology and the measurement standards

In this section, for the ease of understanding, different terminology and measurement standard for radiation dose are briefly reviewed. During the interaction between X-ray photons and matter, energies are transferred from the X-ray photons to the matter. Therefore, the X-ray radiation dose measurement is simply a measure of the amount of energy transferred per unit mass during the interaction (McNitt-Gray, 2002).

Exposure

X-ray exposure is measured in unit of roentgen (R), which is defined as the amount of X-rays required to produce an electrostatic charge of 2.58×10^{-4} coulomb (C) in 1 kilogram of air at standard temperature and pressure. From the definition, exposure describes only the amount of ionization, not the amount of energy absorbed by the tissue being irradiated.

Absorbed radiation dose

Absorbed radiation dose (also called radiation dose) indicates the amount of energy absorbed per unit mass. According to the International Commission on Radiological Protection (ICRP) recommendation, absorbed radiation dose is measured in units of gray (Gy), in which one gray equals one J/kg.

Equivalent dose

The metric of equivalent dose considers the dependence of the harmful

biological effects on the type of radiation delivering the energy. A radiation weighting factor is assigned for different type radiation. For example, the absorbed dose deposited by alpha particles has greater biological effects than the same dose deposited by X-rays, thus a higher radiation weighting factor is assigned. For X-ray and γ -ray imaging, the radiation weighting factor is one.

$$\text{Equivalent dose} = \text{absorbed dose} \times \text{Radiation weighting factor} \quad (2.10)$$

Equivalent dose has the unit of sieverts (Sv), with 1 Sv= 1 J/kg.

Effective dose

In order to take into account of the tissue- or organ- specific radiation risks, the concept of effective dose E was introduced as the weighted sum of all equivalent doses to all the tissues.

$$E = \sum_s w_s D_s \quad (2.11)$$

Where the subscript S represents each tissue type; D_s is the average absorbed dose to tissue S, and w_s is the tissue-weighting factor. The tissue weighting factors to be used for calculation of the effective dose can be found in reference ICRP No. 103 (ICRP, 2007). Similar to equivalent dose, the measurement unit for effective dose E is sieverts (Sv).

Computed Tomography Dose Index (CTDI)

CTDI was introduced to account for the fact that the majority of CT scans performed in a clinical environment consist of multiple scans. When multiple scans are performed in the adjacent regions, X-ray dose from nearby scans also contributes to the dose to the current location, due to the long tails

of the dose profile in z (perpendicular to the cross-section) direction. The CTDI was originally defined:

$$\text{CTDI} = \frac{1}{nT} \int_{-\infty}^{\infty} D_a(z) dz \quad (2.12)$$

Where $D_a(z)$ is the dose function, n is the number of detector rows used during the scan, and T is the nominal thickness of each row. nT is the nominal X-ray beam width during the data acquisition. In practice, the above definition is impractical for measurement.

CTDI_{FDA}

CTDI_{FDA} is originally codified in the U.S. Code of Federal Regulations:

$$\text{CTDI}_{FDA} = \frac{1}{nT} \int_{-7T}^{7T} D_a(z) dz \quad (2.13)$$

Where $D_a(z)$ is the dose absorption distribution in z , n is the number of detector rows used during the scan, and T is the nominal thickness of each row (not necessarily equal to the reconstructed slice thickness). The quantity nT , is the nominal X-ray beam width during the data acquisition. Although the CTDI_{FDA} definition is convenient for practical measurement, it is problematic when T is small or n is large. This is due to the assumption in the definition that the region outside a width of 14 scans does not contribute significantly to the dose calculation.

CTDI_{100}

CTDI_{100} measures the dose per unit length in the z direction (perpendicular to the cross-section), which is measured in the standard poly-

methacrylate (PMMA) phantoms.

$$CTDI_{100} = \frac{1}{nT} \int_{-50mm}^{50mm} D_a(z) dz \quad (2.14)$$

Where $D_a(z)$ is the dose absorption distribution in z for a single axial scan, n is the number of detector rows used during the scan, and T is the nominal thickness of each row (not necessarily equal to the reconstructed slice thickness). The quantity nT , is the nominal X-ray beam width during the data acquisition.

$CTDI_w$

During a CT scan, the interior region of the object being irradiated is always partially “shielded” by the outer portion of the object. To account for the spatial variation of the dose distribution in the cross-section, a weighted dose index, $CTDI_w$, which combines dose information at different locations, is introduced:

$$CTDI_w = \frac{1}{3} CTDI_{100}(central) + \frac{2}{3} CTDI_{100}(peripheral) \quad (2.15)$$

$CTDI_{vol}$

The definition of $CTDI_w$ considers only the X-ray exposure for a step-and-shoot scan, and does not take into account the X-ray dose received when a helical scan is performed. For helical scan mode, the parameter that measures how fast the patient table travels while data collection takes place is the helical pitch, defined as the ratio of the table traveling distance in one gantry rotation over the nominal beam width. Thus, $CTDI_{vol}$ is introduced as:

$$CTDI_{vol} = \frac{CTDI_w}{pitch} \quad (2.16)$$

Dose-length product (DLP)

Dose-length product (DLP) is established with the unit in mGy × cm to account for the integrated dose for the entire CT exam:

$$DLP = CTDI_{vol} \times L \quad (2.17)$$

where L is the scan length in z. For a helical data acquisition, L is the total scan length, not the reconstructed length in z.

Approximate effective dose in CT

As described earlier, the sensitivities of human organs to the X-ray dose are different and organ-dependent. Thus, to different organs, there are different risk levels if the same amount of X-ray radiation is given. As given by equation (2.10), effective dose needs to be calculated to take this into account. To determine specific organ dose, Monte Carlo simulation can be used, in which the absorption and scattering of X-ray photons in various tissues is simulated by using a mathematical model of the human body (Hsieh, 2009). More often, a fast approximation for the effective dose in CT is given in clinical environment (Hsieh, 2009):

$$Dose_{effective} = k \times DLP \quad (2.18)$$

where k is a conversion factor in mSv × mGy⁻¹ × cm⁻¹ that varies depending on the imaged body region. Table 2.4 gives some conversion factors.

Table 2.4 Conversion factors for effective dose estimation from DLP for different anatomies. (Cited from NCRP Report No.160).

Region of Body	K (mSv mGy ⁻¹ cm ⁻¹)
Head	0.0021
Neck	0.0059
Chest	0.014
Abdomen	0.015
Pelvis	0.015

Multiple-scan average dose (MSAD)

Multiple-scan average dose (MSAD) was defined to account for the dose increase in the multiple-scan mode (Hsieh, 2009) before the introduction of $CTDI_{100}$:

$$MSAD = \frac{1}{l} \int_{-l/2}^{l/2} D_{N,l}(z) dz \quad (2.19)$$

where the subscript N stands for N scans, l is the distance between adjacent scans, and $D_{N,l}(z)$ is the dose as a function of the distance z .

2.4.2 Biological effects of X-ray and PET radiation

During the passage through living matter, X-ray radiation loses energy by interaction with atoms and molecules of the matter, and causing ionization and excitation. In general, complex organisms exhibit more sophisticated repair mechanisms. Responses seen at the molecular or cellular level may or may not result in adverse clinical effects in humans. Furthermore, although some responses to radiation exposure appear instantaneously, others take

weeks, years, or even decades to appear. This section briefly describes the biologic effects of X-ray radiation (Bushberg, 2002).

2.4.2.1 Classification of biologic effects

In general, biologic effects of radiation can be classified as either stochastic or deterministic.

Stochastic

For a stochastic effect, the probability of the effect, rather than its severity, increases with radiation dose (Bushberg, 2002). Radiation-induced cancer and genetic effects are stochastic in nature. It is believed that stochastic effects do not have a dose threshold since the radiation damage to a few cells or a single cell could theoretically induce a genetic disorder or cancer, the severity of which will be the same if it ever occurs. Based on the assumption that risk increases with radiation dose and there is no threshold radiation dose below which risks cease to exist, the principle of keeping exposures as low as reasonably achievable (ALARA) was proposed. The principal health risk from exposures of diagnostic imaging, including X-ray CT is regarded as stochastic effects. The effects from medical imaging are almost stochastic effects.

Deterministic effects

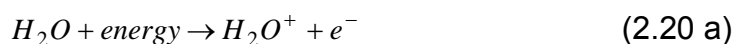
The deterministic or non-stochastic effects are induced by high radiation doses and the severity of the damages, rather than their probability of occurrence, increases with the radiation dose (Saha, 2006). Deterministic effects have a threshold radiation dose below which no damage is evident.

Deterministic effects are different from stochastic effects in that they require high radiation dose.

2.4.2.2 Interaction of radiation with tissue

Direct and indirect interactions

Two types of radiation interactions could produce biological changes: direct and indirect interaction (Bushberg, 2002). In direct interaction, a biologic macromolecule such as DNA, RNA, or protein becomes ionized or excited by an ionizing particle or photon passing through or near it. In indirect interaction, the radiation hits the medium (e.g., cytoplasm) which create reactive chemical species that in turn interact with the target molecule. Most of the radiation-induced damage from medical imaging is mediated through indirect action on water molecules, which produces free radicals, because 70% to 85% of the mass of living systems is composed of water. Free radicals are characterized by an unpaired electron in the structure, which is very reactive, and could react with DNA later to cause structural damage. Here are some typical reactions of radiation with water that produce free radicals and may do harm to cells:





The physical steps that lead to energy deposition and free radical formation occur within 10^{-5} to 10^{-6} seconds, whereas the biologic expression of the physical damage may occur seconds or decades later (Bushberg, 2002).

Radiation effects on DNA and/or chromosome

Radiation damage to the DNA molecule can be due to: a) loss of a base, b) cleavage of the hydrogen bond between bases, c) breakage of one strand of the DNA molecule (single strand) and d) breakage of both strands of the DNA molecule (double strand). At low-dose exposures, the breaks are mostly single stranded and the cell can self-repair by joining the broken components; at higher exposures, double strand breaks may occur and the odds for cellular self-repair decrease.

Although DNA mutations may result in serious implications, they do not necessarily lead to structural changes in chromosomes. However, there are some cases where chromosomes can be cleaved by radiation producing single or double breaks in the strands.

Radiosensitivity of cells

In living matter, there are two types of cells, differentiated and undifferentiated. It has been reported that undifferentiated cells that are undergoing active mitosis are most sensitive to radiation, and differentiated or mature cells are least affected by radiation. Different types of cells and their radiosensitivity can be found in references (Saha, 2006). A tissue or organ

that contains more radiosensitive cells will be highly radiosensitive.

2.4.2.3 Long-Term effects of Radiation

Ionizing radiation can cause damage whose expression is delayed for years or even decades. Depending on the respective cells involved, long-term effects of radiation may be somatic or genetic. Somatic effects are seen in the form of carcinogenesis, life-shortening, or cataractogenesis. A detailed description of carcinogenesis due to radiation and risk models can be found in references (Bushberg, 2002). Genetic effects are effects of radiation that are expressed in future generations when the patient's germ cells have been affected by radiation. It is reported that genetic effects may appear as Down syndromes, achondroplasia, retinoblastoma, cystic fibrosis, and some other chromosome disorders.

Chapter III: Tool development

This chapter introduces the simulation tools and development of the tools used for studies in the following chapters.

3.1 Introduction of CT simulator

Computer Assisted Tomography SIMulator (CATSIM) was used for the simulation of the X-ray CT imaging (De Man *et al.*, 2007). It includes a Monte Carlo based simulation package called CATDOSE for estimation of the CT radiation dose. Both CATSIM and CATDOSE have been validated relative to GE Lightspeed Volumetric Computed Tomography (Lightspeed VCT, General Electric Medical Systems, Waukesha, WI) measurements for a series of properties. The CT simulation models the effects of the X-ray source focal spot, polychromatic tube spectra, beam conditioning, bowtie filter, beam hardening, detector noise and scatter. Although fully described elsewhere, this section provides a brief summary of the properties modeled by CATSIM (De Man *et al.*, 2007).

CT raw data y_i at sinogram index i , are formed from the combination of a quantum noise process p_i and electronic noise process z_i , i.e., $y_i = p_i + z_i$, following methods described by (De Man *et al.*, 2007), similar to the methods described by others (La Riviere, 2005; Whiting *et al.*, 2006). The quantum noise is modeled as:

$$p_i = \left[\sum_k E_k \cdot x_{ik} \right] f_C \quad (3.1)$$

Where E refers to photon energy, k is the energy bin index, f_C is a

factor to convert from keV to the number of electrons, and x_{ik} is a Poisson random process with parameter λ_{ik} , $x_{ik} \sim \mathbb{P}(\lambda_{ik})$, where

$$\lambda_{ik} = \eta \cdot A_{ik} \cdot \sum_s \frac{1}{S} \exp(-\sum_o l_{iso} \mu_{ok}) + y'_{ik} \quad (3.2)$$

Where η is the detector quantum efficiency (fraction of photons absorbed), A_{ik} is the number of photons arriving at the detector without attenuation for energy bin k , s is the beam sub-sampling index for the total of S sub-beam samplings, l_{iso} is the intersection length between the line with index is and the object element with index o , μ_{ok} is the linear attenuation coefficient of object at o at energy k , and y'_{ik} is the estimated scatter at sinogram index i with energy index k .

The electronic noise z_i is modeled as a Gaussian random process, $z_i \sim \mathcal{N}(d, \sigma_e^2)$, where d is the dark current, and σ_e , is the standard deviation of the electronic noise.

The current version of CATSIM is written in FreeMat (m-files) and C (c-files) to allow both flexibility and computational efficiency. It can be run in both Windows and Linux operating systems. The CT architecture, physics and acquisition are written in FreeMat, while the projectors are written in C. The two levels (M- and C-code) communicate with each other through a clearly defined interface. For the work in this dissertation, both the analytical projector and NCAT (NURBS-based cardiac-torso) projector (Segars, 2001; Segars *et al.*, 2008) have been used.

3.2 Introduction of PET simulator

The PET images were simulated using a simplified version of whole-body analytical simulator (ASIM)² (Comtat *et al.*, 1999), which included the physical effects of attenuation, background noise, and photon counting. Unlike the Monte Carlo based simulators (e.g., SIMSET) using photon tracking to model physical effects, ASIM calculates noiseless line integrals, followed by addition of Poisson noise into the raw sinogram data. The advantage of this simulator is that multiple independent and identically distributed (i.i.d) realizations of data can be rapidly generated using ASIM. The noisy prompt coincidences \tilde{p} follow a Poisson pseudo-random process with mean m , ($\tilde{p} \sim \mathbb{P}(m)$), defined as

$$m = \alpha_t \cdot t + \alpha_b \cdot b \quad (3.3)$$

where t represents the true coincidences; b is the background noise including scattered and random coincidences; and α_t and α_b are global scale factors for true coincidences and background noise, respectively.

3.3 Development of tools for CATSIM

For the study in this dissertation, CATSIM collaborator version 3.20b in windows operating system with FreeMat v3.6 has been used. To fully use CATSIM for the study in this dissertation, some modification and development of the tool have to be done by the user. The following subsections list the

² <http://depts.washington.edu/asimuw>

development of the tools for CATSIM that has been done in University of Washington.

3.3.1 Generation of material files for CT contrast agent (iohexol)

We successfully derived the material files of CT contrast agent Omnipaque 300® (iohexol, Omnipaque package insert, GE healthcare, USA) with varying concentrations for CATSIM simulations.

Iohexol, *N,N'*-Bis(2,3 - dihydroxypropyl)- 5- [N - (2,3 - dihydroxypropyl)- acetamido] - 2,4,6 - triiodoisophthalamide, is a nonionic, water-soluble radiographic contrast medium with a molecular weight of 821.138 ($C_{19}H_{26}I_3N_3O_9$, iodine content 46.36%). In aqueous solution each triiodinated molecule remains undissociated. The chemical structure for iohexol is illustrated in Figure 3.1.

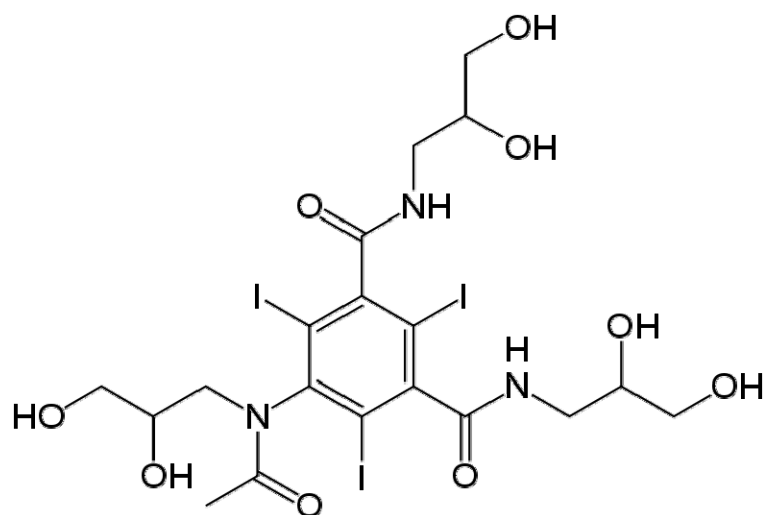


Figure 3.1 Chemical structure of iohexol

Each 1ml of Omnipaque 300® contains 647.1 mg of iohexol (300 mg organically bound iodine), 1.21 mg tromethamine $((HOCH_2)_3CNH_2$, with molecular weight 121.14) and 0.1 mg edentate calcium disodium (EDTA:

$C_{10}H_{12}CaN_2Na_2O_8$). In order to study the CT-based PET attenuation correction of contrast at different concentration, material files of Omnipaque 300 ® of varying concentration according to table 3.1 were generated based on an equation of the x-ray mass attenuation coefficient for mixtures and compounds (Eq. 3.4).

$$\frac{\mu}{\rho} = \sum_i w_i \left(\frac{\mu}{\rho} \right)_i \quad (3.4)$$

Where w_i is the fraction by weight of the i th atomic constituent, and $\left(\frac{\mu}{\rho} \right)_i$ values can be obtained from NIST.

For clinical CT usage, the dosage of Omnipaque 300 ® ranges from 15g I to 60g I. The iodine concentration in the body varies with injection rate, imaging organ and renal clearance rate. Contrast enhancement appears to be greatest immediately after bolus administration (15 seconds to 120 seconds).

Table 3.1 Contrast agent Omnipaque 300 ® diluted in water solution with varying concentrations

Solution	Solution #1	Solution #2	Solution #3	Solution #4	Solution #5	Solution #6	Solution #7	Solution #8
	(pure)	(1:5)	(1:10)	(1:20)	(1:50)	(1:100)	(1:500)	(1:1000)
Iodine								
Concentration	300	60	30	15	6	3	0.6	0.3
(mg I/ml)								

The details of calculation and generation of these material files can be found in Appendix A.

3.3.2 Improvement of beam hardening correction function for multiple detector rows

As mentioned in the previous chapter, beam hardening is a common physical phenomenon in X-ray CT imaging. It is caused by the polychromatic X-ray beam spectrum and the energy-dependent attenuation coefficients. Beam hardening effects could induce inaccuracy in CT numbers, and lead to intensity cupping effects in the reconstructed CT images if no correction step is applied. For clinical CT, there is additional software used to correct for this. In the CATSIM collaborator version, there is no beam hardening correction function provided for multiple detector rows. Since over 80% of a human body is made of water, we developed a simple beam-hardening correction based on water for multiple detector rows. The detailed algorithm can be found in reference (Hsieh, 2009). In our version of the beam hardening correction function, we made modifications for it to work with low dose CT acquisition cases when there are extreme values due to photon starvation. One tested example with improved FreeMat code developed in this study is provided in Appendix B.

3.3.3 Improvement of Poisson random number generator in FreeMat

We found that the original spectra provided in CATSIM become distorted at photon starvation cases, especially for low kVp CT techniques. With careful investigation and discussions with GE experts, we found that the root cause was the FreeMat Poisson random number generator function `randp()`, which does not correctly handle a zero input. The CATSIM function has the check for positive values, but values that are positive in double precision and equal to zero in single precision slip through the cracks. The

problem is fixed by excluding numbers that would be truncated to zero on double to single float point conversion from the call to the FreeMat Poisson random number generator function randp().

3.3.4 Simulation of CATSIM with NCAT integration and contrast agent enhancement in the phantom

It was found that there was problem of coordinate mismatch with CATSIM collaborator version 3.20 when using NCAT phantom (Segars, 2001; Segars *et al.*, 2008) projector. An improvement of CATSIM providing the utility for user-input offsets to compensate for the coordinate mismatches was achieved by cooperating with GE Global Research Center. In addition, an NCAT phantom with liver contrast enhancement for CATSIM simulation was achieved and integrated into the package.

3.3.5 Modifications to CATSIM structure used for efficient generation of i.i.d. realizations

In the following studies of ultra-low dose CT for PET attenuation correction, we need to operate in a regime where noise and bias in the CT data impact the PET image, thus there are calls for multiple independent noisy realizations of CT data for the same object, as shown in Figure 3.2. However, the original CATSIM structure flow is not efficient for generating multiple realizations, especially for NCAT phantoms.

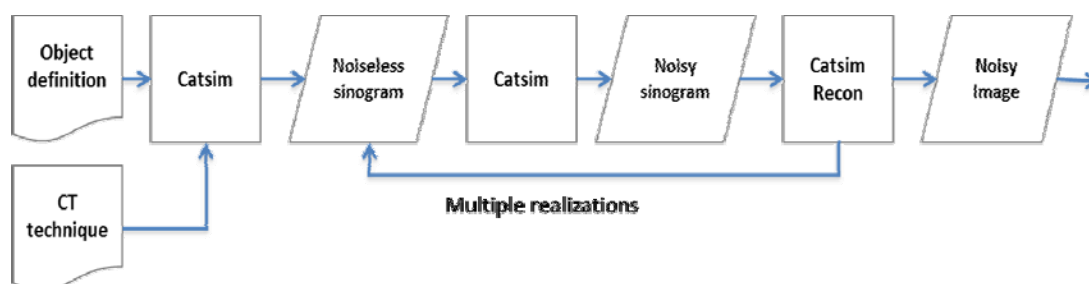


Figure 3.2 Overview of desired structure of CATSIM for multiple realizations.

The original CATSIM flow is as shown in Figure 3.3. In Figure 3.3, computation of attenuation based on projector (especially NCAT projector) is the most time consuming part of the process. It is not very fast for calculating projections for multiple realizations, for multiple mA levels, kVp filtration levels, and different added noise levels. The flow in Figure 3.3 has been modified in our tool development by calculating the “red box” for noise free case and saving the intermediate result for later use. Figure 3.4 shows the details of our strategy. The intermediate results are noise-free cases at given settings, photon counts at each energy bin at each detector element after photons penetrate the phantom. For the noise-free case kernel (compute attenuation), which is the most computationally expensive, we only need to calculate once, and save the results. Then for the same source and detector, phantom settings, we just need to calculate as the flow in the chart of part 2.

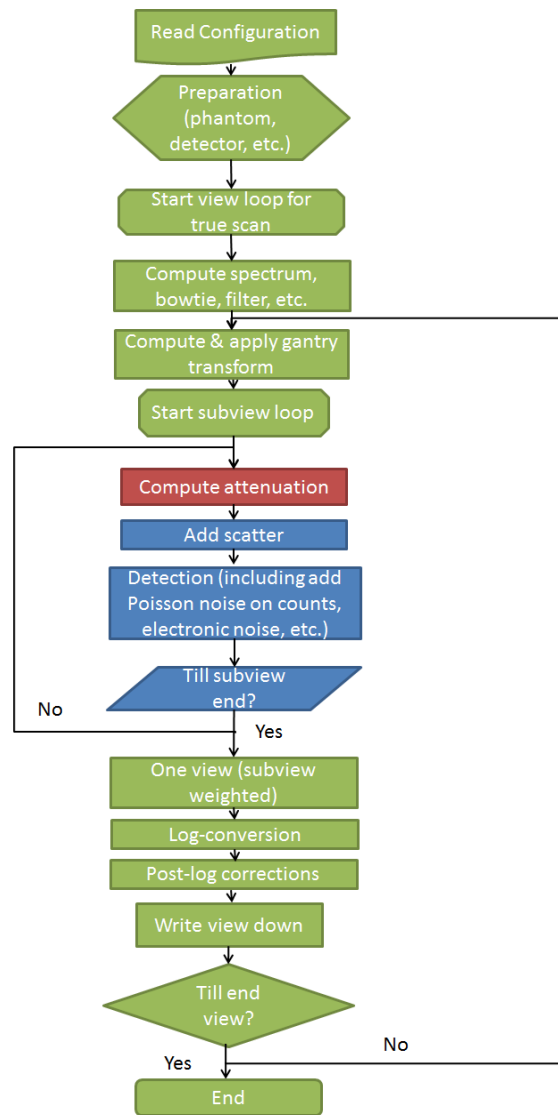


Figure 3.3 Original CATSIM structure flow.



Figure 3.4 Modified CATSIM structure flow (Left: Part 1) for calculating noise-free kernel; (Right: Part 2) for calculating noisy simulations for different mA levels, and /or multiple realizations.

3.3.6 Sinogram pre-processing with CATSIM

3.3.6.1 Development of boxcar smoothing function for CATSIM

In the following study of ultra-low dose CT based PET attenuation correction, to overcome increased CT noise and artifacts for low-dose regime,

a boxcar smoothing function based on FreeMat has been developed. Boxcar smoothing is also called the "moving average" which simply replaces each data value with the average of neighboring values. Both one dimensional, two dimensional, and three dimensional boxcar smoothing function with varying kernel sizes have been developed.

3.3.6.2 Development of adaptive trimmed mean filter for CATSIM

A FreeMat function for adaptive trimmed mean filter (ATM) according to Hsieh's paper (Hsieh, 1998) has also been developed with FreeMat for the sinogram pre-logarithmic conversion processing step and incorporated into CATSIM. The parameters for the filter are adjusted to the local statistical properties of the sinogram data using this method.

3.4 Summary and desired future functionalities

This chapter introduces the simulation tools of CATSIM and ASIM, and describes the developments and improvements of the tools that have been finished in University of Washington for performing studies in this dissertation. Both CATSIM and ASIM are very useful simulation tools for the CT and PET research. Both of them are projector-based simulators and could be used for generation of multiple independent and identically distributed (i.i.d.) realizations of data. Material files of CT iodine-based contrast agent have been generated. These material files are used for the CT contrast agent iohexol dissolved in water with varying concentrations. These material files can be integrated into CATSIM for future simulation. A water-only beam hardening correction function for multi-detector rows has been developed in FreeMat for CATSIM. The bug in Poisson random number generator in

FreeMat 3.6 has been identified and the corresponding modifications have been made in the CATSIM functions to avoid errors. We are able to use the NCAT phantom with iodine contrast enhancement in CATSIM. In addition, modification to the CATSIM structure flow has been proposed and implemented for generation of multiple CT realizations of the NCAT phantom. Furthermore, sinogram pre-processing functions with boxcar smoothing of varying window size and adaptive trimmed mean filter have been developed and incorporated into CATSIM collaborator version 3.20b.

Currently, though FreeMat can be freely downloaded, CATSIM is built on an older version of FreeMat, i.e. FreeMat 3.6. There have been incompatibility issues with the latest versions of FreeMat and CATSIM. Due to this challenge, it is desirable to switch the CATSIM platform from FreeMat to Matlab. CATSIM reconstruction options are limited, and it is desirable for more reconstruction algorithms that represent the latest ones used in actual scanners are provided. Although the material files for the CT contrast agent are only for water solutions, they are enough for the studies in this dissertation. However, it is desirable for material files for contrast agent dissolved in blood solution could also be calculated and generated. Due to the differences in algorithms between those in simulated software and those implemented in an actual scanner, the simulation results may not exactly replicate actual scanner reconstruction behavior with very noisy data. For example, CT image properties depend on treatment of non-ideal data in the low-dose regime, and it is desirable for the CATSIM simulator could be validated and characterized in this regime. For example, one desired future

direction is to match the low-dose measurement with simulations on the raw data. The current version of CATDOSE has the limitation of estimation of dose delivered to only simple objects, such as a uniform analytical elliptical water phantom rather than the NCAT phantom. It would be preferable if CATDOSE had the capability to deal with the NCAT phantom for dose estimation.

Chapter IV: Ultra-low dose CT for PET attenuation correction [†]

As already mentioned in Chapter I, a challenge for PET/CT quantitation is patient respiratory motion, which can cause an underestimation of lesion activity uptake and an overestimation of lesion volume. Several respiratory motion correction methods benefit from longer duration CT scans that are phase matched with PET scans. However, even with the currently available, lowest dose CT techniques, extended duration CINE CT scans impart a generally unacceptably high radiation dose. This chapter evaluates methods designed to reduce CT radiation dose in PET/CT scanning. In this chapter, selected combinations of dose reduced acquisition and noise suppression methods are investigated, taking advantage of the reduced requirement of CT for PET attenuation correction (AC). These include reducing CT tube current, optimizing CT tube voltage, adding filtration, CT sinogram smoothing and clipping. This chapter also studies the impact of these methods on PET quantitation via simulations on different digital phantoms.

4.1 Introduction

4.1.1 Extended duration CT scans for PET/CT imaging requires ultra-low dose CT techniques

One challenge of PET quantitation for lung cancer imaging is patient respiratory motion (Park *et al.*, 2008), which can cause an underestimation of standardized uptake values (SUV) and an overestimation of lesion volume

[†] Based on the work T. Xia, A. M. Alessio, B. D. Man, R. Manjeshwar, E. Asma and P. E. Kinahan, "Ultra-low dose CT attenuation correction for PET/CT," *Physics in Medicine and Biology* **57**, 309 (2012).

(Park *et al.*, 2008; Pevsner *et al.*, 2005; Liu *et al.*, 2009). Several groups have proposed methods to address the PET/CT quantitation problems caused by respiratory motion for lung imaging. For example, Kawano *et al.* and Nehmeh *et al.* proposed breath-hold methods, but these may be poorly tolerated by a large fraction of the population, particularly ill individuals (Kawano *et al.*, 2008; Nehmeh *et al.*, 2007). Other proposed methods include: respiratory gated 4D PET/CT (Nehmeh *et al.*, 2004a; Nehmeh *et al.*, 2004b; Pan *et al.*, 2004), post processing methods (Dawood *et al.*, 2006), and motion corrected PET reconstruction (Thielemans *et al.*, 2006; Qiao *et al.*, 2007; Qiao *et al.*, 2006; Li *et al.*, 2006; Kinahan *et al.*, 2006b). Most of these methods depend on accurate respiratory-gated CT images that are phase-matched with respiratory-gated PET images. When the CT data are acquired and reconstructed in a different respiratory phase than the PET data, there will be mismatches between CT and PET, leading to a degradation of the quantitative accuracy of the PET images. Such mismatches occur due to respiratory pattern variability (Liu *et al.*, 2009). Pan (Pan *et al.*, 2006; Pan *et al.*, 2007) and Chi (Chi *et al.*, 2007) have recommended CT acquisitions of 5-14 s per image plane to improve phase matching. This would increase patient radiation dose dramatically compared to current static acquisition protocols. For example, in order to image respiratory motion with CT, at least a 200 mm length of the thorax region needs to be scanned continuously for 5-6 seconds. Even while operating the CT scanner at its lowest possible setting (10 mA), this imparts an effective dose roughly of 2.7 mSv. If a longer duration (15 s) and extend cine scan range covering both thorax and upper abdomen region

(e.g. 400 mm) are required, this would increase the radiation dose over 3 times. When added with the whole body helical CT scan, even with current low dose protocols, the total radiation dose from CT would be substantially higher. Table 4.1 gives the typical patient radiation effective doses in PET/CT and CT imaging.

Table 4.1 Typical radiation doses from PET/CT and CT scans.

Type	Techniques	Effective Dose (mSv)	References
PET	Recommended administration 190 MBq ¹⁸ F-FDG (in 3D mode)	3.6 ^a	Boellaard <i>et al</i> 2010 (EANM guidelines)
Dx CT	Wide range of settings reported. Coverage: C+A+P	7 – 43	NCRP Report 160, 2009. Table 4.2
LD-HCT	110 – 120 kVp, 30 – 60 mAs, 0.75 – 6.5 mm slice collimation, 1.25 – 2.0 pitch. Scan axial coverage: 851 – 910 mm	1.3 – 4.5 Geometrical mean 2.4 Total for PET/CT: 6.0	(Brix <i>et al.</i> , 2005) Table 2
LD-CINE-CT	120 kVp, 5mAs, 8 × 2.50 mm collimation, 6s cine duration. Cine-CT scan coverage: 200 mm over thorax area	2.7 ^b	Pan <i>et al</i> 2006
LD-HCT + Ext LD-CINE-CT	Cine scan: 15 s duration with 400 mm axial coverage. HCT axial scan coverage: 900 mm	13.5 (cine-CT) + 2.4 (HCT) = 15.9 (all CT) ^b + 3.6 (PET) = 19.5 (total)	Based on Pan <i>et al</i> 2006
LD-HCT + Ext ULD CINE-CT	HCT axial coverage: 500 mm (400 mm coverage from cine-CT)	1.35 (cine-CT) + 1.33 (HCT) = 2.7 (all CT) ^b + 3.6 (PET) = 6.3 (total)	Proposed in this paper

Abbreviations: Dx CT = Diagnostic CT, HCT = Helical CT. LD-HCT = Low Dose HCT for PET/CT. LD-CINE = Low Dose Cine CT. Ext LD-CT = Extended duration and coverage Low Dose Cine CT. Ext ULD CINE-CT = Extended duration and coverage Ultra-Low Dose Cine CT. C+A+P = CT scan range of chest, abdomen, and pelvis, roughly equivalent to 'whole-body' range used in PET/CT.

a. Effective PET dose calculated based 1.9E-02 mSv/MBq from ICRP report 106, 2008 (Table C.9.4).

b. Effective CT dose calculated with ImpACT CT Dosimetry tool (v 1.0.4).

4.1.2 Constraints on CT system for CT radiation dose reduction

Previous discussions already show that it is important and necessary to reduce radiation dose dramatically from CT scans for PET attenuation correction in quantitative PET/CT imaging. In theory, many methods could be used to reduce CT radiation dose for PET/CT imaging. However, in practice, clinical feasibility is a critical constraint in the selection of methods. The methods used need to be implementable in clinical systems in a reasonable time frame without excessive re-engineering of hardware or compromising clinical feasibility. Thus, the methods developed in this thesis are aimed to be within the constraints that they are feasible with current generation hardware and do not compromise the clinical ability of current PET/CT scanners.

4.1.3 General strategies for CT radiation dose reduction and bias/noise suppression

Under the constraint of using a standard clinical X-ray CT scanner, there are several potential methods for reducing CT radiation dose and for reducing the bias and noise that are characteristic of low dose CT images . Table 4.2 provides several potential methods for reducing dose in CT scans. Table 4.3 lists several potential methods to compensate for the increased noise and artifacts at radiation dose reduced CT images. Potentially the most important of these is the recognition that diagnostic CT images usually have a higher signal to noise ratio than is necessary for CT-based PET attenuation correction (CTAC) and motion estimation. This recognition allows for the use of several simple strategies to enable CT radiation dose reduction while maintaining or improving PET image quality (Colsher *et al.*, 2008). This chapter investigates selected combinations of dose reduced acquisition and

noise suppression methods to enable ultra-low dose CT-based PET attenuation correction, benefiting from the reduced requirement of CT for PET AC. Those methods include reducing CT tube current, optimizing CT tube voltage, adding filtration, CT sinogram smoothing and clipping.

Table 4.2 Potential methods for reducing CT radiation dose for CT-based attenuation correction.

Reduce mAs
Optimize kVp
X-ray tube pulsing
Filtration and/or beam conditioning (Boone <i>et al.</i> , 2001; Crotty <i>et al.</i> , 2007)
Collimation
Short scan

Table 4.3 Potential methods for CT noise and bias suppression

Reduced requirements for PET CTAC (Kinahan <i>et al.</i> , 2006a; Kinahan <i>et al.</i> , 2003)
Sinogram smoothing/denoising (Colsher <i>et al.</i> , 2008; La Riviere <i>et al.</i> , 2006)
Combining detector elements
Iterative reconstruction (De Man <i>et al.</i> , 2001)
Compressed sensing (Chen <i>et al.</i> , 2008)
Image smoothing/denoising
Time averaging

i) *Reduction of tube current*

The easiest and most obvious way to reduce CT radiation dose to the scanned object is by lowering the tube current [mA] at given acquisition time and tube voltage. Tube current is the flow of released electrons from the filament to the anode across the x-ray tube. Decreasing CT tube current

decreases the number of output x-ray photons from the tube. The radiation dose and mAs product (i.e., the product between the X-ray tube current and acquisition time) have a linear dependency for a given acquisition time. Thus, decreasing tube current linearly decreases the radiation dose. In other words, the radiation intensity (dose rate) is controlled by adjustment of tube current.

ii) *Optimization of tube voltage*

The tube voltage supplied between the cathode and anode determines the maximum kinetic energy the accelerated electrons will have, thus the photon energy the generated spectrum will have through bremsstrahlung radiation. By changing the voltage applied to the tube, the hardness of the radiation, i.e. its penetration capacity, could be varied over a wide range. It is known that lower-energy X-ray photons contribute more to the contrast in the final image, and higher-energy X-rays have better penetration ability. The relationship between X-ray energy (thus tube voltage) and the resulting radiation dose is nonlinear. For example, it has been found (Hsieh, 2009) that for one particular filtration and system geometry,

$$\frac{dose (kVp)}{dose (80kVp)} = \left(\frac{x}{80} \right)^{2.47} \quad (4.1)$$

iii) *Spectral shaping by added filtration*

There are two main types of filters for an X-ray CT system, a shaped bowtie filter and flat filter. As mentioned in the background section, the bowtie filter is used to reduce the radiation dose of the rays situated at the border of the fan beam via a gradual attenuation so the signal-to-noise-ratio is

comparable across the entire fan beam. For different examined anatomy, bowtie filters can vary in size and shape. Besides bowtie filters, flat filters may be used to reduce the radiation dose to the patient. Some manufactures install flat primary filters behind the X-ray tube, allowing the absorption of low-energy radiation present in the polychromatic X-ray spectrum. However, currently this kind of flat filter is very limited in use, typically 1-3 mm Al or 0.1 mm Cu, with the overall filtering amounts to approximately 5-6 mm Al-equivalent, due to the requirement of high contrast in diagnostic CT imaging for soft tissue discrimination.

For PET attenuation correction, since the CT image is not used for diagnostic purposes, the demand for contrast in the CT image could be moderated by adding flat filters to strongly remove low-energy photons and shape the spectrum to be more dose-efficient with more components of high-penetrating photons. Thus, spectral shaping with added filtration is unique and useful for ultra-low dose CT attenuation correction for PET. Different combinations of metal materials and thicknesses can be studied for shaping the X-ray spectrum with reduced CT radiation dose for PET attenuation correction.

iv) *Sinogram smoothing and clipping*

The root cause of CT number inaccuracy with extremely low dose CT is the treatment of negative signals before logarithmic operation. To reduce the impact of electronic noise, the most effective approach is to process the signal with a low-pass filter prior to performing the logarithmic operation. The filter is applied to all signals in order to preserve the mean and not introduce

bias. As it is known that low-pass filtering generally reduces spatial resolution, filtering before logarithmic conversion will sacrifice CT resolution. However, for PET attenuation correction, CT resolution is not a concern since in practice, to get the attenuation map, CT has to be purposely smoothed with post-processing techniques to match the PET resolution. The easiest way is to use a boxcar kernel for smoothing (Colsher *et al.*, 2008; Xia *et al.*, 2009).

$$p'(x, y, z) = -\log\left(\frac{1}{C} \sum_{\Delta x=-m}^m \sum_{\Delta y=-n}^n \sum_{\Delta z=-l}^l p(x + \Delta x, y + \Delta y, z + \Delta z)\right) \quad (4.2)$$

With $(m, n, l) \in \mathbb{N}^3$, and $C = (2m+1)(2n+1)(2l+1)$.

Other methods to reduce CT noise and streak artifacts include the use of an adaptive filter, such as adaptive trimmed mean filter (ATM) proposed by Hsieh (Hsieh, 1998). This method uses an adaptive smoothing filter with the parameters adjusted to the local statistical properties of the sinogram data to remove noise as well as preserving the CT spatial resolution.

4.2 Materials and Methods

4.2.1 Simulation tool

The Computer Assisted Tomography SIMulator (CATSIM) was used for the simulation of the X-ray CT imaging (De Man *et al.*, 2007) as discussed in chapter 3. It includes a Monte Carlo based simulation package called CATDOSE for estimation of the CT radiation dose. Both CATSIM and CATDOSE have been validated relative to GE Lightspeed Volumetric Computed Tomography (Lightspeed VCT, General Electric Medical Systems, Waukesha, WI) measurements for a series of properties. The CT simulation

models the effects of the X-ray source focal spot, polychromatic tube spectra, beam conditioning, bowtie filter, beam hardening, detector noise and scatter. Although fully described elsewhere, this section provides a brief summary of the properties modeled by CATSIM.

CT raw data y_i at sinogram index i , are formed from the combination of a quantum noise process p_i and electronic noise process z_i , i.e., $y_i = p_i + z_i$, following methods described by (De Man *et al.*, 2007) similar to the methods described by others (La Riviere, 2005; Whiting *et al.*, 2006). The quantum noise is modeled as:

$$p_i = \left[\sum_k E_k \cdot x_{ik} \right] f_C \quad (4.3)$$

Where E refers to photon energy, k is the energy bin index, f_C is a factor to convert from keV to the number of electrons, and x_{ik} is a Poisson random process with parameter λ_{ik} , $x_{ik} \sim \mathbb{P}(\lambda_{ik})$, where

$$\lambda_{ik} = \eta \cdot A_{ik} \cdot \sum_s \frac{1}{S} \exp\left(-\sum_o l_{iso} \mu_{ok}\right) + y'_{ik} \quad (4.4)$$

where η is the detector quantum efficiency (fraction of photons absorbed), A_{ik} is the number of photons arriving at the detector without attenuation for energy bin k , s is the beam sub-sampling index for the total of S sub-beam samplings, l_{iso} is the intersection length between the line with index i and the object element with index o , μ_{ok} is the linear attenuation coefficient of object at o at energy k , and y'_{ik} is the estimated scatter at sinogram index i with energy index k .

The electronic noise z_i is modeled as a Gaussian random process, $z_i \sim \mathcal{N}(d, \sigma_e^2)$, where d is the dark current, and σ_e , is the standard deviation of the electronic noise.

The PET images were simulated using a simplified version of ASIM (Comtat *et al.*, 1999), which included the physical effects of attenuation, background noise, and photon counting. The noisy prompt coincidences \tilde{p} follow a Poisson pseudo-random process with mean m , ($\tilde{p} \sim \mathbb{P}(m)$), defined as

$$m = \alpha_t \cdot t + \alpha_b \cdot b \quad (4.5)$$

where t represents the true coincidences; b is the background noise including scattered and random coincidences; and α_t and α_b are global scale factors for true coincidences and background noise, respectively.

Both CATSIM and ASIM are projector-based simulation methods, which allow for rapid generation of multiple independent and identically distributed (i.i.d.) realizations of data.

4.2.2 Test objects

Two test phantoms were used in the simulations. The first was a uniform 20 cm × 30 cm elliptical water cylinder, with a 10 cm axial dimension, containing uniform activity with count levels of a typical whole-body FDG PET scan. The second was derived from the NURBS-based cardiac-torso (NCAT) phantom (Segars, 2001; Segars *et al.*, 2008), with focal FDG uptake in a 1.6-cm-diameter bone lesion and a 6-cm-diameter soft tissue lesion. The activity

distribution was set at background: liver: lung: lesion as 1:3:0.7:6. The elliptical phantom allowed for systematic evaluation of each dose-reduction method on PET quantitation for uniform soft tissues. The NCAT phantom was used for a more realistic study of lesion quantitation with selected combinations of acquisition parameters representing clinical settings.

4.2.3 Data flow and parameters

Figure 4.1 shows the simulation data flow, where the CT images generated by CATSIM were used to estimate the linear attenuation coefficients at 511 keV for PET attenuation correction. A modification of the bilinear scaling method was used (Kinahan *et al.*, 2003; Burger *et al.*, 2002a). In this method, two scaling factors (one for water/air mixtures and the other for water/bone mixtures) were used to calculate the attenuation values for PET energy directly from the CT numbers. The scaling factors are optimized for different kVp settings from the CATSIM data since the ground truth was known in these studies.

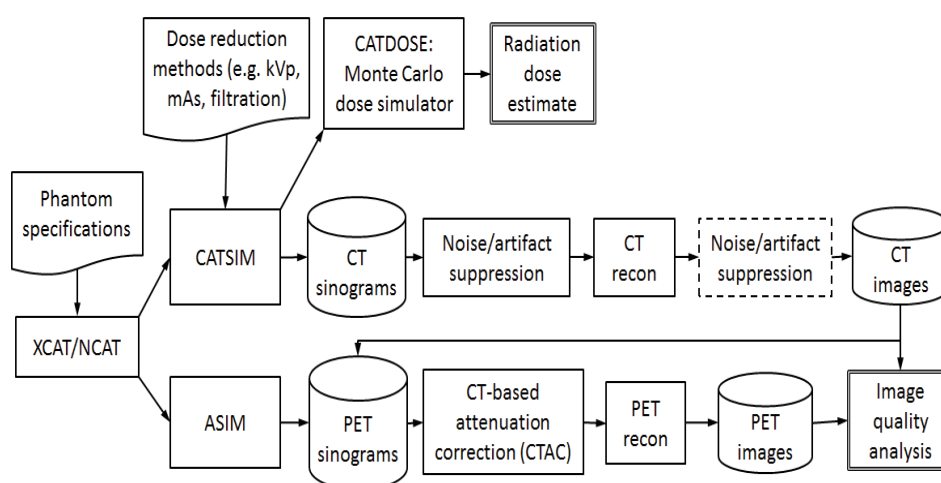


Figure 4.1 Data processing flow used for the simulation studies. The

processing step in the dotted box is not included in this study.

In each simulation, only a single trans-axial section of the phantom was scanned. CT step-and-shoot mode with a gantry rotation time of 0.5 s was used. The beam conditioning included 2 mm of graphite nearest the x-ray source, followed by 0.25 mm of aluminum. Beam hardening correction was applied to the sinogram, based on the polynomial correction method (Hsieh, 2009). The CT slice thickness was 3.125 mm, comparable with the PET slice thickness. All CT images were reconstructed to the size of 128×128 pixels using filtered backprojection (FBP) over a 50 cm field of view (FOV) to match PET image dimensions. Unless otherwise specified, the attenuation corrected PET images were reconstructed using FBP to an image size of 128×128 pixels over 50 cm FOV.

4.2.3.1 CT radiation dose reduction through acquisition parameters and spectral shaping.

CT electronic noise, z_i , was added to the Poisson distributed projection data. For the elliptical water phantom, the variance of z_i was set to different levels {64, 160, 400 photons} of quantum noise to reflect previous studies that modelled electronic noise based on the performance of previous generation CT data acquisition systems (La Riviere *et al.*, 2006). For each combination of tube voltage {80, 100, 120, 140} kVp and tube current {0.5, 1, 5, 10, 20, 25, 50, 100, 500} mA, 20 i.i.d. data realizations for a total of 720 simulations were generated at each electronic noise level for the water cylinder phantom.

Spectral shaping was performed by adding Cu ($Z = 29$) filters of varying

thickness. The study modelled x-rays traveling through primary filters of Cu with varying thicknesses, then through a standard bowtie filter. The post-bowtie spectra were evaluated in terms of mean energy and transmission efficiency (TE), which is defined as the sum of photons in the full spectra divided by the sum of photons in the full spectra with no added filter. With a 160 photon equivalent electronic noise level, for each combination of {120, 140} kVp, {0.5, 1, 5, 10, 20, 25, 50, 100, 500} mA, and {0.25, 0.5, 1.0} mm thickness of copper filtration, this study generated 20 i.i.d. data realizations for a total of 1080 simulations for the water cylinder phantom.

4.2.3.2 CT noise and artifact reduction by sinogram smoothing.

The 160 CT sinograms of the water cylinder phantom (simulated with 140 kVp, no copper filtration, electronic noise of 160 photons) were filtered by 2D 3×3 boxcar smoothing, followed by an adaptive trimmed mean filter (ATM) (Colsher *et al.*, 2008; Hsieh, 2009; Xia *et al.*, 2009).

Next, scans of the NCAT phantom were simulated at CT parameters of 120 kVp, 0.5 mm added copper filtration, with electronic noise on the order of ten photons worth of quantum noise. This noise setting reflects the performance of newer generation CT systems. Several CT tube currents were simulated {1, 5, 10, 20, 50, 100, 500} mA (with one realization for each). Different 2D boxcar smoothing levels ({ 3×3 , 3×5 , 5×5 , 7×7 , 11×11 }) followed by ATM were applied on each of the acquired CT sinograms respectively, making a total of 35 combinations of smoothing level and mA level. The attenuation corrected PET images were reconstructed using both FBP and weighted OSEM (16 subsets, 14 iterations) followed by Gaussian

post-filtering (5 mm FWHM) on 128×128 pixels over a 50 cm FOV.

4.2.4 Metrics

For all the above simulations, CT radiation dose was calculated with CATDOSE, where the mean absorbed dose (mGy) for the central slice of the phantom was evaluated. Then the bias, noise, and root mean square error (RMSE) for the reconstructed CT and PET images were measured. For simulations of the NCAT phantom, five different regions of interest (ROIs) were drawn, as shown in figure 4.2. Table 4.4 lists the ROI specifications. Then the image bias, image roughness noise and RMSE were measured. For the water cylinder simulations with multiple realizations, corresponding ensemble metrics for CT and PET were also calculated with 18 2D ROIs of radius of 2 cm each, drawn on a cross-section of the phantom for each realization.

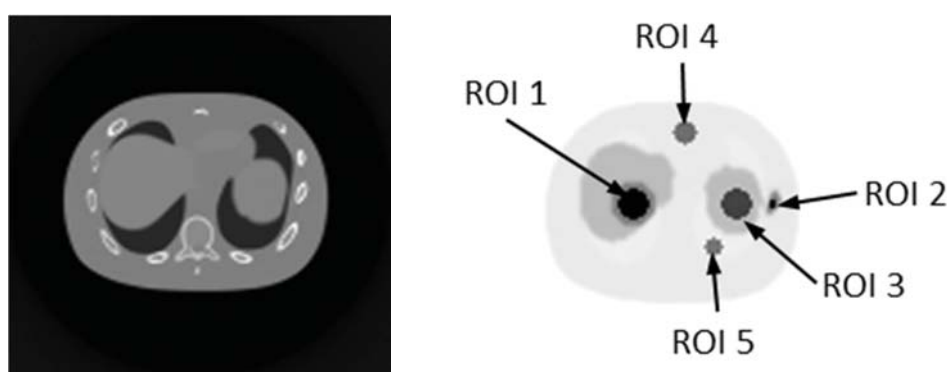


Figure 4.2 (a) Sample images of noise-free CT and (b) corresponding noise-free PET (right) of the NCAT phantom used for simulation with different ROIs drawn on the cross-section image of the NCAT phantom.

Table 4.4 ROI specification

ROI	Radius (cm)	Region
1	2	hot spot in liver
2	0.5	hot spot in bone
3	2	normal spot in spleen
4	1.6	normal spot in background fat tissue
5	1.2	normal spot in lung

4.2.4.1. Bias

For realization r ($r=1, 2, \dots, R$), the mean of pixels in the k th ROI ($k = 1, 2, \dots, K$) is denoted as $m_{r,k}$, \bar{m}_r is the mean pixel value over all ROIs in realization r , and M is the mean of \bar{m}_r over R realizations. Mean bias, B , is calculated as the difference between M and the true value T . Since the true value is constant, we calculate the standard error of the mean M for all realizations SE_M as follows

$$B = M - T ,$$

$$SE_M = \frac{\sqrt{\frac{1}{R-1} \sum_{r=1}^R (\bar{m}_r - M)^2}}{\sqrt{R}} ,$$

where $M = \frac{1}{R} \sum_{r=1}^R \bar{m}_r$, $\bar{m}_r = \frac{1}{K} \sum_{k=1}^K m_{r,k}$, $m_{r,k} = \frac{1}{I} \sum_{i \in ROI_k} f_{ir}$, f_{ir} is the

value of pixel i in realization r and I is the total pixel number in each ROI .

4.2.4.2. Noise

Two types of noise were measured, image roughness noise and ensemble noise (Tong *et al.*, 2010b).

1) Image roughness: For ROI_k and realization r , image roughness $IR_{r,k}$ were measured by calculating the standard deviation of the pixel values inside the ROI. Then the mean image roughness, IR was defined as the mean over r and k of the measured $IR_{r,k}$ and the standard error of mean IR (SE_{IR}) was evaluated as well.

$$IR = \frac{1}{R} \sum_{r=1}^R \left(\frac{1}{K} \sum_{k=1}^K IR_{r,k} \right),$$

$$SE_{IR} = \frac{\sqrt{\frac{1}{R-1} \sum_{r=1}^R \left(\frac{1}{K} \sum_{k=1}^K IR_{r,k} - IR \right)^2}}{\sqrt{R}},$$

where $IR_{r,k} = \sqrt{\frac{1}{I-1} \sum_{i \in ROI_k} (f_{i,r} - m_{r,k})^2}$, f_{ir} is the value of pixel i in realization r and I is the total pixel number in each ROI.

2) Ensemble noise: For each ROI_k , the ensemble noise EN_k was defined as the standard deviation of ROI means $m_{r,k}$ across the R realizations, and this value was averaged over all ROIs to obtain the final mean ensemble noise EN for the uniform background. The standard error of mean ensemble noise SE_{EN} is also calculated.

$$EN = \frac{1}{K} \sum_{k=1}^K EN_k,$$

$$SE_{EN} = \frac{\sqrt{\frac{1}{K-1} \sum_{k=1}^K (EN_k - EN)^2}}{\sqrt{K}},$$

where $EN_k = \sqrt{\frac{1}{R-1} \sum_{r=1}^R (m_{r,k} - \bar{m}_k)^2}$, $\bar{m}_k = \frac{1}{R} \sum_{r=1}^R m_{r,k}$, $m_{r,k} = \frac{1}{I} \sum_{i \in ROI_k} f_{ir}$,

f_{ir} is the value of pixel i in realization r and I is the total pixel number in each ROI.

4.4.4.3 Ensemble root mean square error

For each realization r , $RMSE_r$, was defined by calculating the root mean square error between all the measured and the true pixel values inside the object. The ensemble $RMSE$ was defined as the mean over R realizations of the measured $RMSE_r$ and the standard error of mean $RMSE$ (SE_{RMSE}) was evaluated as well.

$$RMSE = \frac{1}{R} \sum_{r=1}^R RMSE_r,$$

$$SE_{RMSE} = \frac{\sqrt{\frac{1}{R-1} \sum_{r=1}^R (RMSE_r - RMSE)^2}}{\sqrt{R}},$$

where $RMSE_r = \sqrt{\frac{1}{I} \sum_{i \in object} (f_{ir} - f_{it})^2}$, f_{ir} is the value of pixel i in

realization r , f_{it} is the truth value of pixel i , and I is the number of total pixel in the object.

4.3 Results

4.3.1 The impact of acquisition parameters and spectral shaping on CT radiation dose reduction

Figure 4.3 shows the normalized spectra of the simulations for the 80 kVp without added filtration, 140 kVp without added filtration and 140 kVp with 1 mm Cu beam filtration. It also shows the mean energy and relative photon flux transmission efficiency for each spectrum. Table 4.5 lists the mean

energy and transmission efficiency of the spectra for all kVp settings with added Cu filtration of various thicknesses. As expected, increased filtration thickness increases the mean energy and reduces transmission efficiency.

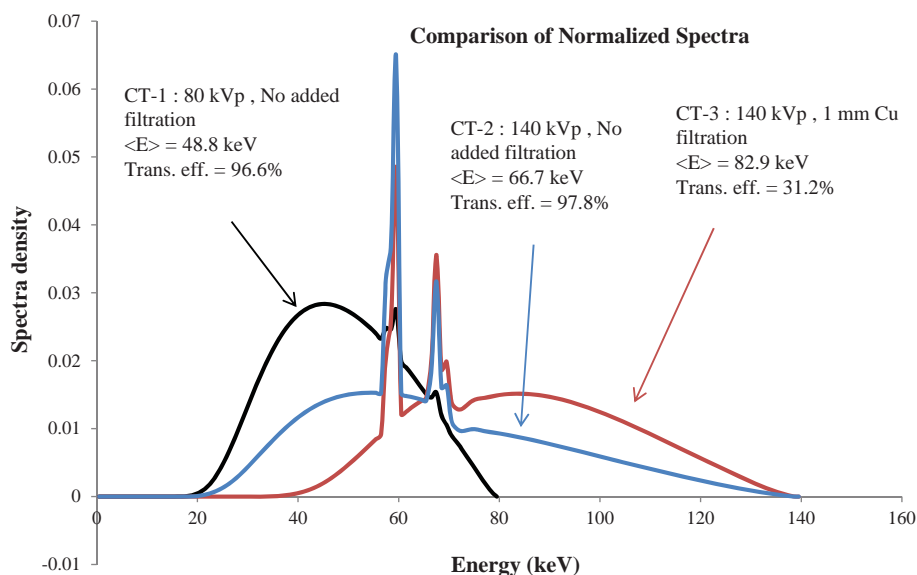


Figure 4.3 Spectra for three CT acquisitions with mean energy and relative photon flux transmission efficiency.

Table 4.5 Mean energy and transmission efficiency comparison corresponding to the normalized spectra density with different filtration thickness at various kVp settings.

Cu (mm)	Property	80 kVp	100 kVp	120 kVp	140 kVp
0	Mean Energy (keV)	48.8	56.0	61.9	66.7
	Transmission Efficiency (%)	96.6	97.2	97.6	97.8
0.25	Mean Energy (keV)	54.1	61.7	67.9	72.9

	Transmission Efficiency (%)	48.5	57.9	63.7	67.3
0.5	Mean Energy (keV)	57.2	65.1	71.6	77.0
	Transmission Efficiency (%)	28.5	38.8	45.6	50.0
1	Mean Energy (keV)	60.8	69.4	76.8	82.9
	Transmission Efficiency (%)	12.2	20.4	26.7	31.2

Figures 4.4-4.5 show the image roughness noise and bias in the reconstructed CT and corresponding PET images as a function of radiation dose for the elliptical water phantom at different combinations of kVp, mA and filtration settings. The standard error of the mean for those metrics across 20 i.i.d. simulations is illustrated with an error bar for the 80 kVp no added filtration setting; errors bars are not presented on the other curves to reduce clutter and because the error is extremely low (as shown with 80 kVp). The image ensemble noise and RMSE plots for CT and PET (data not shown) display similar trends. For the PET data plots, the lower range is truncated if PET bias exceeds 5% when mA decreases from 500 mA to 10 mA in the selected settings. For comparison, Table 4.6 lists corresponding CT bias, CT image roughness noise, CT ensemble noise, PET image roughness noise, PET ensemble noise as well as mean absorbed doses at 5% PET bias for each of the selected filtration settings. The values in the table are calculated through linear interpolation of simulated results in the selected ranges.

Anecdotal CT images generated with different spectra resulting in matched absorbed dose and the corresponding AC PET images are shown in

Figure 4.6. As expected, the higher energy spectra (140 kVp, 1 mm Cu) results in a CT image with visually less streak artefacts and noise.

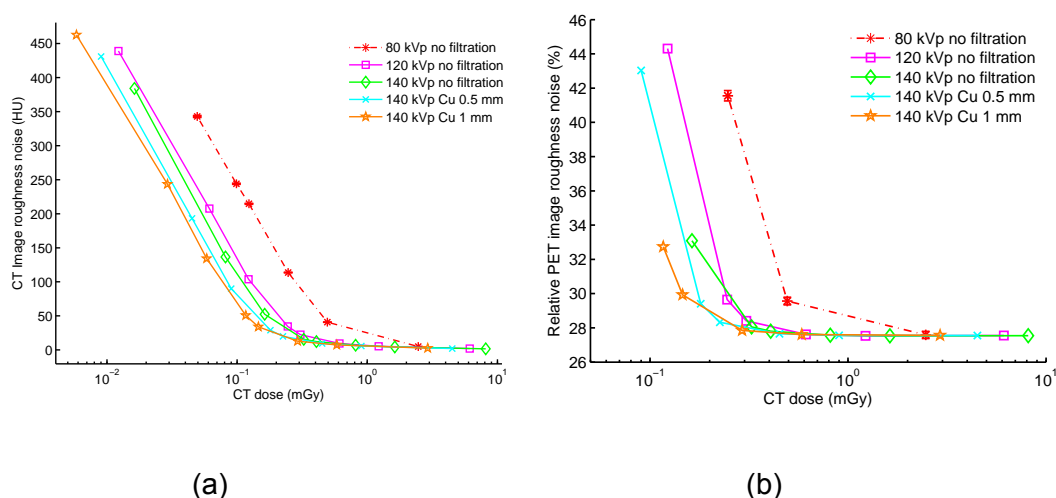


Figure 4.4 (a) CT image roughness noise vs. CT absorbed radiation dose. **(b)** PET image roughness noise vs. CT absorbed radiation dose. Results are based on 20 each repeated CT and PET i.i.d. simulations using various filtration, kVp, and mAs parameters for a 20 x 30 cm elliptical water-filled phantom. The CT tube current is varied for each kVp from 500 mA down to 0.5 mA leading to different absorbed doses (0.5 s tube rotation time). The CT dose is measured as the mean absorbed dose across the central part of the phantom with slice thickness of 3.125 mm. As illustration, the standard error of the mean is shown as error bar for the 80 kVp no filtration case, but is too small to be observed. For CT, the lower range is truncated if the bias is greater than 700 HU with visually obvious artifacts. For PET, the lower range is truncated if the corresponding bias is more than 20%.

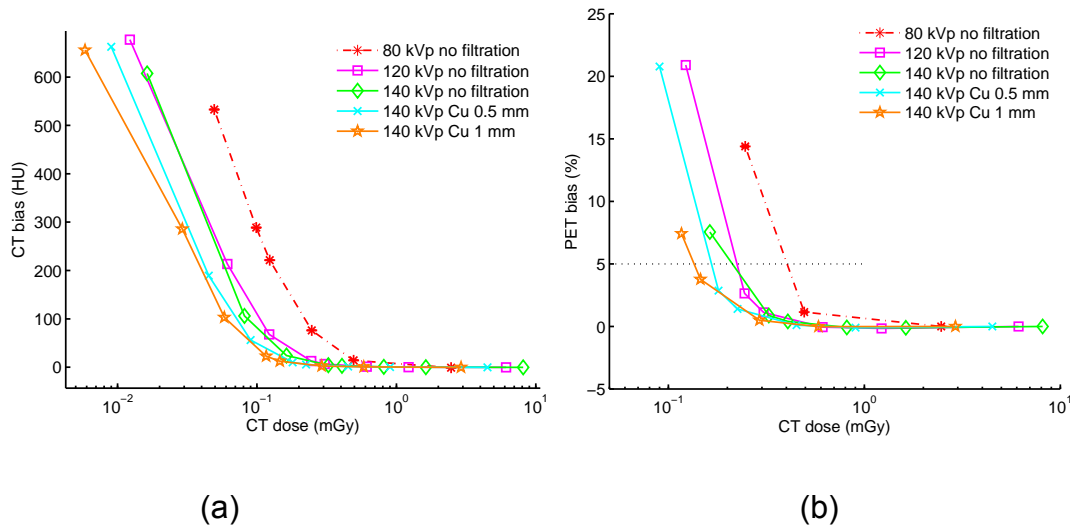


Figure 4.5 (a) CT image bias vs. CT absorbed radiation dose. **(b)** PET image bias vs. CT absorbed radiation dose. Results are based on 20 each repeated CT and PET i.i.d. simulations using various filtration, kVp, and mAs parameters for a 20 x 30 cm elliptical water-filled phantom. The CT tube current is varied for each kVp from 500 mA down to 0.5 mA leading to different absorbed doses (0.5 s tube rotation time). The CT dose is measured as the mean absorbed dose across the central part of the phantom with slice thickness of 3.125 mm. The standard error of the mean is shown as error bar for the 80 kVp no filtration case and is very small. For CT, the lower range is truncated if bias is greater than 700 HU with visually obvious artifacts. PET mean bias of 5% is shown as the horizontal black line.

Table 4.6 At 5% PET bias, corresponding CT bias, CT image roughness noise, PET image roughness, and mean absorbed dose.

Method	CT dose (mGy)	bias in CT (HU)	Roughness noise in CT (HU)	Ensemble noise in CT (HU)	Roughness noise in PET (%)	Ensemble noise in PET (%)
80 kVp, no filtration	0.42	32.37	61.97	3.10	33.05	2.35
120 kVp, no filtration	0.23	19.90	43.44	2.22	31.54	2.24
140 kVp, no filtration	0.22	16.53	38.39	2.00	31.17	2.21
140 kVp, 0.5 mm Cu	0.17	15.61	36.28	1.85	31.03	2.19
140 kVp, 1 mm Cu	0.14	16.09	39.59	2.04	30.88	2.20

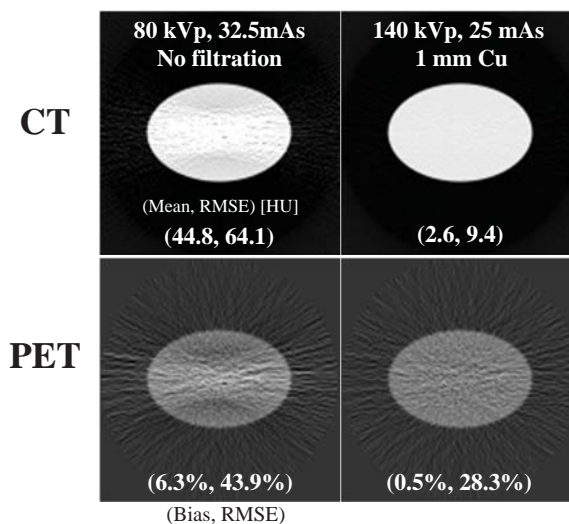


Figure 4.6 (top) CT image mean and RMSE of the water cylinder phantom and (bottom) corresponding attenuation corrected PET mean and RMSE at the same CT radiation dose.

4.3.2 The impact of CT sinogram smoothing

A representative example of the influence of simple boxcar smoothing and ATM filtering on the simulated CT sinogram data after dark current correction is shown in Figure 4.7. A 5×5 boxcar followed by ATM smoothing was applied on one projection view of a CT sinogram acquired at 1 mA, 120 kVp, 0.5 mm Cu filtration. The fraction of non-positive sinogram values decreased from 17.05% to 3.29% after boxcar smoothing, and was further reduced to 0.05% after ATM smoothing and sinogram clipping. This shows that sinogram smoothing may be effective at reducing or eliminating noise induced artifacts in CT.

Figure 4.8 shows the comparison results of CT bias and corresponding PET bias as a function of CT tube current for the elliptical water cylinder phantom (simulated with 140 kVp, no copper filtration, electronic noise of 160 photons). Different levels of sinogram smoothing were used: no sinogram smoothing, 2D 3×3 boxcar smoothing and 2D 3×3 boxcar + ATM smoothing, respectively. It can be observed that for a matched PET bias of 5%, compared with no CT sinogram smoothing, 2D 3×3 boxcar smoothing allows reducing the tube current from ~ 13 mA to ~ 4 mA, while 2D boxcar smoothing + ATM allows a further reduction in tube current.

The impact of CT sinogram smoothing in noise-free NCAT PET images is shown in Figure 4.9 presenting the profiles through the PET lung region with different CT sinogram smoothing levels. CT sinogram smoothing can cause resolution mismatch between CT and PET images, especially at boundaries.

Tables 4.7 and 4.9 present the reconstructed CT and corresponding noisy PET images for the NCAT phantom. Each column of a table represents a different CT dose level (with (tube current) \times (time) in units of mAs), and each row represents a different sinogram smoothing level (boxcar kernel size). The numerical value listed on the corner of each image in table 4.7 gives the RMSE of the reconstructed CT image. The number on the corner of each image in table 4.9 shows the normalized RMSE for PET (% of RMSE compared to the known true PET image). Results for other mA levels are not shown here but are consistent with the patterns shown in Tables 4.7 and 4.9. The difference images of CT and noisy PET are also compared in Table 4.8 and Table 4.10. Table 4.11 lists percentage change of bias, coefficient of variation of image roughness for different ROIs and normalized RMSE for the total object in the noisy PET images if the corresponding CT images are acquired at 120 kVp, 0.5 mm Cu filtration, 2.5 mAs, with various sinogram smoothing levels. This shows that compared to no sinogram smoothing, some level of smoothing is helpful for reducing PET bias and noise, while too much smoothing may be detrimental for PET quantitation.

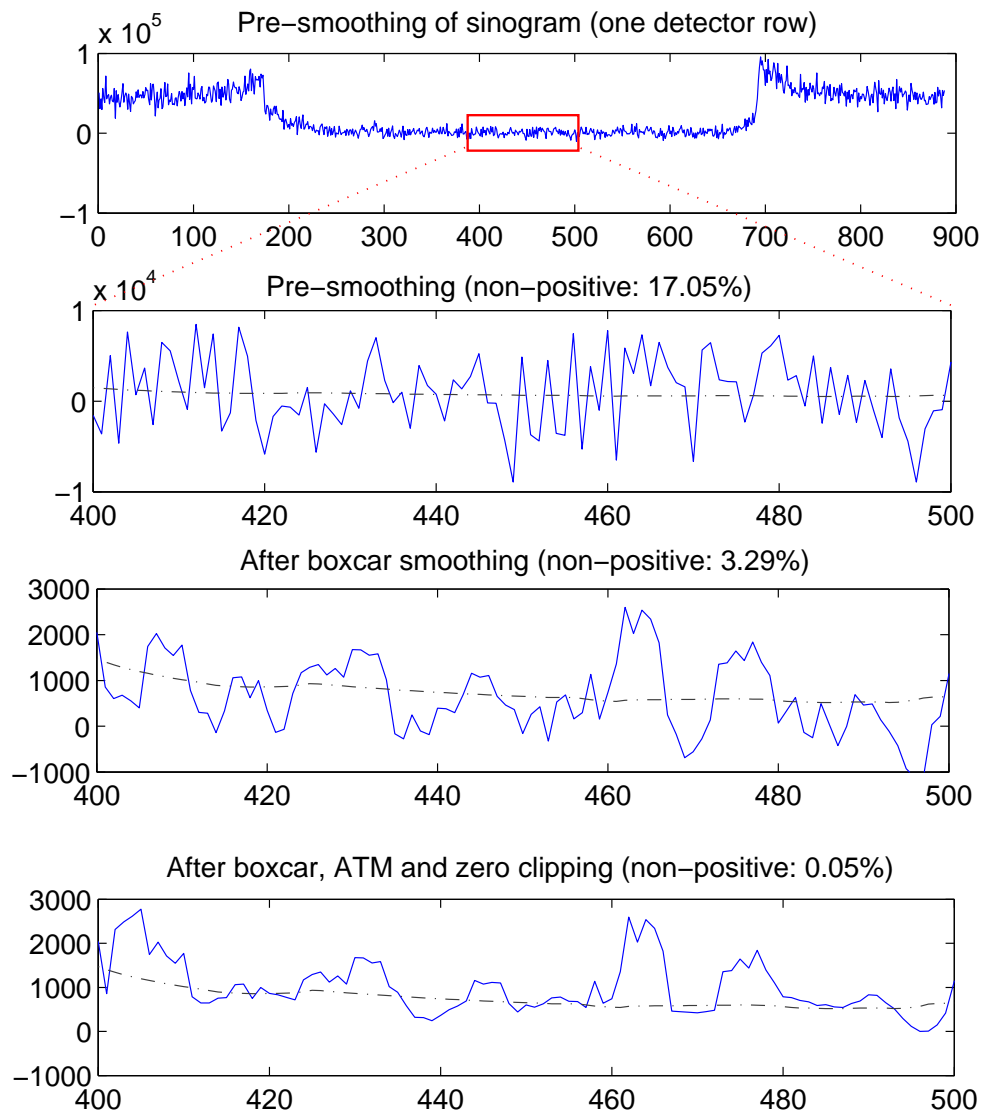


Figure 4.7 Detailed profile of sinogram after dark current subtraction in each processing step. The sinogram was generated with CT technique of 1 mA, 120 kVp, 0.5 mm Cu filtration. The sinogram was smoothed by a 5×5 boxcar, followed by ATM smoothing and zero clipping. Note the x- and y- axis scale changes. The dashed line is the reference noise-free CT sinogram profile for comparison.

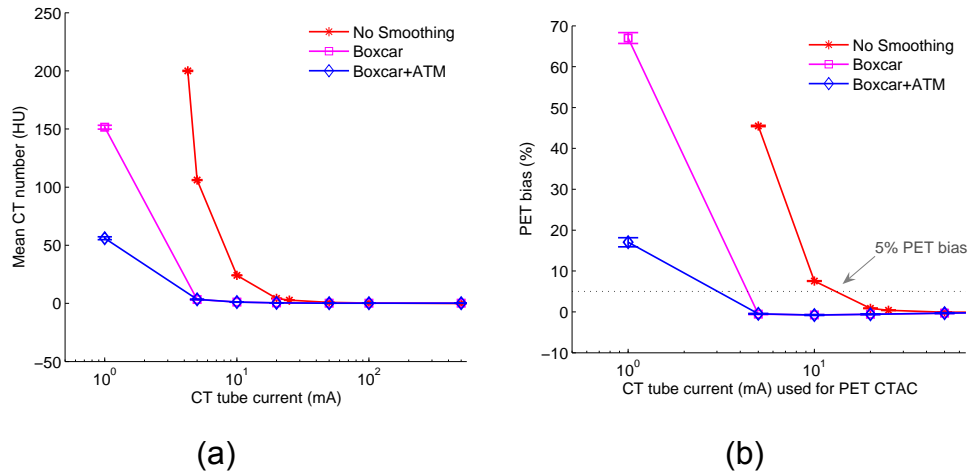


Figure 4.8 (a) Comparison of CT bias (mean CT number in HU) as a function of CT tube current with and without sinogram smoothing for 20 i.i.d elliptical water cylinder phantom simulations. (b) Corresponding comparison of PET bias (%) as a function of CT tube current for the 20 i.i.d elliptical water cylinder phantom simulations with and without CT sinogram smoothing. The standard error of the mean is shown as error bar. The dotted line shows 5% PET bias. It can be seen that 2D 3×3 boxcar sinogram smoothing could reduce CT dose for matched PET bias, boxcar followed with ATM could further reduce CT dose. Note that lower range of the no smoothing case is truncated if the corresponding PET bias is higher than 70%.

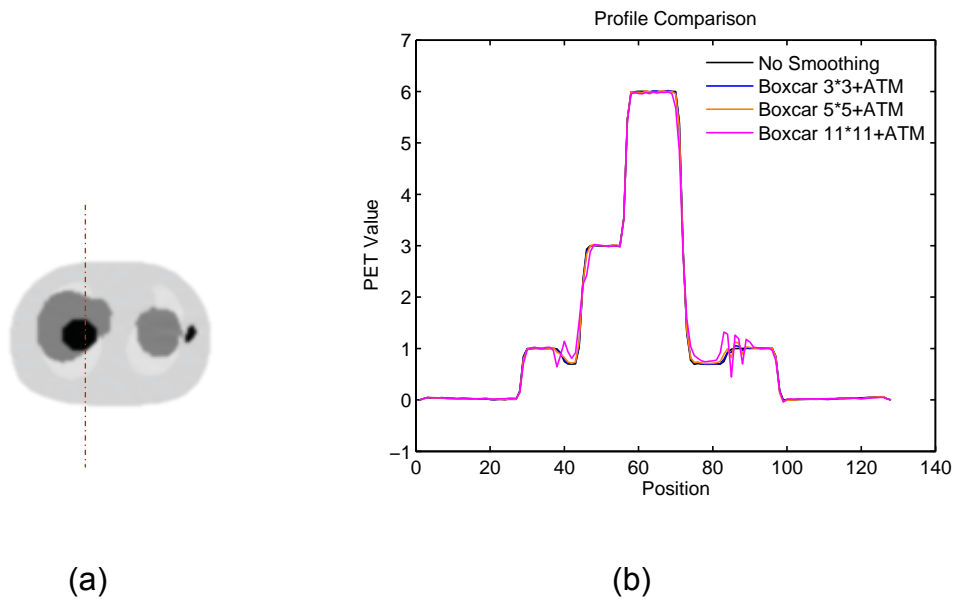


Figure 4.9 (a) Illustration of the location of the profile through the reconstructed noise-free PET NCAT phantom. (b) The profile through PET lung region as illustrated in the left for different CT sinogram smoothing kernels.

Table 4.7 The effects of different smoothing levels on the CT images of the NCAT phantom. The number in each table element is the root mean square error (RMSE) measured in HU. The underlined value represents the optimal smoothing level at each dose level (tube current time product in unit of mAs in the column). The CT images were simulated at 120 kVp, 0.5 mm Cu filtration.

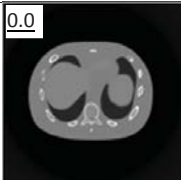
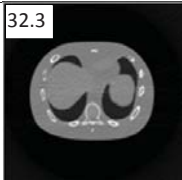

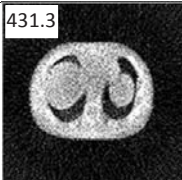
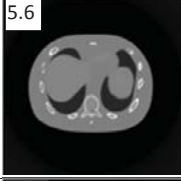
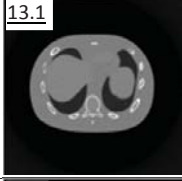
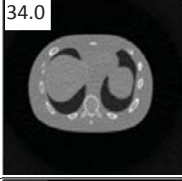
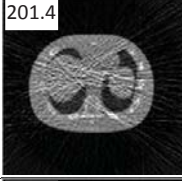
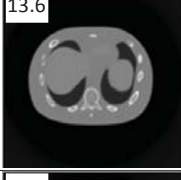
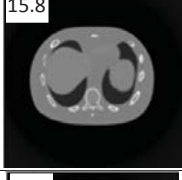
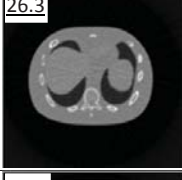
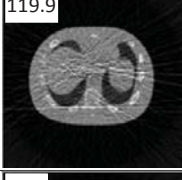
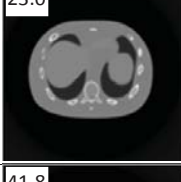
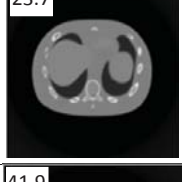
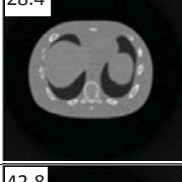
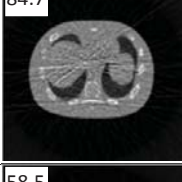




CT total tube current Sinogram smoothing levels	CT noise-free	10 mAs	2.5 mAs	0.5 mAs
No CT sinogram smoothing	<u>0.0</u> 	32.3 	182.6 	431.3 
3*3 Boxcar +ATM	5.6 	<u>13.1</u> 	34.0 	201.4 
5*5 Boxcar +ATM	13.6 	15.8 	<u>26.3</u> 	119.9 
7*7 Boxcar +ATM	23.0 	23.7 	28.4 	84.7 
11*11 Boxcar +ATM	41.8 	41.9 	42.8 	<u>58.5</u> 

Table 4.8 The difference images of the NCAT phantom simulated above with the noise-free no sinogram smoothing CT images. The CT images were simulated at 120 kVp, 0.5 mm Cu filtration.

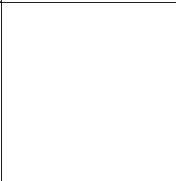
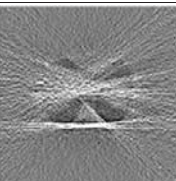
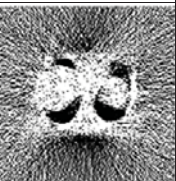
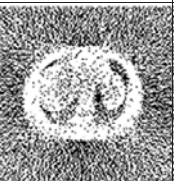

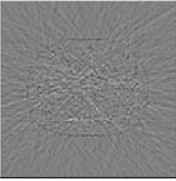
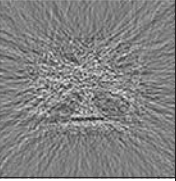
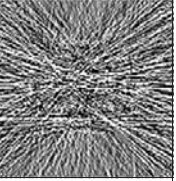

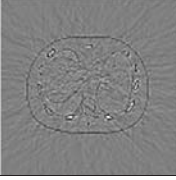
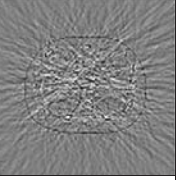
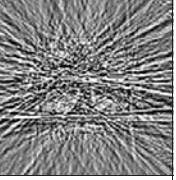


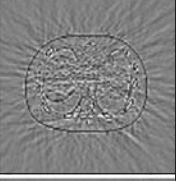
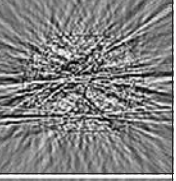



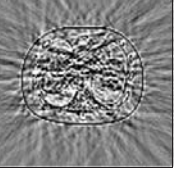
CT total tube current Sinogram smoothing levels	CT noise-free	10 mAs	2.5 mAs	0.5 mAs
No CT sinogram smoothing				
3*3 Boxcar +ATM				
5*5 Boxcar +ATM				
7*7 Boxcar +ATM				
11*11 Boxcar +ATM				

Table 4.9 Noisy PET reconstructed images and the Normalized RMSE (%) are shown for each category. The underlined value highlights the optimal smoothing level at each dose level (tube current time product in unit of mAs in the column). The CT images for PET attenuation correction were simulated at 120 kVp, 0.5 mm Cu filtration.

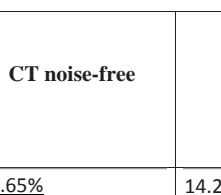
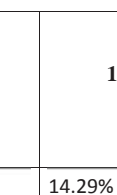
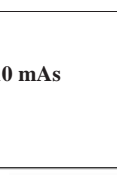
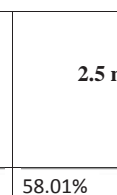
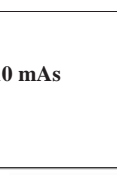
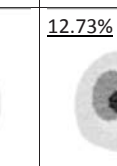

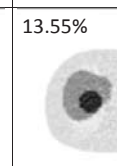
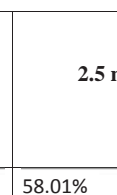
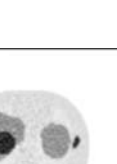
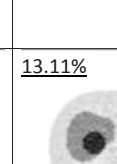
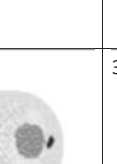
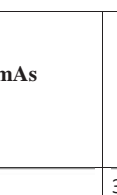

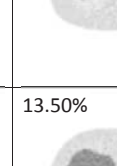
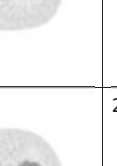
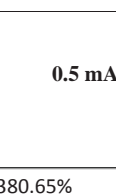
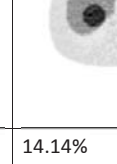
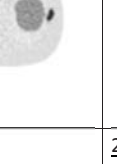

CT total tube current CT sinogram smoothing levels	CT noise-free	10 mAs	2.5 mAs	0.5 mAs
No CT sinogram smoothing	<u>12.65%</u> 	14.29% 	58.01% 	380.65% 
3*3 Boxcar +ATM	12.67% 	<u>12.73%</u> 	13.55% 	37.16% 
5*5 Boxcar +ATM	12.73% 	12.84% 	<u>13.11%</u> 	32.04% 
7*7 Boxcar +ATM	12.91% 	12.97% 	13.50% 	26.42% 
11*11 Boxcar +ATM	13.84% 	13.88% 	14.14% 	<u>21.13%</u> 

Table 4.10 The difference image between noisy PET reconstructed images above and the noise-free truth PET image attenuation corrected with CT noise-free and no sinogram smoothing. The CT images for PET attenuation correction were simulated at 120 kVp, 0.5 mm Cu filtration.

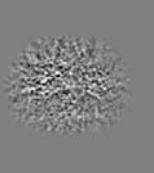
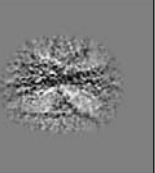


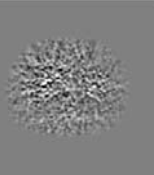
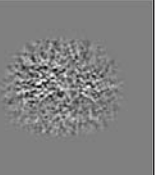
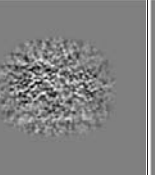
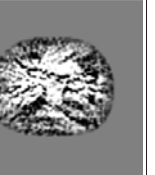
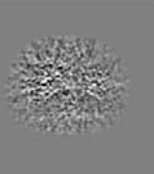
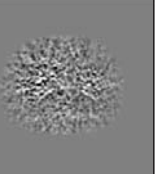
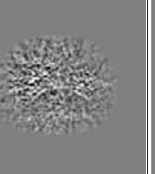

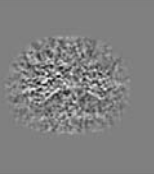
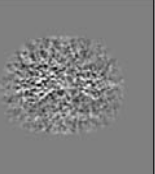
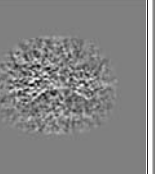


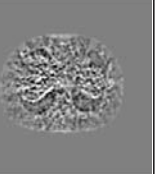
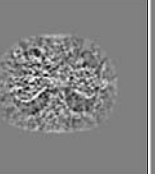

CT total tube current Sinogram smoothing levels	CT noise-free	10 mAs	2.5 mAs	0.5 mAs
No CT sinogram smoothing				
3*3 Boxcar +ATM				
5*5 Boxcar +ATM				
7*7 Boxcar +ATM				
11*11 Boxcar +ATM				

Table 4.11 Bias and noise results for increasing CT sinogram smoothing levels for the NCAT object simulated with a 2.5 mAs CT acquisition. Metrics presented are the percentage PET bias, the percentage image roughness in the brackets for each ROI shown in Figure 2, and the normalized RMSE for the total object. Each metric is normalized to the mean true value of the emission object.

Metrics	ROI	No Smoothing	2D 3*3 boxcar ATM	2D 5*5 boxcar ATM	2D 7*7 boxcar ATM	2D 11*11 Boxcar ATM
PET bias (noise)	ROI #1	24.5 (12.3)	0.5 (8.8)	-0.5 (8.0)	-0.1 (10.0)	-0.5 (9.0)
	ROI #2	30.5 (6.7)	-0.1 (6.3)	0.6 (6.5)	-1.3 (7.0)	-1.4 (8.5)
	ROI #3	41.8 (15.0)	2.8 (10.8)	2.0 (11.5)	0.3 (11.3)	0.9 (10.9)
	ROI #4	68.2 (22.3)	-0.1 (16.8)	2.7 (15.3)	0.2 (14.5)	1.8 (16.1)
	ROI #5	-99.6 (213.3)	-6.0 (19.4)	-0.9 (15.0)	2.2 (16.2)	11.4 (17.2)
RMSE % (total object)		58.0	13.6	13.1	13.5	14.1

4.4 Discussion

The proposed radiation dose reduced acquisition methods are based on CT tube current reduction, tube voltage optimization and spectral shaping. Decreasing CT tube current decreases the number of X-ray photons generated from the tube, thus linearly decreasing the radiation dose for a given acquisition time. By optimizing the tube voltage and the hardness of the x-ray spectra, the photon penetration capacity can be optimized. Additional flat filters could remove low-energy photons and shape the spectrum to be more dose-efficient. The results show that ultra-low dose CT for PET/CT may

be possible by simply extending these standard acquisition methods.

The propagation of noise and bias from the CTAC image to the PET image is complex and depends on the PET image values and the reconstruction algorithm used (Hsiao and Gindi, 2002; Qi and Huesman, 2005). As a rough estimate, however, we have previously shown (Kinahan *et al.*, 2006a) that PET image errors are roughly proportional to local CTAC errors. It can be observed from Figures 4.4 and 4.5 that both bias and noise in the CT image determine the quantitative accuracy in the PET image. As expected, for set kVp and filtration, through tube current reduction, there is a dose threshold below which the CT bias and noise increase significantly. These artifacts are due to photon starvation at low flux levels and the presence of electronic noise in the data acquisition systems (DAS). Modern high-end CT scanners have lower electronic DAS noise than simulated here. Our results clearly show the benefit of reductions in dark current noise for ultra-low dose PET/CT imaging.

Narrower and higher energy spectra are more dose-efficient when subtle contrast discrimination in the CT image is not necessary and over-all PET image bias and noise are important. It can be observed in Figure 4.5(b) that for the lowest energy spectra (80 kVp, no filtration), PET bias is below 5% when absorbed radiation dose is greater than 0.42 mGy. However, for the highest/narrowest energy spectra (140 kVp, 1 mm Cu), PET bias is still below 5% when dose is less than 0.14 mGy. Table 4.6 further illustrates this trend. In Table 4.6, compared to 80 kVp no filtration, optimizing tube voltage and filtration allows reduced CT radiation dose for the matched PET bias. It shows

that for matched PET bias, highest/narrowest energy spectra (140 kVp, 1 mm Cu) has a dose reduction factor of 3 with decreased CT and PET noise compared to the lowest energy spectra (80 kVp, no filtration). It should also be noted that the transmission efficiency is only 31.2%, implying that the X-ray tube uses about 3× more energy for a given protocol. The transmission efficiency metric is intended as a check that filtration is not placing unrealistic requirements on x-ray tube power capabilities. Figure 4.6 shows that for matched CT radiation dose, with spectral shaping, the CT and corresponding PET images have less image noise and artifacts.

Reducing CT radiation dose by extending standard acquisition techniques leads to increased noise and/or artifacts in CT images, especially for ultra-low dose cases where bias and noise in CT images would inevitably appear. At the limit where acquired low dose CT SNR and/or artifacts are detrimental to PET image quality, sinogram smoothing can be employed, making low dose CT acquisitions acceptable for PET attenuation correction. In the presence of electronic noise in the CT DAS, the collected signal after removing the mean dark current of the DAS often drops below zero (Colsher *et al.*, 2008; Kachelriess *et al.*, 2001; Hsieh, 2009). The root cause of the CT number inaccuracy is the treatment of non-positive signals before logarithmic operation. As an example, Figure 4.7 shows the effect of smoothing on the sinogram data in each step. The noise-free profile is also shown in Figure 4.7 as dashed line for comparison. For the simulated NCAT object at set acquisition conditions, it is observed in Figure 4.7 that 2D boxcar smoothing could suppress noise and preserve the mean without introducing bias, followed

by ATM to reduce non-positive values. Filtering before logarithmic conversion with the low-pass 2D boxcar will degrade CT resolution. However, for PET attenuation correction, CT image has to be smoothed with post-processing techniques to match the PET resolution. Our study in Figure 4.8 shows that for a uniform phantom scanned at 140 kVp, and with a threshold of 5% PET bias, the 2D 3×3 boxcar smoothing allows reducing CT dose by a factor of approximately 3 to 4, and 2D 3×3 boxcar smoothing followed with ATM allows a further reduction of CT dose.

The NCAT phantom was simulated to test the effects on lesion contrast. From Tables 4.7 and 4.9, we observe that with reduced mAs (thus reduced radiation dose), both CT and corresponding PET images suffer from increased noise and artifacts if no CT sinogram smoothing is applied. However, with smoothing, we obtain PET images with matched RMSE with reduced radiation dose. For example, by applying 5×5 boxcar followed with ATM, we have PET images of same level of RMSE after reducing CT tube current-time product from 10 mAs to 2.5 mAs (a factor of 4). Table 4.7 and Table 4.9 also suggest the optimal smoothing level (value with underline) for each dose level (each column). In general, more smoothing is needed when noise level is increased. Table 4.11 also gives the percentage of bias, coefficient of variation of image roughness in each ROI and the normalized RMSE for the total object, which indicates that there may be an optimal level of smoothing in reducing PET bias. It is worth noting that these results will vary with the specific PET reconstruction algorithms, reconstruction parameters, post-filtering levels as well as ROI size. However, the results

here indicate the general trend. We also evaluated the PET images reconstructed with FBP, which gave similar results to OSEM PET reconstructions (data not shown). Table 4.8, Table 4.10 and Figure 4.9 suggest that too much CT sinogram smoothing may introduce artifacts in PET images where the object has structural boundaries due to resolution mismatch between CT and PET images.

Though more sophisticated CT sinogram smoothing algorithms could be used, the purpose of this study is to investigate the feasibility of ultra-low dose PET/CT imaging by extending standard methods. The initial results with simple boxcar smoothing followed with ATM (Colsher *et al.*, 2008) are successful and suggest that further improvements may be possible with more sophisticated smoothing algorithms.

Four different CT and PET image metrics were used: image bias, image roughness noise, ensemble noise, and RMSE for image evaluation. Image bias is not typically used for diagnostic CT imaging, but is a reasonable metric used here for CT-based attenuation correction. Image roughness noise measures the pixel to pixel variability in the image, and is the noise perceived when viewing an individual image. Ensemble noise is a measure for noise across independent realizations, and is inversely proportional to detection task performance (Tong *et al.*, 2010b). Evaluation results based on these metrics in our study show that PET noise is not substantially increased by ultra-low dose CT scans with the constraint that bias in the PET image is within an acceptable range. Both bias and noise in the CT images determine the quantitative accuracy in the PET images. We use the absorbed CT dose

in our study as dose metric. The most appropriate quantity for assessing the risk due to diagnostic imaging procedure is the radiation dose to individual organs (Turner *et al.*, 2011). In our study, however, the absorbed dose is used to estimate the relative dose reduction factor compared to those in clinical PET/CT procedures.

One critical constraint for this ultra-low dose CTAC study is that proposed methods should be feasibly implemented on the diagnostic CT subsystem of a PET/CT scanner. For the purpose of PET attenuation correction at 511 keV, CT images can contain relatively high noise, low spatial resolution, and low contrast. This work explored some of the simplest strategies for dose reduction to take advantage of the reduced requirements of CTAC for PET. There are other simple methods besides those studied here, for example: collimation, X-ray tube pulsing, short scan with gating or fixed shielding (Xia *et al.*, 2009; Xia *et al.*, 2010a). For noise reduction, we may use combined detector elements, iterative CT reconstruction (De Man *et al.*, 2001), compressed sensing (Chen *et al.*, 2008), or temporal averaging. We reconstructed CT images on a matrix size that matches PET image size directly in our study. This also reduces CT computation time and may allow for computationally intense CT processing techniques, such as gated and/or iterative CT image reconstruction. To the best of our knowledge, little work has been done to capitalize on the lower image quality requirements of CTAC to combine methods for PET attenuation correction and radiation-dose-reduced CT imaging.

One challenge in this study is that system parameters and

implemented algorithms may vary among different scanners from different manufactures. The presented results here are based on simulations, using combinations of wide range of parameters to predict the general scanner behaviours for ultra-low dose situations. One limitation of the study is that a fixed small scatter-to-primary ratio was used for all our simulations. It is believed, however, that this is a reasonable approximation as it is known that for example, the scatter-to-primary ratio for the LightSpeedTM 16 scanner is less than 4% (Hsieh, 2009). Though scatter causes CT bias, this is a small contribution compared to photon starvation effects in the ultra-low dose case. In addition, some of the simulated parameter values (e.g. tube current less than 10 mA) are below the lower limit currently available on commercial scanners. Furthermore, it may be challenging to equip some CT scanners with special filtration for low dose CT. In general, however, the proposed methods are feasible to implement in practice, and could be translated into protocols for the assessment of individual response to therapy and to strengthen clinical trials of more effective cancer therapies, as well as PET/CT guided radiation treatment planning and PET/CT cardiac imaging.

4.5 Conclusion

This chapter has presented a systematic simulation study investigating the possibility of using ultra-low dose CT for PET/CT attenuation correction. Our simulations are based on PET data that have been attenuation corrected with dose-reduced CT techniques with an elliptical water cylinder phantom containing clinical PET activity and the NCAT phantom with focal FDG uptake in soft tissue and bone. The simulation results demonstrate that ultra-low dose

CT for PET/CT is feasible, and there is significant room to reduce CT radiation dose in the cases where CT is not used for diagnostic or anatomical localization purposes. We have shown that appropriately choosing tube potential, current and filtration allow lower CT doses at matched PET image quality. Spectra that are higher energy and narrower are generally more dose efficient with respect to PET image quality. Sinogram smoothing can be used to compensate for the increased noise and artifacts in reduced dose CT acquisitions. The methods presented here are clinically and technically feasible, and could be used for longer duration CT scans for respiratory-gated CT that is phase matched with PET for attenuation correction and motion estimation, and to reduce patient radiation dose in general.

Chapter V: Dual energy CT used for PET attenuation correction

As mentioned in Chapter I, another challenge for PET/CT quantitation is to estimate tracer uptake in dense and/or high Z materials. Dual energy CT (DECT) takes advantage of the energy dependency of attenuation for different materials, and offers the potential to model the attenuation coefficient of any material as a weighted sum of photoelectric absorption and Compton scattering probabilities. The information extracted from dual energy CT is useful for quantitative imaging of high atomic number materials. Dual energy CT-based attenuation correction could improve the quantitative accuracy of PET/CT imaging involving bone, metal or contrast agent. Improved quantification of tracer uptake could lead to improved patient outcomes by providing more accurate information for therapeutic choices. In this chapter, 1) energy dependent noise and bias properties of monoenergetic images synthesized from dual-energy, or dual-kVp, CT acquisitions are evaluated; 2) associated noise suppression and dose optimization methods are investigated for dual energy CT based PET attenuation correction.

5.1 Introduction

5.1.1 Problems of Interest

Dual energy[†] CT (DECT) has been proposed as a method to estimate material properties using either photoelectric and Compton components (Alvarez and Macovski, 1976), or physical basis materials such as plastic and

[†] It is more accurate to use the term dual-kVp CT, since each CT acquisition is polyenergetic, not monoenergetic. However, the term dual-energy CT is already in wide use.

aluminum (Lehmann *et al.*, 1981). DECT has been proposed to remove the bias from the CT attenuation correction for SPECT (Blankespoor *et al.*, 1996; Guy *et al.*, 1998) and PET (Kinahan *et al.*, 2003). A challenge with the use of DECT is the significant noise amplification due to the poorly conditioned inverse problem of estimating the component sinograms (Beyer *et al.*, 2000a), leading to excessive noise amplification. It has already been shown in the literature that the noise amplification is energy dependent in the diagnostic CT energy range (Alvarez and Seppi, 1979; Alvarez and Macovski, 1976; Doost-Hoseini, 1984), but the noise and bias at SPECT or PET energies are largely unknown. Table 5.1 lists the photon energies of common isotopes used in PET/CT and SPECT/CT Imaging. Figure 5.1 illustrates the noise amplification trend with respect to synthesized energy for known diagnostic CT energy. Another potential drawback of dual energy is the additional patient radiation dose required to acquire two separate energies and to reduce noise.

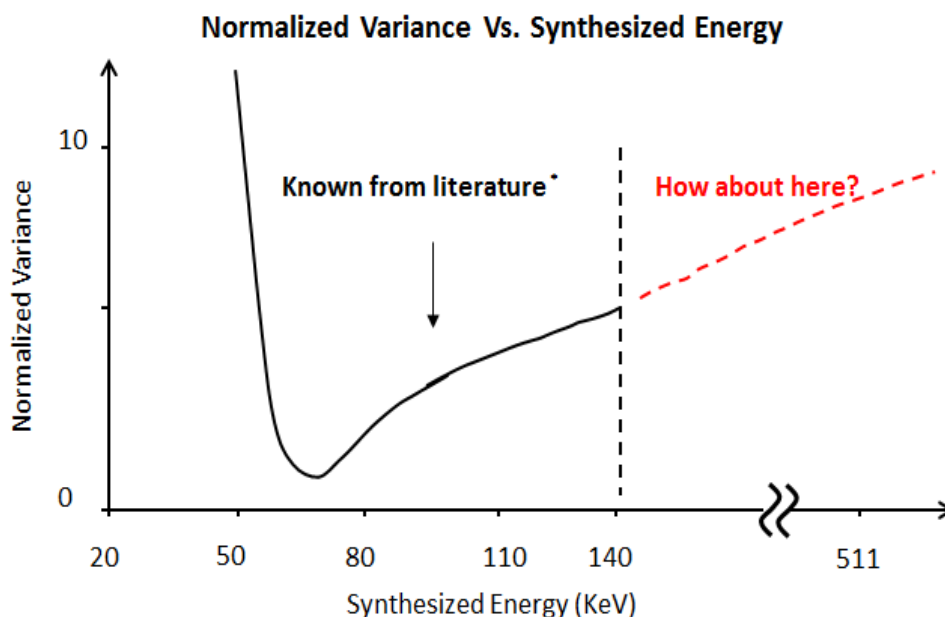


Figure 5.1 Normalized variance vs. synthesized energy from known literature

(Alvarez and Macovski, 1976), but no published literature deals with the noise trend in higher energies.

Table 5.1 Photon energies of common isotopes used in PET/CT and SPECT/CT Imaging.

Mode	Isotope	Energy (keV)
PET	All (i.e. F-18, C-11, N-13, etc.)	511
SPECT	Xe-133	80.9
SPECT	Tc-99m	140
SPECT	I-123	160
SPECT	Ga-67	185
SPECT	In-111	171, 245

To address these issues with DECT-based attenuation correction, there have been alternate methods previously proposed using iterative CT reconstruction (Noh *et al.*, 2009) and image-based strategies (Kinahan *et al.*, 2006a). In this study, the aims are 1) to evaluate the energy dependent noise properties of monoenergetic images synthesized from dual-energy CT, in the energy range appropriate for nuclear imaging (140-511 keV); and 2) to minimize noise and radiation dose in DECT-based attenuation correction.

5.2 Materials and methods

5.2.1 Basis material decomposition (BMD)

The general procedures of the dual energy method are outlined in Figure 5.2. The procedures use the basis material decomposition (BMD) to separate the dual-kVp sinogram data. The details of the BMD method can be found in the papers (Chuang and Huang, 1988; Goh *et al.*, 1997; Lehmann *et*

al., 1981; Gingold and Hasegawa, 1992). We give a brief description of BMD technique.

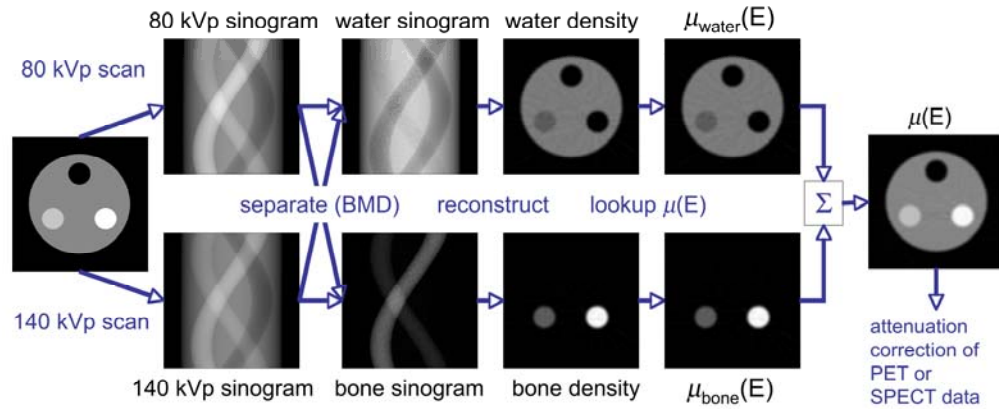


Figure 5.2 Process used to form the monoenergetic attenuation image $\mu(E)$ for attenuation correction of a SPECT or PET radioisotope emitting photons with and energy E .

It is well-known that above the k edge, the linear attenuation coefficient of a particular material ξ , $\mu(x, y, z; E)$, can be considered the composition of two components, attenuation due to the photoelectric absorption and the attenuation due to the Compton scatter, shown in the following formula:

$$\mu(x, y, z; E) = a_p(x, y, z)f_p(E) + a_c(x, y, z)f_{KN}(E) \quad (5.1)$$

where $f_p(E) \approx E^{-3}$ is the photoelectric energy dependency function, and $f_{KN}(E)$ is the Klein-Nishina function describing the Compton scattering part. a_p and a_c are material dependent coefficients that represent the contributions of the photoelectric effect and Compton scatter, respectively .

$$a_c = \frac{\rho}{A} \cdot Z \cdot N_0 \quad (5.2)$$

$$a_p = \frac{\rho}{A} \cdot c_1 \cdot Z^{n'} \quad (5.3)$$

Where ρ is the mass density, A is the atomic weight, Z is atomic number, N_0 is the Avogadro's number, n' is around 4 to 5, and c_1 is a constant.

$$\begin{aligned} \int \mu_\xi ds &= \int [a_p(x, y, z) f_p(E) + a_c(x, y, z) f_{KN}(E)] ds \\ &= \int a_p(x, y, z) ds \cdot f_p(E) + \int a_c(x, y, z) ds \cdot f_{KN}(E) \end{aligned} \quad (5.4)$$

Since any two linearly independent sums of two basis functions (the Compton and photoelectric components) span the space, they're also adequate basis functions. The linear attenuation coefficient of an unknown material ξ , can be expressed in terms of the linear attenuation coefficient of the two "basis" materials α and β .

$$\mu_\xi = C_{\alpha\xi} \mu_\alpha + C_{\beta\xi} \mu_\beta \quad (5.5)$$

According to (5.1),

$$\mu_\xi = a_{p\xi} f_p(E) + a_{c\xi} f_{KN}(E) \quad (5.6)$$

$$\mu_\alpha = a_{p\alpha} f_p(E) + a_{c\alpha} f_{KN}(E) \quad (5.7)$$

$$\mu_\beta = a_{p\beta} f_p(E) + a_{c\beta} f_{KN}(E) \quad (5.8)$$

From (5.5)-(5.8), it can be shown that

$$C_{\alpha\xi} = \frac{\rho_{\xi}}{\rho_{\alpha}} \cdot \frac{N_{g\xi}(Z_{\xi}^n - Z_{\beta}^n)}{N_{g\alpha}(Z_{\alpha}^n - Z_{\beta}^n)} \quad (5.9)$$

$$C_{\beta\xi} = \frac{\rho_{\xi}}{\rho_{\beta}} \cdot \frac{N_{g\xi}(Z_{\xi}^n - Z_{\alpha}^n)}{N_{g\alpha}(Z_{\alpha}^n - Z_{\beta}^n)} \quad (5.10)$$

Where $N_g = \frac{Z}{A} \cdot N_0$ is the electron mass density and n is around 3.8.

Thus, the integral of the linear attenuation coefficient can be written as:

$$\begin{aligned} \int \mu_{\xi} ds &= \int C_{\alpha\xi} ds \cdot \mu_{\alpha} + \int C_{\beta\xi} ds \cdot \mu_{\beta} \\ &= A_{\alpha} \cdot \mu_{\alpha} + A_{\beta} \cdot \mu_{\beta} \end{aligned} \quad (5.11)$$

where A_{α} and A_{β} have the units of length.

For DECT, when the CT data are collected with two different energy spectra, $\psi_H(E)$ and $\psi_L(E)$, the resulting measurements are:

$$I_L(A_{\alpha}, A_{\beta}) = \int \psi_L(E) \cdot \exp[-A_{\alpha}\mu_{\alpha}(E) - A_{\beta}\mu_{\beta}(E)] dE \quad (5.12)$$

$$I_H(A_{\alpha}, A_{\beta}) = \int \psi_H(E) \cdot \exp[-A_{\alpha}\mu_{\alpha}(E) - A_{\beta}\mu_{\beta}(E)] dE \quad (5.13)$$

Here, subscripts “H” and “L” symbolize the high- and low-kVp scans, respectively. The linear attenuation coefficient of two materials μ_{α} and μ_{β} are known, so from the above two equations, the coefficients A_{α} and A_{β} can be calculated in the calibration step. As long as accurate A_{α} and A_{β} are known, and the incident tube spectrum are kept the same for imaging, the linear attenuation integral for any material, can be calculated from (5.11), and the reconstruction step is followed to reconstruct the object being imaged.

The calibration of the coefficients A_α and A_β is the most important step, which determines the accuracy of the following steps. There are many methods for calibration (Chuang and Huang, 1988), and the most common and straightforward one is through the Taylor series approximation of the logarithmic transform of Equations (5.12) and (5.13).

5.2.2 Analytical approximation to estimate noise properties in dual-energy derived sinograms

The analytic approximations to estimate the variance of the synthesized monoenergetic sinogram are based on the work of Doost-Hoseini (Doost-Hoseini, 1984).

The variance of the monoenergetic sinogram is approximated by

$$\sigma_m^2 = \frac{(f_1(E_m)m_{22} - f_2(E_m)m_{21})^2 \frac{\sigma_1^2}{I_1^2} + (f_1(E_m)m_{12} - f_2(E_m)m_{11})^2 \frac{\sigma_2^2}{I_2^2}}{(m_{11}m_{22} - m_{12}m_{21})^2} \quad (5.14)$$

where I_1 and I_2 and σ_1^2 and σ_2^2 are the integrated photon signals and variances for the two kVp scans, $f_1(E)$ and $f_2(E)$ are the energy dependence of the attenuation coefficients of the two basis materials, E_m is the target energy and $m_{ij} = (1/I_i)(\partial I_i / \partial A_j)$ was the variation of signal intensity with amount of basis material, and A_j was the object-dependent coefficient for material basis.. It has been shown that σ_m reaches its minimum at an optimum target energy E_{opt} , which is a function of object thickness (Doost-Hoseini, 1984).

Since the linear attenuation coefficient of any object is also energy dependent, based on Equation (5.14), the energy-dependent coefficient of

variation (COV) for any object in the monoenergetic sinogram domain can be studied.

$$\text{COV}_{E_m} = \frac{\sigma_m}{\mu_m} \quad (5.15)$$

In Equation (5.15), COV_{E_m} is the coefficient of variation in the monoenergetic sinogram at target the energy, while σ_m is the noise of the object in the sinogram domain at the target energy E_m and μ_m is the linear attenuation coefficient of the object at energy E_m . Based on Equation (5.14) and (5.15), the normalized COV_{E_m} for the target energy E_m ranging from 10 to 525 keV with 1 keV increments can be calculated, where the normalized COV_{E_m} is the COV_{E_m} divided by the minimum value of COV at the optimal energy.

This derivation used a first order Taylor approximation and ignored polyenergetic beam hardening effects. In order to confirm this analytic relationship, polyenergetic simulations was also performed to estimate the noise of the synthesized monoenergetic data in energies from the same energy range.

5.2.3 Simulation tools

To overcome the limitations of analytical approximation, simulation studies of noise and bias properties for dual energy based PET attenuation correction were performed.

5.2.3.1 CT and PET simulators

The CATSIM package was used for simulation of the CT images and

estimation of the CT radiation dose. A detailed description of CATSIM can be found in the previous chapter and some other literature (De Man *et al.*, 2007). The CT simulations included the effects of the x-ray tube spectra, beam conditioning, and quantum noise. The CT simulation models the effects of the X-ray source focal spot, polychromatic tube spectra, beam conditioning, bowtie filter, and beam hardening. The PET simulator ASIM was used to simulate PET images, which included the physical effects of attenuation, background noise, and photon counting. The detailed description of the ASIM simulator can be found in the previous chapter.

5.2.3.2 Test objects

Three test phantoms were simulated. The first was a 10 cm diameter and 10 cm long water cylinder. The second was a uniform 20 cm × 30 cm elliptical water cylinder, with a 10 cm axial dimension. The third was derived from the NURBS-based cardiac-torso (NCAT) phantom (Segars, 2001; Segars *et al.*, 2008). The NCAT phantom had three regions with focal FDG uptake: A 1.6-cm-diameter bone lesion, a 3-cm-diameter contrast enhanced liver lesion and a 3-cm-diameter soft tissue lesion. The PET activity distribution was set to tracer uptake ratios of (background : liver : lung : lesion) = (1: 3 : 0.5 : 6).

The two water phantoms allowed evaluation of energy dependent noise and bias in the DECT derived attenuation map for uniform soft tissues. The rotational symmetry of the first 10 cm diameter water cylinder allowed evaluation of variance in the central projection bin of the synthesized monoenergetic sinograms, which assumed that the noise is uncorrelated

across view angles. The second elliptical water phantom invoked slightly more realistic beam hardening effects, and allowed evaluation of energy dependent noise and bias in the reconstructed DECT derived attenuation images. It was also used for dose estimation and optimization in a torso-like object. The NCAT phantom was used for a more realistic study of the quantitative accuracy of the estimated PET tracer uptake with selected combinations of DECT acquisition parameters for comparison to single kVp CT based attenuation correction with similar radiation dose levels.

5.2.3.3 Simulation procedure for basis material decomposition

The basis material decomposition (BMD) technique described in the previous section was performed with basis materials of aluminum and plastic (polyethylene). For calibration, the polyethylene (PI, $\rho = 0.93 \text{ g/cm}^3$) and aluminum (Al, $\rho = 2.72 \text{ g/cm}^3$) step wedge phantoms were defined (Figure 5.3). The calibration and measurement procedures were as follows:

Calibration:

1. Define step wedges made of aluminum and plastic for calibration (Al: 0-8 steps, 4 mm/step; Plastic: 0-17 steps, 12.5 mm /step).
2. Generate sinograms from high and low kVp scans for the step wedges
3. Calculate $\ln(I_0 / I)$ for each combination of aluminum and plastic steps.
4. Generate calibration coefficients $\{d_i\}$, $\{e_j\}$ for each material:

$$A_\alpha = d_0 + d_1 T_H + d_2 T_L + d_3 T_H T_L + d_4 T_H^2 + d_5 T_L^2 + d_6 (T_H T_L)^2 + d_7 T_H^3 + d_8 T_L^3$$

(5.16)

$$A_{\beta} = e_0 + e_1 T_H + e_2 T_L + e_3 T_H T_L + e_4 T_H^2 + e_5 T_L^2 + e_6 (T_H T_L)^2 + e_7 T_H^3 + e_8 T_L^3 \quad (5.17)$$

where A_{α} and A_{β} are the thickness of the two materials, and $T_H = \ln(I_0 / I)_H$ and $T_L = \ln(I_0 / I)_L$ are for the high (H) and low (L) kVp scans.

Measurements:

5. Generate high and low kVp sinogram data for the test object at the given settings (mAs).
6. Using the generated coefficients $\{d_{ij}\}$, $\{e_{jj}\}$, obtain basis material sinograms of A_{α} and A_{β} for the test object.
7. Convert the basis material density sinograms into basis material attenuation sinograms at desired energy E , using known attenuation values versus E for each material.
8. Sum the attenuation sinograms of each material to obtain the total attenuation sinogram of the test object at the desired energy E .
9. Reconstruct attenuation images at desired energy E .

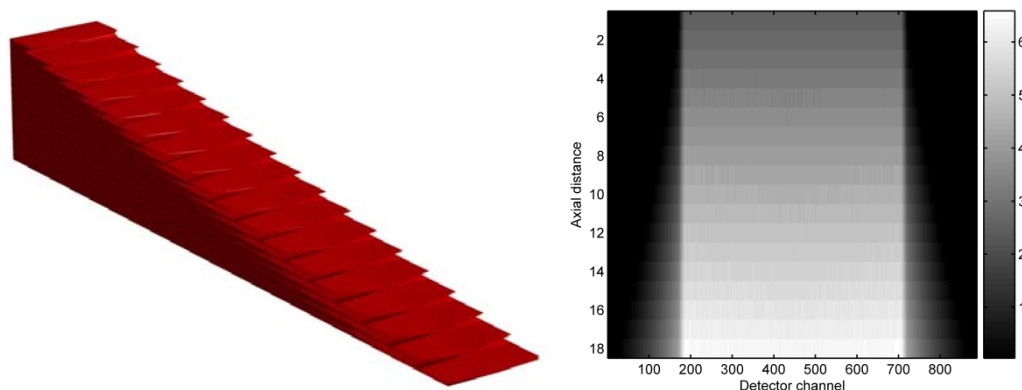


Figure 5.3 Schematic illustration and simulation of x-ray image of step wedge used for BMD calibration.

5.2.4 Study of energy dependent noise and bias properties

First, the noise and bias in the synthesized monoenergetic sinograms of the 10 cm diameter water cylinder were studied. Secondly, the image domain energy-dependent noise and bias for both the 10 cm diameter water cylinder and the 20 cm × 30 cm elliptical water cylinder were evaluated. CT step-and-shoot mode with a gantry rotation time of 0.5 second was simulated for all studies. The dual-energy spectra were based on the GE Lightspeed VCT scanner at 80 and 140 kVp, with added filtration of 0.5 mm Copper following the bowtie filter. The CT slice thickness was 3.125 mm, comparable with the PET slice thickness. Multiple x-ray tube currents were simulated at [64, 91, 110, 128, 181, 256, 362, 512, 724, 1024] mA for each kVp scan. Synthesized monoenergetic data and images were formed at [50, 60, 70, 80, 90, 100, 140, 171, 185, 245, 511] keV covering the range of photon energies for SPECT and PET imaging listed in Table 5.1. All DECT-derived attenuation images were reconstructed to the size of 128 x 128 pixels using filtered back projection (FBP) over a 50 cm field of view (FOV) to match PET

image dimensions. For the 10 cm diameter water cylinder, only one 2D region of interest (ROI) with a diameter of 6 cm was drawn on the cross-section of the phantom for analysis. For the 20 cm × 30 cm elliptical water cylinder, a total of eighteen 2D ROIs each with radius of 2 cm were drawn on the cross-section of the phantom, shown in Figure 5.4. The averaged mean and COV for all ROIs were calculated.

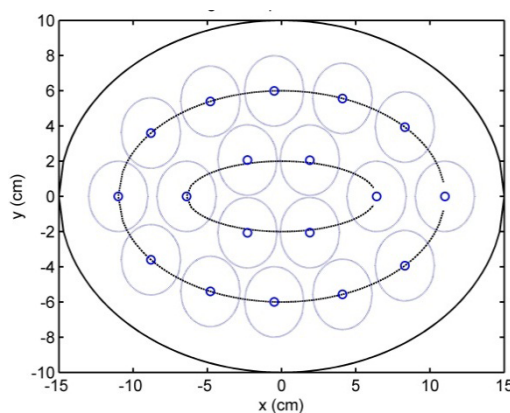


Figure 5.4 Elliptical cylinder phantom with 30 cm × 20 cm cross-section, eighteen 2D ROIs each with radius of 2 cm were drawn for evaluation.

5.2.5 DECT noise suppression and dose minimization for attenuation correction

To further reduce DECT noise, the high and low kVp CT sinograms of the elliptical water cylinder acquired with the tube current of 64, 91, 110, 128, 181, 256, 362, 512, 724, and 1024 mA for each kVp scan were filtered by 2D 5×5 boxcar smoothing, followed by an adaptive trimmed mean filter (ATM) (Hsieh, 1998; Colsher *et al.*, 2008; Xia *et al.*, 2010a; Xia *et al.*, 2012). Then, with the basis material decomposition method and image reconstruction similar to the procedure performed in Section 5.2.3, the sinogram smoothed

DECT-derived attenuation image were generated for each synthesized energy of 50, 60, 70, 80, 90, 100, 140, 171, 185, 245, and 511keV. For each synthesized energy, the COV in the reconstructed attenuation image was evaluated as a function of tube currents for high and low kVp scans.

With the simulation package CATDOSE, this study also estimated the total radiation dose for each combination of tube currents at high and low kVp scans for the 20 cm × 30 cm elliptical water cylinder. Comparing the dose distribution and COV distribution as a function of tube currents for the two kVp CT scans, we estimated the parameters for the DECT acquisition for attenuation correction with the minimum radiation dose. For comparison, a single kVp CT scan of the 20 cm × 30 cm elliptical water cylinder was obtained. The CT technique was selected to be comparable to clinical low dose CTAC protocol (Xia *et al.*, 2012) with a tube voltage of 120 kVp, tube current of 100 mA, and gantry rotation time of 0.5 s. The spectra were conditioned with a bowtie filter only. The slice thickness was the same as the DECT images. Radiation dose was estimated through CATDOSE.

5.2.6 Comparison of PET attenuation correction with dual- and single kVp-derived attenuation map

To study the impact of DECT based attenuation correction on PET quantitation, the NCAT phantom with iodine-based contrast agent was used to compare both DECT and single kVp CT attenuation corrected PET images.

5.2.6.1 Single kVp CT-based PET attenuation correction

The NCAT phantom was first simulated for a step-and-shoot

acquisition with a CT tube voltage of 120 kVp (without added filter, with bowtie filter), tube current of 100 mA, and gantry rotation time of 0.5 s. The CT slice thickness was 3.125 mm, comparable with the PET slice thickness. The CT image was reconstructed to a 128×128 image matrix, using filtered back projection (FBP) over a 50 cm field of view (FOV) to match PET image dimensions. Then a modified version of the bilinear transformation method that relates the CT number to the attenuation coefficient at 511keV was used to generate the attenuation image for PET (Kinahan *et al.*, 2003; Goh *et al.*, 1997). Figure 5.5 shows the modified version of the bilinear transformation used in the study. In the modified method, the slopes for the transformation line of the soft-tissue and bone were estimated with the best fit using the known true values. With the generated attenuation map, both noise-free and noisy attenuation corrected PET images were reconstructed using weighted OSEM (16 subsets, 14 iterations) on a 128 x 128 pixel matrix over a 50 cm FOV.

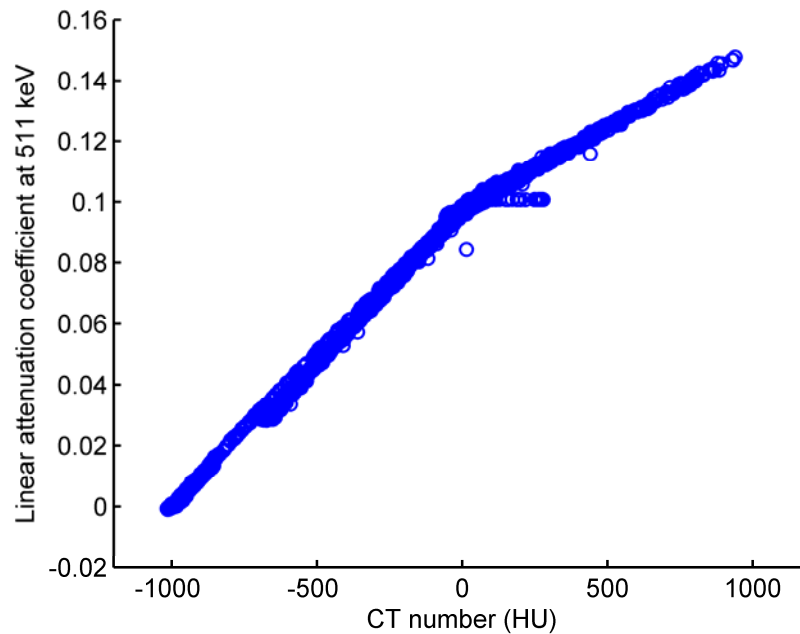


Figure 5.5 Modified version of the bilinear transformation used in the study.

The slopes for the transformation line of the soft-tissue and bone were estimated with the best fit using the known true values.

5.2.6.2 DECT-based PET attenuation correction

The data flow of DECT-based PET attenuation correction process is shown in Figure 5.6. The same dual energy CT tube spectra described in previous sections were used. The CT tube currents for the high and low kVp scans were selected based on the optimal estimation result of Section 5.2.5 for the elliptical water cylinder, giving the same range of radiation dose as that of 120 kVp 50 mAs single-kVp scan. The CT sinograms for the high and low kVp scans were then smoothed with a 2D 5×5 boxcar followed by the adaptive trimmed mean filter (ATM) for noise suppression. With the basis material decomposition method, the synthesized attenuation image at 511

keV was reconstructed with FBP to 128×128 pixels over the 50 cm FOV. The DECT-derived attenuation image was used for PET attenuation correction. Both noise-free and noisy attenuation corrected PET images were reconstructed using weighted OSEM (16 subsets, 14 iterations) on a 128×128 pixel matrix over a 50 cm FOV.

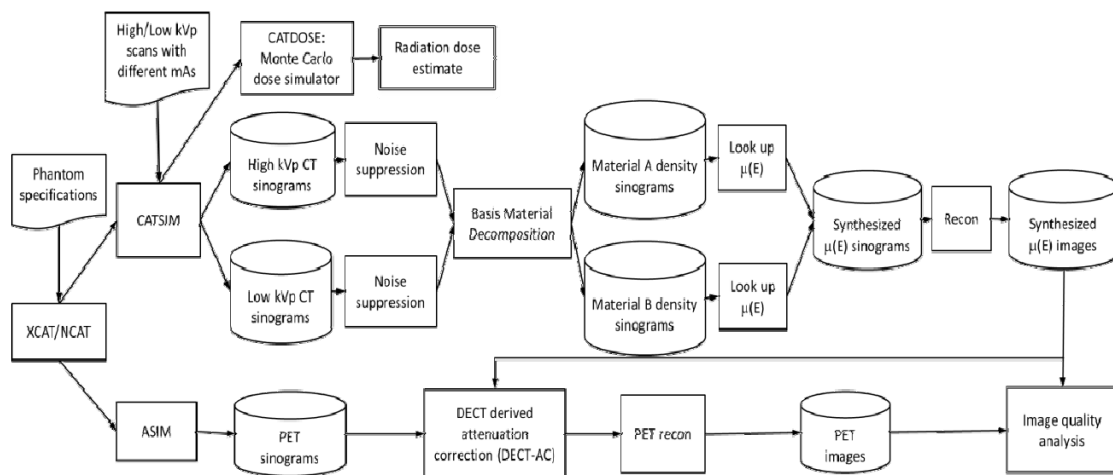


Figure 5.6 Data flow for evaluating use of DECT for PET attenuation correction.

5.2.6.3 Image analysis and comparison

The difference images between the true attenuation image and the single-kVp or DECT derived attenuation image, and the corresponding noise-free and noisy PET image were compared.

For each of the single-kVp and DECT derived attenuation images, six 2D ROIs were drawn on the attenuation image. Correspondingly, six 2D ROIs were drawn on the reconstructed noise-free and noisy PET images for analysis. The total root-mean-square error (RMSE) in the spatial extent of the

object for attenuation images and corresponding attenuation corrected PET images were also calculated. A horizontal profile through the center of the noise-free PET images containing both lesions of the contrast and bone was drawn for comparison.

5.3 Results

5.3.1 Analytical approximation to estimate noise properties in dual-energy derived sinogram

The theoretical prediction result based on Equations (5.14-5.15) and the transmitted spectra at the central bin of the sinogram for the 10 cm diameter water cylinder is shown in Figure 5.7, where the COV is normalized to a minimum value of 1. It can be observed from Figure 5.7 that, with increasing energy the normalized coefficient of variation first decreases to reach its expected minimum value at an energy point between the mean energies of the high and low transmitted spectra. Then it begins to increase until it plateaus near the 160 keV (I-123, SPECT imaging energy), at a level of approximately 3 times the minimum relative COV, and then remains constant with increasing energy (i.e. at PET imaging energies). There are many choices of high and low kVp tube current levels, and Figure 5.7 only shows one combination (256 mA for 80 kVp and 110 mA for 140 kVp). It is found that the theoretically predicted normalized COV vs. synthesized energy does not change significantly with different combination of tube currents.

5.3.2 Impact of beam conditioning and basis material coefficients

Before the added Copper filter (Cu, Z=64, 0.5 mm), the mean energy of the 140 kVp and 80 kVp spectra were 42.7 keV and 59.7 keV, respectively.

After the added filter, the mean energy of the 140 kVp and 80 kVp spectra were 57.1 keV and 77.0 keV, respectively.

The coefficients $\{d_j\}$, $\{e_j\}$ describing the relationships between aluminum and polyethylene thickness and the high- and low-kVp log-transformed projections for the central bin without sinogram smoothing (equations (5.16) and (5.17)) were estimated as:

$$A_{Pl} = 0.0272 + 24.4142T_H - 17.2192T_L + 3.3312T_H T_L - 0.3397T_H^2 - 2.5445T_L^2 + 0.0001T_H^2 T_L^2 - 0.2267T_H^3 + 0.1373T_L^3 \quad (5.16)$$

$$A_{Al} = -0.0088 - 5.1178T_H + 4.7601T_L - 1.7392T_H T_L + 0.4399T_H^2 + 1.1547T_L^2 - 0.0003T_H^2 T_L^2 + 0.0719T_H^3 - 0.0422T_L^3 \quad (5.17)$$

5.3.3 Study of energy dependent noise and bias properties

The simulation results of the normalized COV for the 10 cm diameter water cylinder in the central bin of the synthesized sinogram as a function of synthesized energy is shown in Figure 5.7. The normalized COV vs. synthesized energy in the sinogram domain agrees closely with the theoretical prediction. The normalized COV for the 10 cm diameter water cylinder in the reconstructed attenuation image as a function of synthesized energy is also shown for comparison. In this case, the trend is similar to those predicted and simulated in the sinogram domain, but the exact amplification factor was slightly lower, which may be due to the image reconstruction algorithm and

bowtie filter used. For the same fixed tube currents, the normalized COV in the reconstructed attenuation image as a function of synthesized energy for the elliptical water cylinder is shown in Figure 5.7 as well. It can be seen that the image domain normalized COV curve for the elliptical water cylinder is very close to that of 10 cm water cylinder when no sinogram smoothing was applied.

For all the combinations of tube currents for high and low kVp scans, the percentage bias for both phantoms as a function of synthesized energy were very small, less than 2.4% for diagnostic CT energy range and 0.4% for SPECT and PET energies.

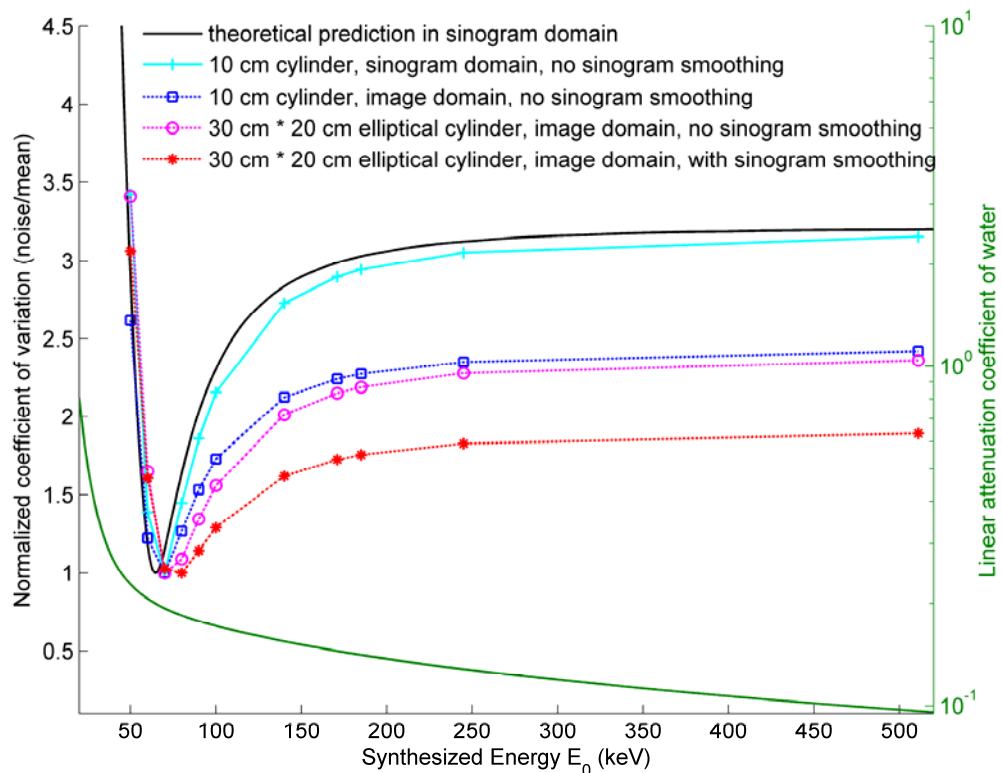


Figure 5.7 Normalized noise vs. synthesized energy of monoenergetic attenuation image. The trend of decreasing linear attenuation coefficient of water with increased energy is also shown in the plot (the vertical axis at right side). Dual

energy CT was acquired at 80 kVp with 256 mA and 140 kVp with 110 mA. Further details are given in the text.

5.3.4 DECT noise suppression and dose minimization for attenuation correction

The total radiation dose (mGy) to the 20 x 30 cm diameter water phantom as a function of tube currents of the high and low kVp scans are shown in Figure 5.8. As expected, with increasing tube currents, the total radiation dose increased.

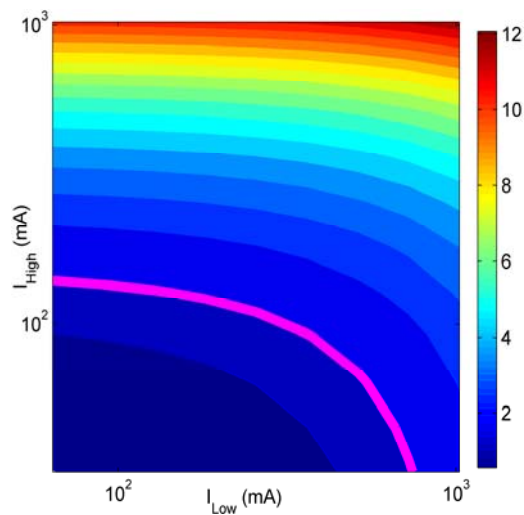


Figure 5.8 Isocontour plot of the radiation dose (mGy) to a 20 x 30 cm diameter water phantom acquired as a function of mAs for high vs. low energy (kVp) scans. The tube current levels that result in the same radiation dose as a low-dose single CT scan (120 kVp, 50 mAs) are plotted as the solid curve.

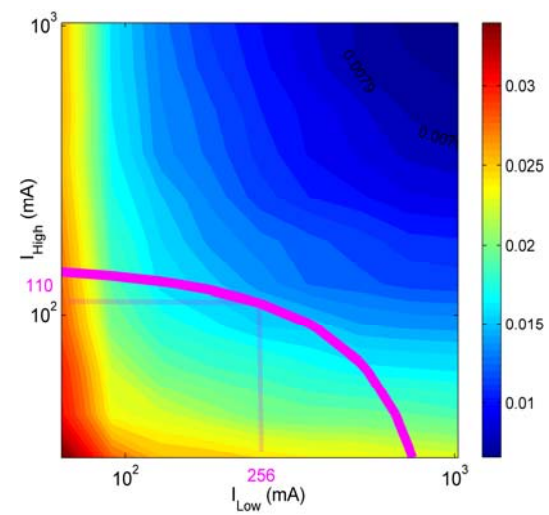


Figure 5.9 Isocontour plot of coefficient of variation of DECT-derived attenuation map of elliptical water cylinder at 511 keV (PET photon energy) acquired with different CT tube currents at high and low kVps, respectively. The values obtained with DECT that have the same radiation dose as that of a single CT scan of 120 kVp, 50 mAs are shown with curve copied

from Figure 5.8.

Figure 5.9 shows the averaged COV of the eighteen 2D ROIs in the reconstructed attenuation image with sinogram smoothing as a function of tube currents for high and low kVp scans for the elliptical water phantom. The values acquired with DECT tube currents that give the same radiation dose as that of a single kVp scan of 120 kVp, 50 mAs are also highlighted. It can be observed that, in general, COV vs. tube currents in Figure 5.9 has an inverse relationship with that of dose vs. tube currents in Figure 5.8. Based on Figure 5.9, one can estimate the optimal combination of the tube currents that gave the same radiation dose as a single kVp CT scan, but generate an attenuation image at 511 keV (PET photon energy) with the minimum COV, which are 110 mA for the 140 kVp scan and 256 mA for the 80 kVp scan.

At the optimal tube current combination, the image domain normalized COV vs. synthesized energy for the elliptical water cylinder with sinogram smoothing is also shown in Figure 5.7 for comparison, which shows a reduction in noise at higher photon energies. The trend of normalized COV vs. energy for the sinogram smoothing case is the same as that without sinogram smoothing, but the noise amplification factor is reduced from 2.4 to 1.9 for SPECT and PET photon energies.

5.3.5 Comparison of PET attenuation correction with DECT and single kVp – derived attenuation map

Both the DECT and single kVp derived attenuation images were

generated with roughly comparable radiation dose. At fixed optimal tube currents for high and low kVp CT scans, Figure 5.10 shows the comparison of attenuation images of the NCAT phantom derived from the DECT or single-kVp scans. Table 5.2 lists the bias in each ROI and the total object RMSE for the two attenuation images. Both PET attenuation images have bias in the contrast agent region, 5.4% for the DECT-derived attenuation image compared to 11.0% in the single-kVp based image. The total normalized RMSE for the object support region in the attenuation image is 2.6% with single-kVp based estimation and to 1.9% with the DECT method.

The corresponding reconstructed PET images are shown in Figure 5.11. The first row of Figure 5.11 shows (from left to right) the reconstructed noise-free PET image with perfect attenuation correction, the noisy PET image attenuation corrected with the DECT method, and the one attenuation corrected with single-kVp method. The second row of Figure 5.11 shows the difference image between the reconstructed PET images and the noise-free truth. The ROIs and profile for comparison are also illustrated in Figure 5.11. The ROI quantitation results are compared in Table 5.3. Figure 5.12 shows the comparison of profiles in the reconstructed noise-free PET images attenuation corrected with the DECT and single-kVp derived methods. It can be observed that the PET image attenuation corrected with DECT method slightly reduced RMSE for the total image and overall bias, and reduced the bias in contrast agent by a factor of approximately 2.6.

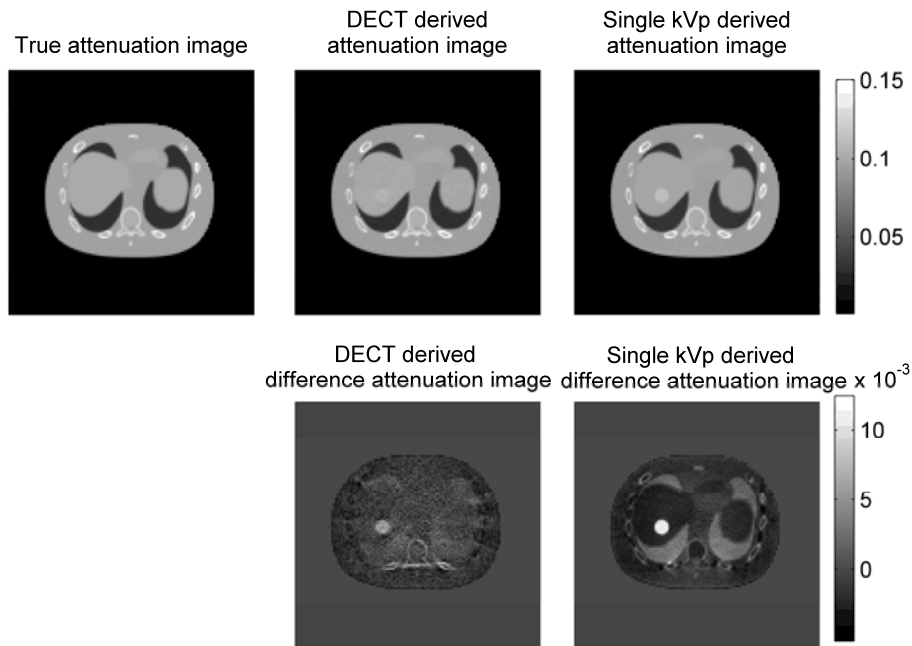


Figure 5.10 Comparison of attenuation image at 511 keV.

Table 5.2 Comparison of bias and RMSE in the DECT and SCT derived attenuation images at 511 keV for the NCAT phantom.

	ROI 1 Contrast (hot)	ROI 2 Soft tissue (hot)	ROI 3 Bone (hot)	ROI 4 Spine (normal)	ROI 5 Background (normal)	ROI 6 Lung (normal)	Total Object RMSE
DECT bias	5.4%	-0.9%	-0.7%	0.5%	-1.3%	2.5%	1.9%
Single- kVp bias	11.0%	-2.5%	0.7%	-1.5%	-2.0%	11.5%	2.6%

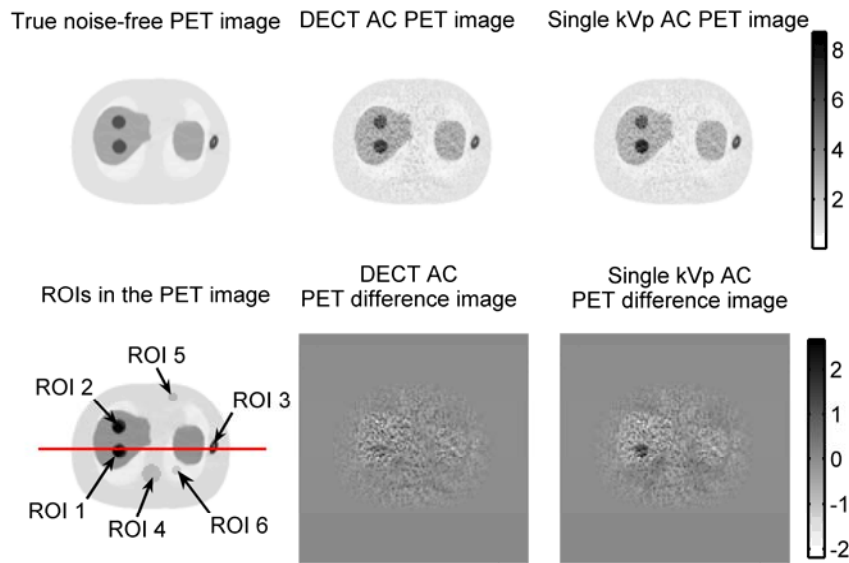


Figure 5.11 Comparison of PET images using DECT and single-kVp CT-based attenuation correction (AC) methods.

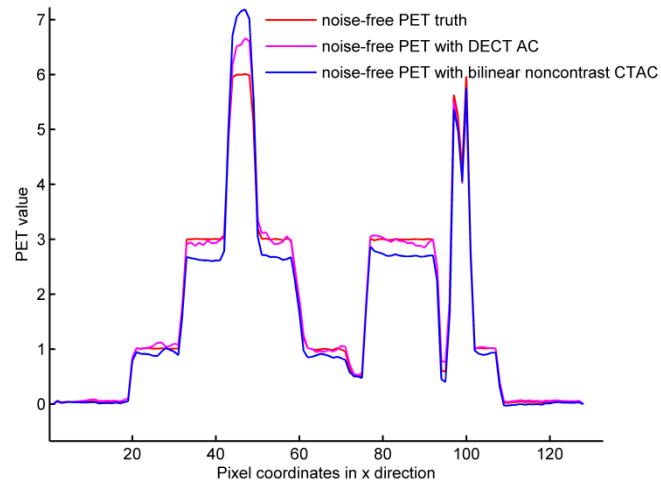


Figure 5.12 Profile comparison of the reconstructed noise-free PET images (OSEM reconstruction, 16 subsets, 14 iterations).

Table 5.3 Comparison of noisy PET images with DECT and single kVp based attenuation correction (AC) with different ROIs in the NCAT phantom (OSEM reconstruction, 16 subsets, 14 iterations).

	ROI 1 Contrast (hot)	ROI 2 Soft tissue (hot)	ROI 3 Bone (hot)	ROI 4 Spine (normal)	ROI 5 Background (normal)	ROI 6 Lung (normal)	Total Object RMSE
PET image truth value	6.0	5.9	5.8	1.0	1.0	0.5	–
Bias in PET with DECT AC	6.9%	-1.2%	-3.3%	0.6%	-1.2%	11.7%	21.0%
Bias in PET with single- kVp AC	17.8%	-5.4%	-1.1%	-16.7%	-4.3%	42.9%	23.3%

5.4 Discussion

Standard methods of CT-based attenuation correction for SPECT and PET have been shown to work well for low density biological objects (Kinahan *et al.*, 2003). In cases where there is PET or SPECT tracer uptake in bone or other confounding high-Z materials (e.g. contrast agent, implants) more accurate methods such as dual-energy CT-based attenuation correction may provide significantly more accurate images (Hasegawa *et al.*, 1993; Kinahan *et al.*, 2006a). DECT is known to be problematic because of the significant noise amplification and the additional patient radiation dose required to perform two scans and to reduce noise. To analyze the properties of DECT-based attenuation correction we focused on the noise and bias of synthesized

monoenergetic attenuation images as a function of the synthesized energy and source currents. We then studied DECT noise suppression and dose minimization for attenuation correction. Finally, we used the NCAT phantom with iodine contrast to compare the noise and bias properties in attenuation corrected PET images.

There are different strategies for dual energy CT imaging, such as separate dual kVp acquisitions, fast-switching interlaced dual kVp acquisitions, simultaneous dual source acquisitions or multi-energy detector-based. Our study was based on dual kVp acquisitions, but can be extended to other strategies as well. We used 0.5 mm Cu as additional flat filters for both high and low kVp scan, since our previous study indicated that this might shape the spectra to be more dose efficient (Xia *et al.*, 2012). Although there are advantages for using different filtration for the two sources and a dual-tube scanner, we used the same filtration for both kVp scans as a single-tube CT scanner is more likely to be combined with a SPECT or PET scanner.

Figure 5.7 shows the normalized coefficient of variation vs. synthesized energy for water phantoms in the sinogram and image domains. It is reasonable to use the normalized coefficient of variation (COV) as our analysis metric, since the linear attenuation coefficient of water is energy dependent, and the energy-dependent noise amplification factor is what we are more interested in. The theoretical prediction was performed in the sinogram domain, and it matches with the simulation results of the 10 cm diameter water cylinder closely. It should be noted that only the central bin is used for simulation of the sinogram COV. The normalized COV vs. energy

trend could vary among different channels due to the transmitted spectra differences, but the general trend would be similar. The theoretical prediction and sinogram simulation do not agree completely, possibly due to the approximation error and ignorance of beam hardening effects in the theoretical prediction. Figure 5.7 also shows that the optimal synthesized energy where the COV reaches its minimum is object-dependent. The energy for the minimum point in the curves for the two water phantoms were slightly different, mainly due to the beam hardening effects for different thicknesses of the objects. In general, however, the minimal COV occurs when the energy is between the mean energy of the transmitted spectra. The different curves in Figure 5.7 indicate that the normalized COV for different phantoms have a similar trend. After reaching its minimum, the normalized COV increased with increasing energy until it plateaued around 160 keV (SPECT energy), and then remained constant with increasing energy up to PET energies. For the given incident spectra, without sinogram smoothing, at SPECT and PET energies the normalized COV in attenuation images for both water phantoms showed an amplification factor of about 2.4 times the lowest level. Sinogram smoothing could further reduce the amplification factor to only 1.9 times. We used 2D 5×5 boxcar followed by adaptive trimmed mean filter for sinogram smoothing. Filtering before logarithmic conversion with the low-pass 2D boxcar will degrade CT resolution. However, for SPECT and PET attenuation correction, the CT image has to be smoothed with post-processing techniques to match the PET resolution. Our previous studies have already shown that a 5×5 boxcar filter for sinogram smoothing was reasonable for PET attenuation

correction (Xia *et al.*, 2012). For the same 10 cm diameter water cylinder, the maximum normalized COV in the image domain is lower than that in the central bin of the sinogram domain, probably due to noise correlations in image reconstruction, type of image reconstruction and kernel filters used, and bowtie filter effects across the total FOV. Figure 5.7 only shows one representative tube current combination for high and low kVp scans, and similar results could be obtained for other tube current combinations. As a check, the bias of the linear attenuation coefficients of the synthesized monoenergetic images were within 2.4% of the known true values across the entire energy range for various tube current combinations.

Figures 5.8-5.9 showed the results of radiation dose as a function of tube currents and the tube current settings optimized for DECT based PET attenuation correction. The dose estimation and parameter optimization were based on the elliptical water phantom. The study on the NCAT phantom-based PET quantitation used the optimal parameters suggested from Figure 5.9. Though it would be more precise if the dose calculation and parameter optimization were based on the NCAT phantom, the estimation based on the elliptical water phantom was reasonable. In practice, it would be hard to evaluate the exact dose delivered at each imaging cross-section for an individual patient.

Figures 5.10-5.12 showed that with the same CT radiation dose as single energy CT, DECT acquisition parameters can be optimized to generate a more accurate attenuation map with less bias leading to reduced PET bias in regions containing CT contrast agent and to similar or reduced RMSE for

the total PET image. It can be seen from Table 5.2 and Table 5.3 that single-kVp based attenuation correction leads to an overestimation of the attenuation coefficient by 11.0% and PET value by 17.8% for contrast agent. With DECT-based method, the overestimation of attenuation coefficient was minimized to 5.4% and PET value to 6.9% for contrast agent. The DECT-based PET attenuation correction showed better over-all performance compared with single-kVp based method. In practice, the single kVp-based attenuation correction method could be modified to reduce PET bias in iodine contrast. However, it would lead to bias for bone as well. In short, the bilinear method is problematic if both bone and iodine are required to be quantitatively accurate in PET images.

The DECT results here are based on the basis material pair {polyethylene, aluminum}, and there are many other choices of basis material pairs (Lehmann *et al.*, 1981; Goh *et al.*, 1997). For example, we also repeated the PET quantitation study with a {water, iodine} material pair (data not shown). The bias in contrast agent region of the attenuation image can be further reduced from 5.4% to -1.6% with the {water, iodine} pair (data not shown), but the bias in the bone and lung regions would be higher than those if the {polyethylene, aluminum} pair was used. The optimal choice of basis material was outside the scope of this study.

In this study, the attenuation correction of the NCAT phantom was performed for PET imaging, but similar conclusions could be drawn for SPECT imaging as well.

5.5 Conclusion

This chapter addressed the energy dependent noise and bias properties for DECT derived attenuation maps for SPECT and PET imaging. The results showed the expected minimum noise value for a synthesized monoenergetic image at an energy between the mean energies of the two transmitted spectra. In addition, we found that for increasing energies, the coefficient of variation of water plateaued near the 160 keV energy of I-123 (i.e. SPECT), at a level of approximately 2.4 times higher than the minimum coefficient of variation, and then remained constant with increasing energy (i.e. at PET imaging energies). The trend of coefficient of variation vs. synthesized energy provided confidence in the use of DECT for attenuation correction in PET/CT and SPECT/CT. Analysis of the noise, bias, and radiation dose indicated that there are optimal ranges for the mAs of the high and low kVp scans. We provided a solution for noise suppression and dose optimization, and showed that sinogram smoothing could further reduce the noise amplification in DECT-derived attenuation map. In addition, we showed through appropriate selection of CT techniques, DECT could deliver the same radiation dose as that of a single spectra CT and provide reduced bias and RMSE for PET imaging containing high-Z materials.

Chapter VI: Phantom-based measured experiments on spectra validation

The studies in Chapter IV and Chapter V are all based on simulation studies. Simulations are a very useful scheme to predict the general trend of scanner behavior. It provides a faster and more variable way than building real scanners, and can be performed in a controlled environment with multiple realizations. However, simulation models might not be exactly the same as physical scanners due to various factors. Thus the results from simulations may not agree with results from physically measured data. Though CATSIM and CATDOSE simulators have been validated relative to GE Lightspeed Volumetric Computed Tomography (Lightspeed VCT, General Electric Medical Systems, Waukesha, WI) measurements for a series of properties, more phantom-based measured experiments are needed for characterization and validation purposes. This chapter investigates the phantom-based measured experiments for spectra validation.

6.1 Introduction

6.1.1 Problems of Interest

Since CATSIM and CATDOSE simulators have been validated relative to GE VCT scanner to some degree, and the simulations in general appear to provide a reliable trend. However, more phantom-based physical measurements are needed to link the simulation results to the measured data. It is not surprising to find disagreements between simulation results and the measured data, since there are numerous factors that contribute to any scanner model, including the variability of the system parameters and the

differences of implemented algorithms among different scanners from different manufacturers. Among these factors, the reliability of the x-ray tube energy spectra files used for simulation compared to those generated from real scanner tube have a first-order impact on the simulation accuracy. It has been noticed that there is no documentation about the origins of the spectra files used in CATSIM, nor is detailed filtration information provided. It is believed that the GE VCT scanner has more pre-patient x-ray filtration than accounted for in the CATSIM spectra, possibly due to the amount (thickness) of cooling oil and the tube casing window, which should be modeled in the spectra files. This chapter investigates phantom-based measured experiments to characterize and validate spectra files for use in CATSIM simulation.

6.1.2 Investigation of spectra generators

In this section, several available spectra simulators are investigated.

6.1.2.1 SpekCalc

SpekCalc is a software program for calculating the x-ray emission spectra from tungsten anodes, such as those used in diagnostic radiology and kV radiotherapy x-ray tubes. The theoretical approach was developed by Gavin Poludniowski and Phil Evans at the Institute of Cancer Research, London, UK (Poludniowski *et al.*, 2009). SpekCalc can be downloaded freely³. SpekCalc was created using REALbasic (REAL software, Inc.), and versions

³ http://www.icr.ac.uk/research/research_divisions/Radiotherapy_and_Imaging/SpekCalc/index.shtml.

of the executable are available for both Windows and Mac operating systems. With the latest *SpekCalc* version 1.1, the x-ray tube spectra can be calculated for tungsten anodes at diagnostic energy range with user-inputs of kVp, filtration and take-off angle. Figure 6.1 illustrates the emission spectrum from tube at 120 kVp with 7 degree tungsten anode angle and intrinsic filtration.

The theoretical approach underlying *SpekCalc* combines Monte Carlo methods, analytical theory and semi-empirical models. Monte Carlo methods treat particle transport with great rigor but are more time-consuming. Semi-empirical models of X-ray production treat the penetration and energy loss of the incident electron beam crudely but with less computation burden (Poludniowski *et al.*, 2009; Birch and Marshall, 1979). In *SpekCalc*, the survival probabilities for an electron reaching certain depths within the target, and the electron energy distributions at those depths, have been pre-calculated using Monte Carlo codes of BEAMnrc (Poludniowski *et al.*, 2009; Poludniowski, 2007). The bremsstrahlung cross-section is treated using analytical theory, and the self-filtration within the anode is treated similar to semi-empirical approaches (Poludniowski *et al.*, 2009). The advantages of *SpekCalc* are that it is computationally fast, quick and convenient to provide information (e.g., HVLs) to the user, and flexible to extend its predictions to orthovoltage X-ray beams. However, it has limitation of only calculation for pure tungsten anodes and tungsten-dominated anodes.

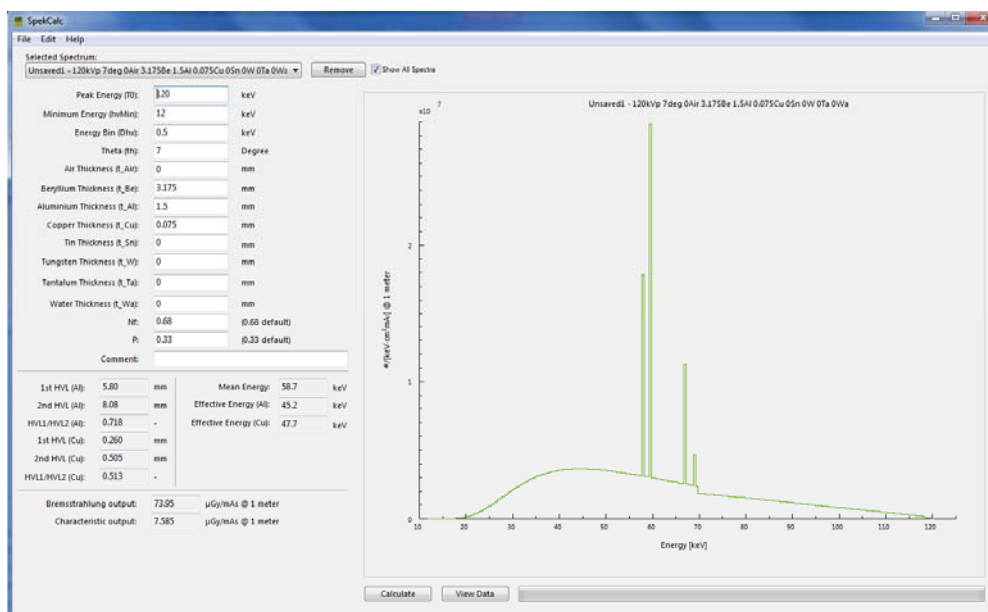


Figure 6.1 Graphic User Interface of SpekCalc program shows an emission spectrum from tube generated at 120 kVp with 7 degree tungsten anode angle and intrinsic filtration.

6.1.2.2 Xspect

Xspect is a collection of programs for modeling x-ray production, attenuation, and detection for radiographic imaging systems. The code was developed at Henry Ford Health Systems (Detroit, MI) and can run on both Windows and Unix platforms. With Xspect's semi-empirical models (Flynn and Samei, 1999) for electron target tubes, users are able to generate the spectral distribution of the x-ray source (Samei and Flynn, 2003; Storm, 1972a, b).

6.2 Materials and Methods

6.2.1 Overview of the study

The overview of the study can be illustrated in Figure 6.2. After

phantom preparation and protocol design, both physically measured experiment and simulation were performed with the same phantom and protocol. After pre-processing of the raw data, we were able to get the sinograms after the standard negative of the logarithmic conversion (Neglog) step for both data sets. Then, we performed analysis and comparison of the two data sets by drawing the same region of interest (ROI) over corresponding areas. In this way, we could evaluate the new spectra used for simulation. It should be noted that a carefully designed protocol is needed for this spectral validation study so that other physical effects, such as quantum noise and electronic noise in X-ray generation and propagation could be minimized.

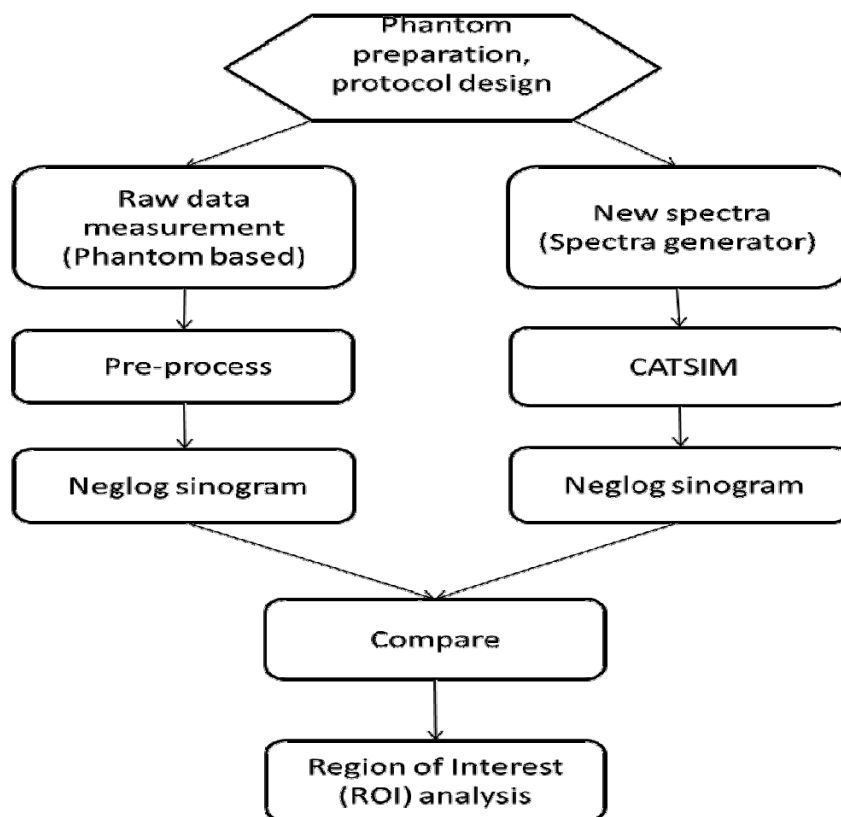


Figure 6.2 The overview of the spectra validation study flow.

6.2.2 Phantom preparation

The beam hardening slab phantoms and the holder mentioned in this section were designed by Mr. Paul Fitzgerald and built by GE Global Research Center.

Two sets of beam hardening phantom were used. The first set was Polymethyl-methacrylate (PMMA, $\rho = 1.185 \text{ g/cm}^3$) slabs, and the second set was Aluminum slabs (Al, $\rho = 2.737 \text{ g/cm}^3$). There were a total of 16 PMMA slabs, each with average thickness around 23 mm, as shown in Figure 6.3. Table 6.1 listed the measured average thicknesses of each PMMA slab. The Aluminum stack was shown in Figure 6.4. There were a total of 21 Aluminum slabs each with thickness of 3.12 mm and two base slabs, one with thickness of 3.12 mm, and the other with thickness of 9.37 mm. The two sets of beam hardening phantoms made with different materials were used to evaluate beam-hardening properties of the tube spectra when different tube voltage was applied.

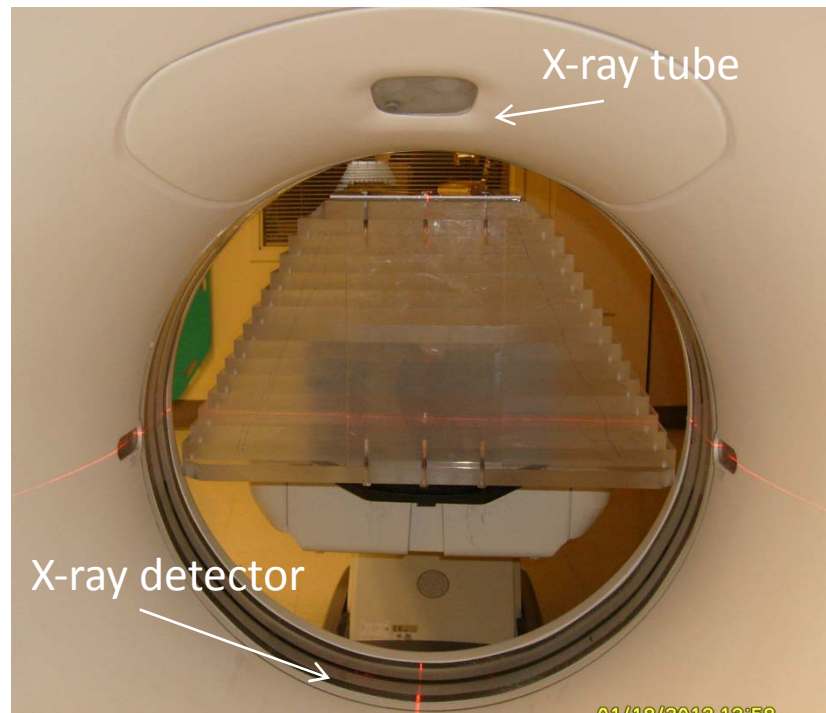


Figure 6.3 PMMA phantom contains a total of 16 slabs, each with average thickness around 23 mm.



Figure 6.4 (a) Aluminum phantom with base of 3.12 mm (b) Aluminum

phantom with base of 9.37 mm. (Image Courtesy of GE Global Research Center).

To carefully control the phantom position during experiment, a heavy phantom holder was used, as shown in Figure 6.5. In addition, to balance the phantom on the phantom holder placed on patient table, a series of counterweights were used, as shown in Figure 6.6.

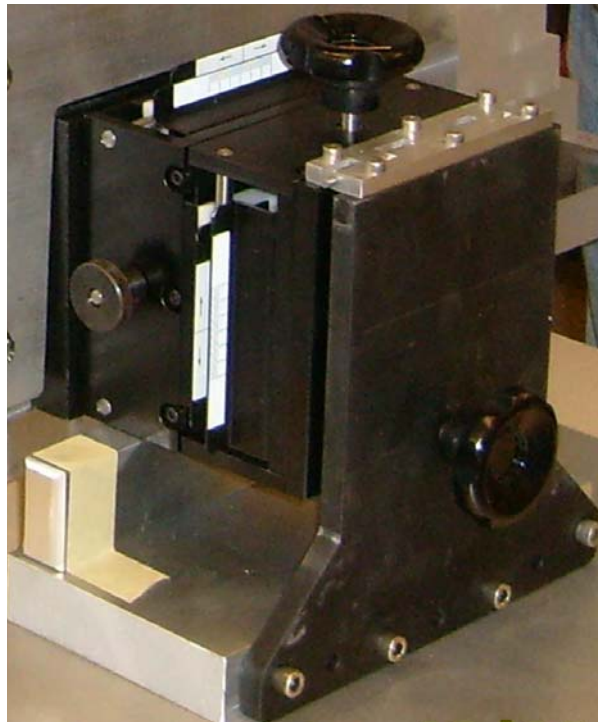


Figure 6.5 Heavy phantom holder used in the experiment to hold the beam hardening phantoms. Note there are three knobs on the holder to precisely adjust the phantom position, and a support block under the adjuster of the phantom holder to provide extra support and stability.



Figure 6.6 A series of counterweights were used to balance the heavy phantom on the phantom holder.

Table 6.1 The measured average thicknesses of each PMMA slab.

Slab Position in the Stack	Slab Number	Average Thickness (mm)
Base	1	22.56
	2	23.77
	3	22.44
	4	22.76
	5	22.67
	6	22.83
	7	22.82
	8	22.19
Middle	9	23.34
	10	22.73
	11	22.28
	12	23.50
	13	23.16
	14	22.59
	15	23.10
Top	16	22.56

6.2.3 Experiment flow

The phantom-based measured experiment was performed on a GE Lightspeed Volumetric Computed Tomography (Lightspeed VCT, General Electric Medical Systems, Waukesha, WI) scanner at the University of Washington Medical Center.

6.2.3.1 Protocol files and scripts installation

The protocol files for phantom scanning and scripts for data transfer were saved in a USB memory stick and provided by Mr. Paul Fitzgerald from the X-ray and CT laboratory in GE Global Research Center. These protocol files and scripts were installed on the VCT scanner from the USB memory stick before the experiment.

6.2.3.2 Phantom alignment

To get reliable physical measurement, the beam hardening phantoms (PMMA slabs or Aluminum slabs) were assembled on the patient table with the phantom holder to hold the phantom and adjust the precise position. The counterweights were used to balance the whole apparatus. Figure 6.7 illustrates the phantom aligned on the patient table. The detailed steps for phantom alignment were as follows:

1. Install the “heavy phantom holder” on the patient table.
2. Adjust the holder parallel to the edges of the patient table to guarantee the proper phantom yaw, since the phantom yaw depends on the yaw of the holder with respect to the table.
3. Add the counterweights, in the order from the smallest to the

largest. Note that the counterweights need to be installed before installing any phantom, and can only be removed after the phantom has been removed.

4. Center the adjusters on the phantom holder.
5. Install the whole stacks of the beam hardening phantom (PMMA stack or Aluminum stack).
6. Make sure to use the lead collimator with minimum slot on top of the phantom to minimize the scatter effects.
7. Adjust the vertical position using the lasers and the patient table height adjustment.
8. Check pitch and yaw with the lasers and levels. Adjust until it seems as close as possible
 - a. Adjust yaw by re-positioning the holder base on the patient table. Remove phantom first, then counterweights, then re-position base, then add counterweights, then phantom.
 - b. In addition to the 3 knobs on the phantom holder, use the support block under the adjuster of the phantom holder to provide extra support and stability, especially for heavier phantoms.
9. Move the table in the Z (rotation) direction and use the laser to approximately center the phantom thickness with the one that's offset from the scan region (out of the scanner). Press the landmark

- button that corresponds to this laser. Then use the z-translation buttons to move to “0” position.
10. Record the displayed height (so that if one accidentally steps on the foot pedal, he or she can return to the correct position).
 11. Run the phantom centering utility to tweak x and y. Use the knobs on the box to do this. Try to get to < 1 mm error.
 12. Note that when adjusting z, both the knob and the set screws on the support block need to be readjusted.
 13. Check the pitch, yaw and roll each time one slab is removed from the phantom stack during the experiment.



Figure 6.7 The whole PMMA phantom aligned in the scanner bore.

6.2.3.3 Phantom scanning

The phantom scanning was performed on the VCT scanner in Service mode. Service mode could be accessed via the “Diagnostic Data Collection” (DDC) tool, which allows the user to scan and create scan files using user selectable scan types and parameters as an aid in troubleshooting and verifying the data integrity of the DAS/Detector subsystem. The detailed steps for phantom scanning are as follows:

1. Go into service mode (button on upper left of right monitor).
2. Click “Diagnostics” button.
3. Click “Diagnostic Data Collection (DDC)”.
4. Click “Protocol Name” button (left side).
5. Select the protocol from the list and click “Load”. Use each mA; each kVp will be run.
6. Click “Accept Rx”. (Make sure that the tube position is zero degree when starting the scanning).
7. Record the exam number that shows up in the “scan list” dialog.
8. Push the exposure button on the console for each kVp.
9. Go to step 4 and do the next mA.
10. Install and align the next phantom (i.e., adding or removing one slab of the phantom stack at a time).
11. Go to step 1. Record the exam numbers that correspond to each phantom and mA.

The details of the protocol used in step 5 are listed in Table 6.2.

Table 6.2 Details of protocol used for phantom scanning

Scan mode:	Static
Tube voltage (kVp):	80, 100,120,140
Tube current (mA):	500
Scan time (sec):	1
Trigger rate:	984
Focal spot size:	Large
Collimation:	0.625 mm × 4
DAS gain:	4
Gantry filter:	Air

6.2.3.4 Data export

The collected raw data were saved as '*.ffp' format files and exported with Perl scripts provided by GE Global Research Center. These data were transferred to GE Global Research Center for interpretation of the proprietary raw data format and pre-processing, and sent back to University of Washington as pre-processed raw data, with each file of size 888x984x4, 32 bit real.

6.2.4 Data processing and analysis

6.2.4.1 Experiment data visualization and analysis

Data processing and analysis were performed at both University of Washington and GE Global Research Center. At the University of

Washington, based on the preprocessed data, a graphic user interface (GUI) was programmed with MATLAB version 7.10.0 (The Math Works, Inc) to visualize the raw data post negative-logarithmic conversion step. Figure 6.8 shows a screen shot of the GUI.

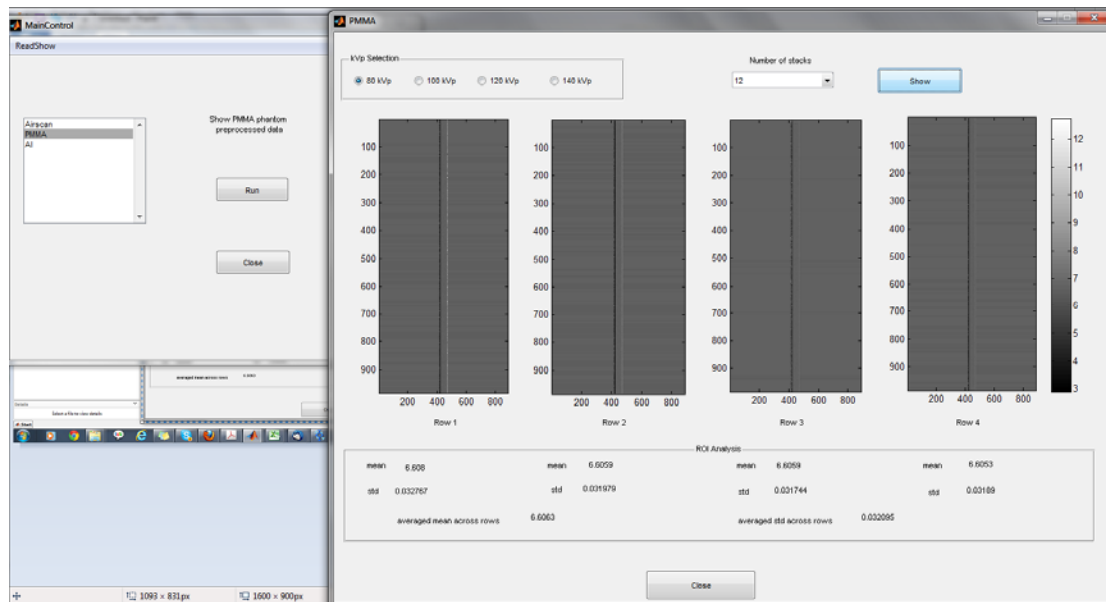


Figure 6.8 Screen shot of the graphic user interface for visualization of the preprocessed raw data of the VCT scanned beam hardening phantoms.

On the main panel of the GUI, user could select the data sets for visualization: air scan, PMMA phantom or Aluminum phantom. After clicking the 'Run' button, a corresponding panel would pop up, which allows the user to choose experiment condition, such as tube voltage and the number of slabs used for the phantom. After clicking the 'Show' button, the four rows of sinogram data were shown. For data collected on each detector row, a rectangular ROI was drawn, covering the data collected on the central 20 detector channels (within the range of the collimator) and all triggered views. The mean value and standard deviation of each ROI for each detector row r

was denoted m_r and σ_r respectively. Then the mean projection value, M , and noise, σ , were calculated as the average of m_r and σ_r across R detectors.

$$m_r = \frac{1}{I} \sum_{i \in ROI_r} f_{ir} \quad (6.1)$$

$$M = \frac{1}{R} \sum_{r=1}^R m_r \quad (6.2)$$

$$\sigma_r = \sqrt{\frac{1}{I-1} \sum_{i \in ROI_r} (f_{ir} - m_r)^2} \quad (6.3)$$

$$\sigma = \frac{1}{R} \sum_{r=1}^R \sigma_r \quad (6.4)$$

where f_{ir} was the value of pixel i in r th ROI, and $r = 1, 2, \dots, R$, and $R = 4$.

The values of m_r and σ_r for each detector row, and the mean projection value M and noise σ were displayed on the GUI panel.

6.2.4.2 Simulation of the beam hardening phantom with new spectra

To compare the results collected in the experiment, and to validate the spectra used in the CATSIM simulation, two sets of spectra data were used for simulation. The first set of spectra data were the original default spectra files provided in CATSIM, and the second set of spectra data were generated with Xspect with proper amount of intrinsic filtration. Each set of spectra data contains spectra file for tube voltages of 80, 100, 120 and 140 kVps.

Digital phantoms of PMMA slabs and Aluminum slabs with varying thicknesses were defined. Then both sets of phantoms underwent CATSIM

simulation with the above two sets of spectra files. All other simulation parameters were set comparable to the experiment ones, and scatter and noise effects were neglected in simulation.

The post negative logarithmic converted sinogram data from simulation were analyzed with the same procedure as that used for experiment data. The mean value for each ROI and the averaged mean across the ROIs were calculated according to Equations 6.1- 6.4.

6.2.4.3 Comparison of simulated data with experiment collected data

The simulated results for the two different sets of spectra files were compared to the experiment results for both the PMMA phantom and Aluminum phantom. The relative error vs. phantom thicknesses for the two beam hardening phantoms were calculated and compared between the two different spectra sets. The relative error (R_{error}) was calculated as:

$$R_{\text{error}} = \frac{M_{\text{sim}} - M_{\text{exp}}}{M_{\text{sim}}} \times 100\% \quad (6.5)$$

Where M_{sim} and M_{exp} are simulated and experiment measured mean projection value, respectively.

6.3 Results

6.3.1 Spectra comparison

The original spectra data provided in CATSIM, and the spectra data generated with Xspect without and with intrinsic filtration are plotted for comparison for each kVp in Figure 6.9. In those figures, the spectra were

normalized to make the area under each curve to be one and compared. It can be seen that the relative photon amplitudes for each photon energy bin were different among different spectra.

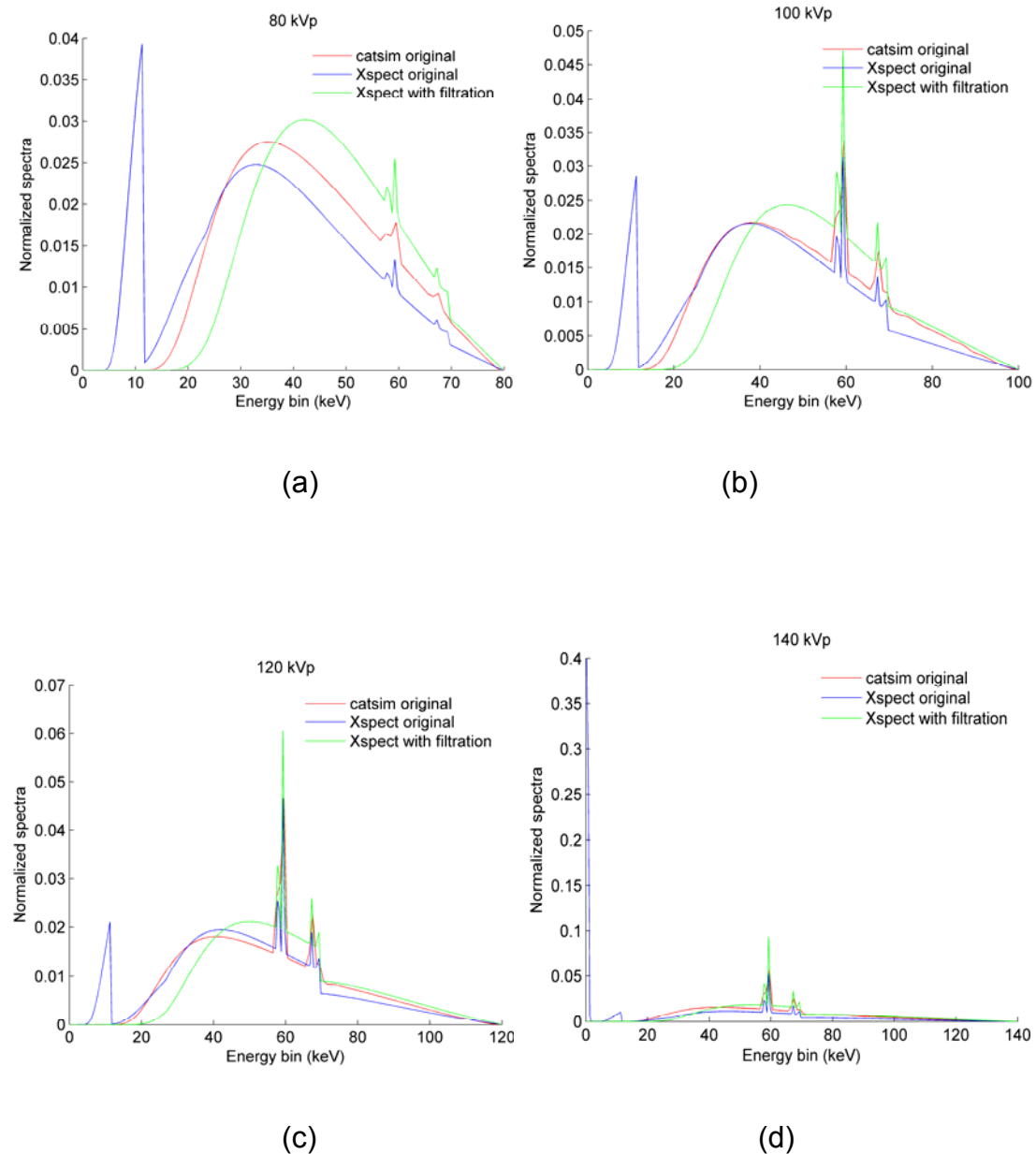


Figure 6.9 Comparison of normalized spectra among the original spectra data provided in CATSIM, and the spectra data generated with Xspect without filtration, and the spectra generated with Xspect with proper intrinsic filtration. (a) 80 kVp (b) 100 kVp (c) 120 kVp and (d) 140 kVp.

6.3.2 Experiment results on spectra validation

The experimentally measured mean projection value as a function of phantom thickness for PMMA phantom and Al phantom are shown in Figure 6.10 and Figure 6.11, respectively.

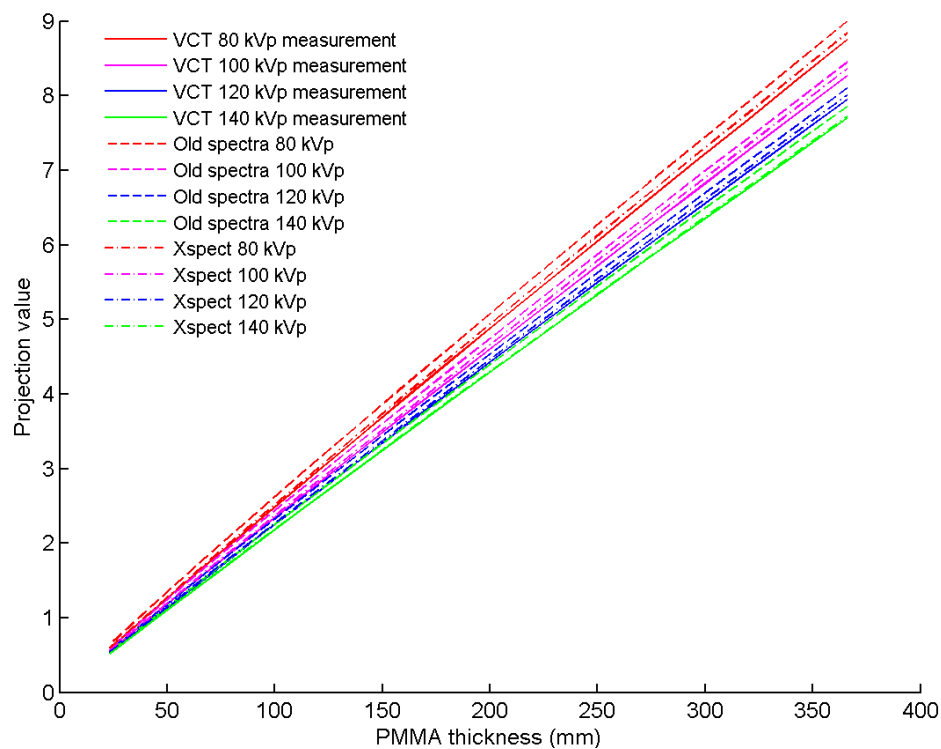


Figure 6.10 Mean projection value vs. PMMA phantom thickness for VCT scanner, for simulated data with old spectra, and for simulated data with Xspect spectra with proper filtration.

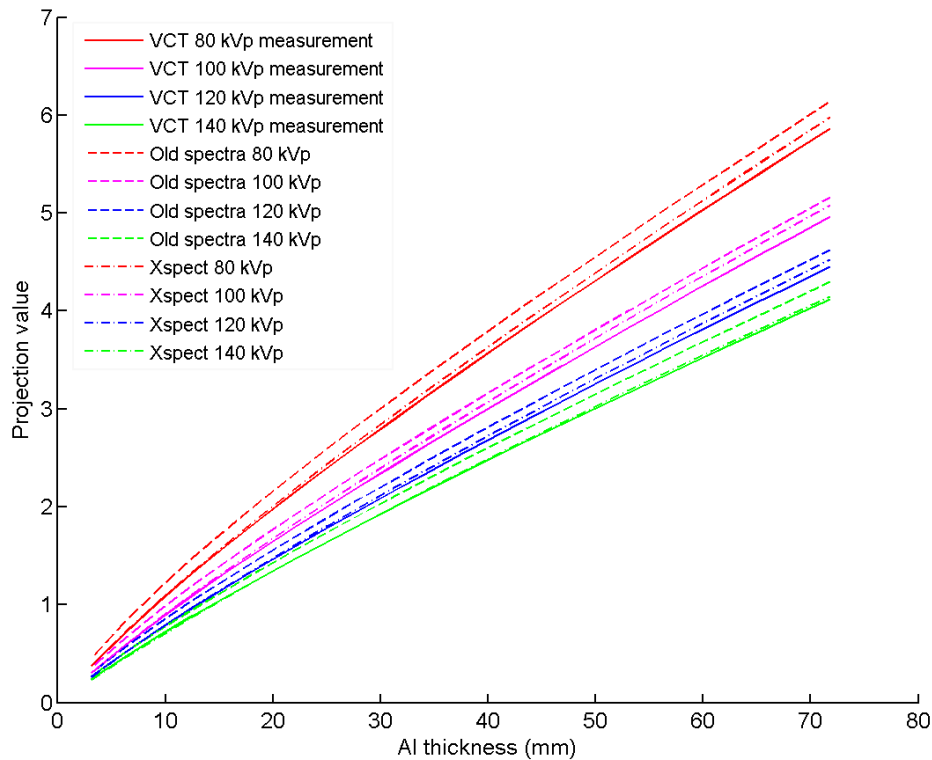


Figure 6.11 Mean projection value vs. Al phantom thickness for VCT scanner, for simulated data with old spectra, and for simulated data with Xspect spectra with proper filtration.

6.3.3 Simulation results on spectra validation

The simulated results with old spectra and Xspect spectra with proper filtration were also shown in Figure 6.10- Figure 6.11. As expected, increased phantom thickness increases projection value, and more beam hardening effects are observed for the Al phantom compared to PMMA phantom for the same phantom thickness. Figures 6.10- 6.11 also suggest that compared to the old spectra, the simulated data with Xspect spectra are closer to the measured data.

6.3.4 Comparison of the two sets of spectra data

To further compare the two sets of spectra data, Figure 6.12

shows the relative error for the old spectra for the PMMA phantom, and Figure 6.13 shows the relative error for the new spectra with the PMMA phantom. Correspondingly, Figure 6.14 and Figure 6.15 show the relative error for the old spectra and new spectra with the Al phantom.

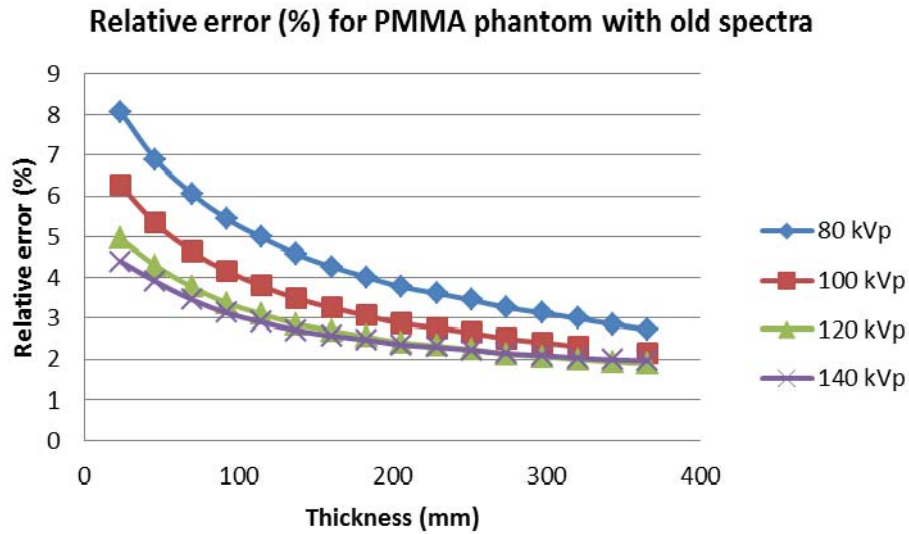


Figure 6.12 The calculated relative error for the old spectra for PMMA phantom.

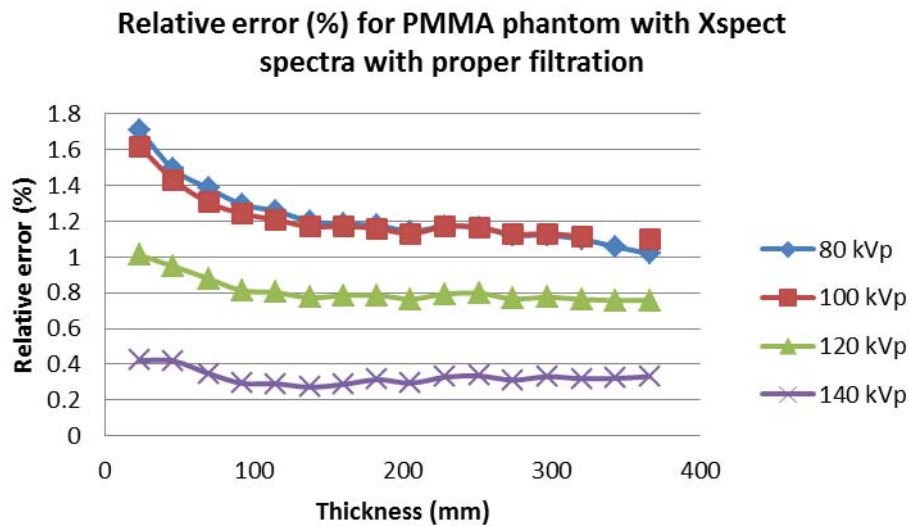


Figure 6.13 The calculated relative error for the new spectra generated with Xspect for PMMA phantom.

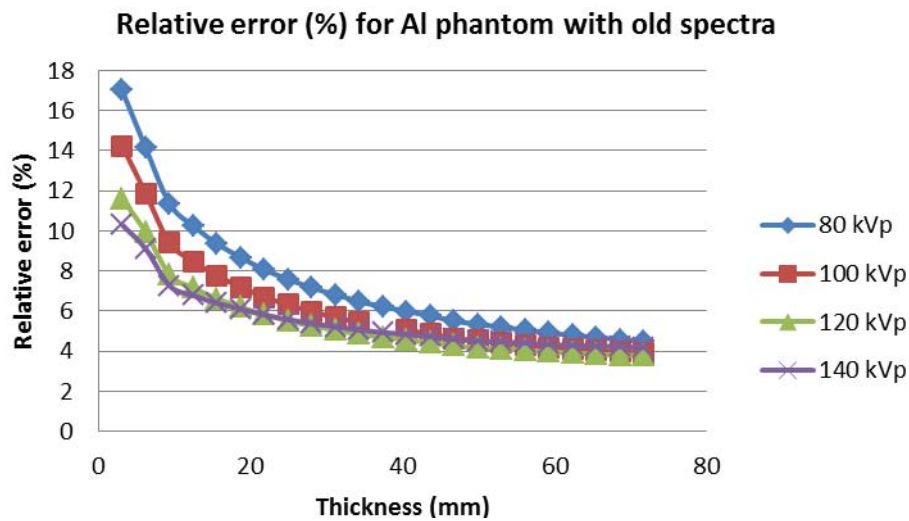


Figure 6.14 The calculated relative error for the old spectra for Al phantom.

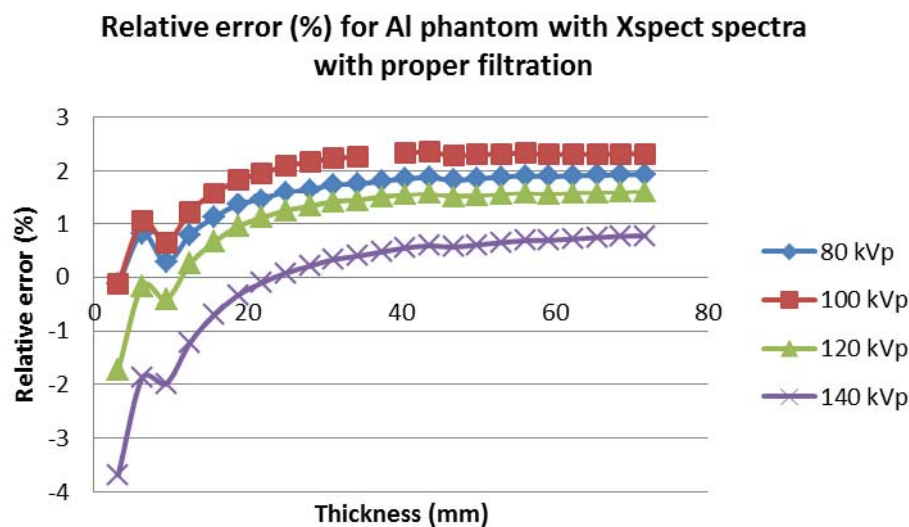


Figure 6.15 The calculated relative error for the new spectra generated with Xspect for Al phantom.

6.4 Discussion

The reliability of the spectra files used for simulation has a first-order impact on the simulation accuracy. To validate spectra files used for simulation, phantom-based measured experiments were performed and compared with simulation results based on different sets of spectra files. Our

experiment results were very close to the results obtained at GRC, with the intra-scanner difference below 0.5%. In addition, simulation results based on the spectra generated with Xspect with proper amount of intrinsic filtration agree very well with measured data for both PMMA and Al phantoms. Compared to the old spectra, with Xspect spectra and proper filtration, the maximum relative error among all kVps was reduced from 8.1% to 1.7% for the PMMA phantom, and was reduced from 17.0% to 2.3% for the Al phantom.

The simulation for spectra validation was performed with ideal conditions, without considering scatter, quantum noise and detector electronic noise, etc. When considering quantum noise, more experiments are needed to adjust the absolute photon numbers in each energy bin to better match with measured data. In that case, a scaling factor for the spectra file should be determined. We tried the current spectra for simulation considering photon quantum noise case, and found that without proper scaling there would be photon starvation for thick phantom layers. A more reliable noise model, especially the low photon model for CATSIM will be needed for future studies, and are beyond the scope of this experiment.

6.5 Conclusion

This chapter discussed the phantom-based measured experiment for simulation spectra validation. Simulation results based on the spectra generated with Xspect with the proper amount of intrinsic filtration agree very well with measured data for both PMMA and Al phantoms. For CATSIM simulation, the spectra files generated with Xspect with proper amount of

intrinsic filtration are preferred to the original x-ray tube spectra files. When considering photon quantum noise, proper scaling of the absolute photon number in each energy bin is needed. A more reliable noise model, especially a low photon model considering both quantum noise and electronic noise is desired and will be studied in the future.

Chapter VII: Summary and future work

This chapter summarizes the contributions of the thesis, and proposes future work.

7.1 Summary of contributions

Two significant challenges for quantitative PET/CT imaging come from patient's respiratory motion and estimation of the attenuation coefficients for high atomic number materials. Longer duration respiratory-gated CT has been proposed for attenuation correction of phase-matched respiratory-gated PET and motion estimation. Dual energy CT has been proposed for accurate CT-based PET attenuation correction for imaging of high atomic number materials. However, for both methods, the radiation dose from the CT scan is unacceptably high with the current CT techniques. The main focus of this thesis is the formulation of strategies for CT radiation dose minimization for PET attenuation correction in quantitative PET imaging. The specific aims for this thesis were to: 1) develop CT acquisition methods for PET attenuation correction with reduced radiation dose that enable quantitative PET imaging; 2) develop compensation methods to suppress increases in CT noise and/or bias from dose reduction methods; 3) investigate and evaluate the impact of CT dose reduction and noise compensation strategies on both CT and PET image quality; 4) understand and reduce noise propagation from dual energy CT (DECT) acquisitions used for attenuation correction for PET or SPECT. These specific aims have been accomplished in the studies presented in Chapters III to VI.

To accomplish these aims, simulation tools for PET and CT have been developed and/or improved, as discussed in Chapter III. Specifically, the major contributions in the work presented in Chapter III are: 1) generation of material files of CT contrast agent with varying concentrations used for simulation; 2) improvement of beam hardening correction function for multiple detector rows; 3) improvement of Poisson random number generator in FreeMat; 4) simulation of CATSIM with NCAT integration and contrast agent enhancement in phantom; 5) modification to CATSIM structure used for efficient generation of multiple realizations; and 6) development and implementation of sinogram preprocessing algorithms for CT simulator.

In Chapter IV, the simulation studies for ultra-low dose CT used for PET attenuation correction were presented. The motivation for the study in that chapter is to reduce CT radiation dose dramatically, enabling longer duration CT scans for respiratory gated CT that is phase matched with PET for attenuation correction and motion estimation. To the best knowledge of the author, there is no previous published journal paper addressing the problem of reducing CT radiation dose dramatically for quantitative PET imaging. The work in Chapter IV extended standard techniques to achieve dramatic CT radiation dose reduction, benefiting from the reduced requirement of CT for PET attenuation correction. These methods included reducing CT tube current, optimizing CT tube voltage, adding filtration, CT sinogram smoothing and clipping. The impact of these methods on PET quantitation was studied via systematic simulations of different digital phantoms. The work presented in Chapter IV has several contributions. First of all, it demonstrates that ultra-low

dose CT for PET/CT is feasible, and there is significant room to reduce CT radiation dose in the cases where CT is not used for diagnostic or anatomical localization purpose. Secondly, it shows that appropriately choosing tube potential, current and filtration allow lower CT doses at matched PET image quality. Spectra that are higher energy and narrower are generally more dose efficient with respect to PET image quality. Sinogram smoothing could be used to compensate for the increased noise and artifacts at radiation dose reduced CT images, which allows a further reduction of CT dose with no penalty for PET image quantitation. Thirdly, the proposed CT dose reduction methods are clinically and technically feasible, and could be used for longer duration CT scans for respiratory-gated CT that is phase matched with PET data for attenuation correction and motion estimation. In addition, the techniques proposed in Chapter IV are useful for the reduction of patient radiation dose in general. The work in Chapter IV leads to a featured article published in the journal of *Physics in Medicine and Biology*, four international conference papers, several invited oral presentations, and several media reports in medical imaging field.

The work in Chapter V studied the use of dual energy CT for attenuation correction for quantitative bone cancer imaging. Energy dependent noise and bias properties of monoenergetic images synthesized from dual-energy, or dual-kVp, CT acquisitions were evaluated. Associated noise suppression and dose optimization methods were investigated for dual energy CT based PET attenuation correction. There are several main contributions from the work presented in Chapter V. First of all, though it had

already been known that the noise amplification for synthesized sinogram was energy dependent in the diagnostic CT energy range, the noise and bias at SPECT and PET energies were largely unknown at the beginning of the study in Chapter V. The presented work firstly studied the trend of coefficient of variation vs. synthesized energy at SPECT and PET energies. The noise and bias result provides confidence in the use of dual energy CT for attenuation correction in PET/CT and SPECT/CT. Secondly, analysis of the noise, bias, and radiation dose indicates that there are optimal ranges for the mAs of the high and low kVp scans. Thirdly, a solution for noise suppression and dose optimization has been proposed. Fourthly, the work presented shows that through appropriate selection of CT techniques, dual energy CT could deliver the same radiation dose as that of a single spectra CT and provide reduced bias and RMSE for PET imaging containing high-Z materials. This work produced a submitted journal paper, two invited oral presentations, and two conference proceedings.

In Chapter VI, phantom-based measured experiments were performed to validate spectra files used for simulation. The presented work investigated several spectra generators, and validated the generated spectra files with measured experiments on GE VCT scanner. Our experiment results were very close to the results obtained at GE Global Research Center, with the intra-scanner difference below 0.5%. It has been found that spectra generated with Xspect with the proper amount of intrinsic filtration agree very well with measured data for both PMMA and Al phantoms. Compared to the old spectra, with Xspect spectra and proper filtration, the maximum relative error

among all kVps was reduced from 8.1% to 1.7% for the PMMA phantom, and was reduced from 17.0% to 2.3% for the AI phantom. A GUI interface was also developed for experiment data visualization and analysis. The presented work in Chapter VI contributes to the release of an updated CATSIM package with more accurate spectra files, providing confidence for future CT simulations with low-radiation-dose noise models.

7.2 Potential future directions

The work of CT radiation dose reduction for quantitative PET imaging presented in this thesis has several potential future directions.

7.2.1 Simulation tool improvement for dose estimation

The simulation tool used for estimating CT radiation dose is the package of CatDose from CatSim. However, CatDose has some limitations in estimating dose for NCAT phantom, and the accuracy of CatDose needs to be verified. One potential future direction is to compare the estimated radiation dose output from CatDose with the one from CT adaptive Monte Carlo N-Particle eXtended code (MCNPX, Los Alamos National Lab, USA) for the same phantom. MCNPX is a general-purpose Monte Carlo radiation transport code for modeling the interaction of radiation with everything, and it is fully three-dimensional and time dependent. For CT dose estimation, MCNPX has to be adapted to create a CT source (DeMarco *et al.*, 2007).

7.2.2 Simulation tool improvement with more accurate low-dose CT noise model

A potential challenge for presented ultra-low dose study is that system parameters and implemented algorithms may vary among different scanners

from different manufactures. The presented results in the thesis used combinations of wide range of parameters to predict the general scanner behaviors for ultra-low dose situations. However, if we are able to have raw data access tool for some certain scanners and to compare the results from measured experiments with those from simulations on the same scanners at low dose cases, we will be able to establish a link between the simulation and practical measurements.

Thus, one potential future direction is experimental characterization of low-dose CT noise model for simulation on certain scanners, especially at extreme low dose cases when the real signal is buried in both quantum noise and electronic noise. CATSIM simulator was initially developed and verified for high and moderate dose regions to some extent on GE VCT scanner. It would be desirable if the noise model for CATSIM at low dose region considering both quantum noise and electronic noise is characterized experimentally on GE VCT scanner.

For example, the low dose noise characterization can be performed experimentally on the scanner in raw data domain with uniform PMMA cylinder with varying tube current at fixed tube voltage, where the noise is a combination of photon quantum noise and electronic noise. The electronic noise can be measured directly from the scanner with X-ray off.

The established link between the simulation and practical measurements on scanners at ultra-low dose cases could enable simulations to be more reliable for future practical protocol design.

7.2.3 Evaluation of standard CT dose reduction techniques for various object sizes with simulation

For the study of ultra-low dose CT based PET attenuation correction, the simulation results presented show a general trend: we can reduce the radiation dose roughly by an order of magnitude compared to the current techniques. One limitation in the presented work is that simulations were performed with only fixed phantom size, either 30 cm × 20 cm elliptical water cylinder or NCAT phantom with a typical adult size. In reality, however, radiation dose is patient size dependent, thus the exact reduced dose is also patient size dependent. It is believed that the general trend (relative dose reduction factor) by our techniques would not change too much no matter what size the patient would be. However, for a comprehensive study, one potential future direction is to evaluate standard CT dose reduction techniques for a series of phantom sizes with simulation.

7.2.4 Development of more advanced dose minimization and noise suppression strategies

The presented work for ultra-low dose study explored some of the simplest strategies for dose reduction to take advantage of the reduced requirements of CTAC for PET. There are other simple dose reduced acquisition methods besides those studied here, for example: collimation, X-ray tube pulsing, short scan with gating or fixed shielding (Xia *et al.*, 2012; Xia *et al.*, 2010b).

For noise reduction, simple boxcar smoothing and adaptive trimmed mean filter were used in this thesis for CT sinogram noise and artifacts reduction. However, the initial results also suggest that further improvements

may be possible with more sophisticated smoothing algorithms.

In addition, we may investigate some other methods, such as combined detector elements, , iterative CT reconstruction (De Man *et al.*, 2001), or compressed sensing (Chen *et al.*, 2008).

7.2.5 Design practical protocols enabling low dose longer duration CT scans for quantitative PET imaging

An exciting future direction is to apply the presented work for practical protocol design. For example, it is desirable to design protocols of longer duration CT scans for respiratory-gated CT to be phase matching with PET for attenuation correction and motion estimation, and radiation dose reduced dual energy CT with improved quantitation for PET imaging of bone cancer.

Bibliography

- Abdelnour A F, Nehmeh S A, Pan T, Humm J L, Vernon P, Schoder H, Rosenzweig K E, Mageras G S, Yorke E, Larson S M and Erdi Y E 2007 Phase and amplitude binning for 4D-CT imaging *Phys Med Biol* **52** 3515-29
- Abella M, Alessio A M, Mankoff D A, MacDonald L R, Vaquero J J, Desco M and Kinahan P E 2012 Accuracy of CT-based attenuation correction in PET/CT bone imaging *Phys Med Biol* **57** 2477-90
- Adams S, Baum R P, Stuckensen T, Bitter K and Hor G 1998 Prospective comparison of 18F-FDG PET with conventional imaging modalities (CT, MRI, US) in lymph node staging of head and neck cancer *Eur J Nucl Med* **25** 1255-60
- Alessio A M and Kinahan P E 2006 Improved quantitation for PET/CT image reconstruction with system modeling and anatomical priors *Med Phys* **33** 4095-103
- Alessio A M, Kinahan P E, Cheng P M, Vesselle H and Karp J S 2004 PET/CT scanner instrumentation, challenges, and solutions *Radiol Clin North Am* **42** 1017-32, vii
- Alexieva-Figusch J, Van Putten W L, Blankenstein M A, Blonk-Van Der Wijst J and Klijn J G 1988 The prognostic value and relationships of patient characteristics, estrogen and progesterin receptors, and site of relapse in primary breast cancer *Cancer* **61** 758-68
- Alles J and Mudde R F 2007 Beam hardening: analytical considerations of the effective attenuation coefficient of X-ray tomography *Med Phys* **34** 2882-9
- Alvarez R and Seppi E 1979 Comparison of Noise and Dose in Conventional and Energy Selective Computed-Tomography *Ieee T Nucl Sci* **26** 2853-5
- Alvarez R E and Macovski A 1976 Energy-Selective Reconstructions in X-Ray Computerized Tomography *Physics in Medicine and Biology* **21** 733-44
- Antoch G, Jentzen W, Freudenberg L S, Stattaus J, Mueller S P, Debatin J F and Bockisch A 2003 Effect of oral contrast agents on computed tomography-based positron emission tomography attenuation correction in dual-modality positron emission tomography/computed tomography imaging *Invest Radiol* **38** 784-9
- Bai C, Kinahan P E, Brasse D, Comtat C, Townsend D W, Meltzer C C, Villemagne V, Charron M and Defrise M 2003a An analytic study of the effects of attenuation on tumor detection in whole-body PET oncology imaging *J Nucl Med* **44** 1855-61
- Bai C Y, Shao L, Da Silva A J and Zhao Z 2003b A generalized model for the conversion from CT numbers to linear attenuation coefficients *Ieee T*

Nucl Sci **50** 1510-5

- Becker K, Mueller J D, Schulmacher C, Ott K, Fink U, Busch R, Bottcher K, Siewert J R and Hofler H 2003 Histomorphology and grading of regression in gastric carcinoma treated with neoadjuvant chemotherapy *Cancer* **98** 1521-30
- Beissert M, Lorenz R and Gerharz E W 2008 [Rational imaging in locally advanced prostate cancer] *Urologe A* **47** 1405-16
- Beyer T, Townsend D W and Blodgett T M 2002 Dual-modality PET/CT tomography for clinical oncology *Quarterly Journal of Nuclear Medicine* **46** 24-34
- Beyer T, Townsend D W, Brun T, Kinahan P E, Charron M, Roddy R, Jerin J, Young J, Byars L and Nutt R 2000a A combined PET/CT scanner for clinical oncology *Journal of Nuclear Medicine* **41** 1369-79
- Beyer T, Townsend D W, Brun T, Kinahan P E, Charron M, Roddy R, Jerin J, Young J, Byars L and Nutt R 2000b A combined PET/CT scanner for clinical oncology *J Nucl Med* **41** 1369-79
- Bhosale P and Iyer R 2008 Diagnostic imaging in gynecologic malignancy *Minerva Ginecol* **60** 143-54
- Birch R and Marshall M 1979 Computation of bremsstrahlung X-ray spectra and comparison with spectra measured with a Ge(Li) detector *Phys Med Biol* **24** 505-17
- Blankespoor S C, Wu X, Kalki K, Brown J K, Tang H R, Cann C E and Hasegawa B H 1996 Attenuation correction of SPECT using X-ray CT on an emission-transmission CT system: Myocardial perfusion assessment *IEEE T Nucl Sci* **43** 2263-74
- Boone J M, Nelson T R, Lindfors K K and Seibert J A 2001 Dedicated breast CT: radiation dose and image quality evaluation *Radiology* **221** 657-67
- Brenner D J and Hall E J 2007 Computed tomography--an increasing source of radiation exposure *N Engl J Med* **357** 2277-84
- Brix G, Lechel U, Glatting G, Ziegler S I, Munzing W, Muller S P and Beyer T 2005 Radiation exposure of patients undergoing whole-body dual-modality 18F-FDG PET/CT examinations *J Nucl Med* **46** 608-13
- Brooks R A and Di Chiro G 1976 Beam hardening in x-ray reconstructive tomography *Phys Med Biol* **21** 390-8
- Bujenovic S, Mannting F, Chakrabarti R and Ladnier D 2003 Artfactual 2-deoxy-2-[(18)F]fluoro-D-glucose localization surrounding metallic objects in a PET/CT scanner using CT-based attenuation correction *Mol Imaging Biol* **5** 20-2
- Bunyaviroch T and Coleman R E 2006 PET evaluation of lung cancer *J Nucl Med* **47** 451-69
- Burger C, Goerres G, Schoenes S, Buck A, Lonn A H and Von Schulthess G

- K 2002a PET attenuation coefficients from CT images: experimental evaluation of the transformation of CT into PET 511-keV attenuation coefficients *Eur J Nucl Med Mol Imaging* **29** 922-7
- Burger C, Goerres G, Schoenes S, Buck A, Lonn A H R and von Schulthess G K 2002b PET attenuation coefficients from CT images: experimental evaluation of the transformation of CT into PET 511-keV attenuation coefficients *Eur J Nucl Med Mol I* **29** 922-7
- Bushberg J T 2002 *The essential physics of medical imaging* (Philadelphia: Lippincott Williams & Wilkins)
- Buzug T M 2008 *Computed Tomography: From Photon Statistics to Modern Cone-Beam CT*: Springer-Verlag Berlin Heidelberg)
- Chacko T K, Zhuang H, Stevenson K, Moussavian B and Alavi A 2002 The importance of the location of fluorodeoxyglucose uptake in periprosthetic infection in painful hip prostheses *Nucl Med Commun* **23** 851-5
- Charron M, Beyer T, Bohnen N N, Kinahan P E, Dachille M, Jerin J, Nutt R, Meltzer C C, Villemagne V and Townsend D W 2000 Image analysis in patients with cancer studied with a combined PET and CT scanner *Clinical Nuclear Medicine* **25** 905-10
- Chen G H, Tang J and Leng S 2008 Prior image constrained compressed sensing (PICCS): a method to accurately reconstruct dynamic CT images from highly undersampled projection data sets *Med Phys* **35** 660-3
- Cherry S R, Sorenson J A and Phelps M E 2003 *Physics in nuclear medicine* (Philadelphia, Pa.: Saunders)
- Chi P C, Mawlawi O, Nehmeh S A, Erdi Y E, Balter P A, Luo D, Mohan R and Pan T 2007 Design of respiration averaged CT for attenuation correction of the PET data from PET/CT *Med Phys* **34** 2039-47
- Chuang K S and Huang H K 1988 Comparison of four dual energy image decomposition methods *Phys Med Biol* **33** 455-66
- Clamp A, Danson S, Nguyen H, Cole D and Clemons M 2004 Assessment of therapeutic response in patients with metastatic bone disease *Lancet Oncol* **5** 607-16
- Cohade C, Osman M, Nakamoto Y, Marshall L T, Links J M, Fishman E K and Wahl R L 2003 Initial experience with oral contrast in PET/CT: phantom and clinical studies *J Nucl Med* **44** 412-6
- Coleman R E and Rubens R D 1987 The clinical course of bone metastases from breast cancer *Br J Cancer* **55** 61-6
- Colsher J G, Jiang H, Thibault J-B, Lonn A, Pan T, Lokitz S J and Turkington T G 2008 Ultra low dose CT for attenuation correction in PET/CT. In: *Nuclear Science Symposium Conference Record, 2008. NSS '08. IEEE: Proc. of IEEE*) pp 5506-11

- Comtat C, Kinahan P E, Defrise M, Michel C, Lartzien C and Townsend D W 1999 Simulating whole-body PET scanning with rapid analytical methods. In: *IEEE Nuclear Science Symposium and Medical Imaging Conference*, (Seattle, WA: Proc. of IEEE) pp 1260-4
- Crotty D J, McKinley R L and Tornai M P 2007 Experimental spectral measurements of heavy K-edge filtered beams for x-ray computed mammotomography *Phys Med Biol* **52** 603-16
- Czernin J, Allen-Auerbach M and Schelbert H R 2007 Improvements in cancer staging with PET/CT: literature-based evidence as of September 2006 *J Nucl Med* **48 Suppl 1** 78S-88S
- Dawood M, Buther F, Lang N, Schober O and Schafers K P 2007 Respiratory gating in positron emission tomography: a quantitative comparison of different gating schemes *Med Phys* **34** 3067-76
- Dawood M, Lang N, Jiang X and Schafers K P 2006 Lung motion correction on respiratory gated 3-D PET/CT images *IEEE Trans Med Imaging* **25** 476-85
- De Man B, Basu S, Chandra N, Dunham B, Edic P, Iatrou M, Mcolash S, Sainath P, Shaughnessy C, Tower B and Williams E 2007 CATSIM : a new Computer Assisted Tomography SIMulation environment. In: *Medical Imaging 2007: Physics of Medical Imaging*, ed J Hsieh and J Flynn: Proc. of SPIE) p 65102G
- De Man B, Nuyts J, Dupont P, Marchal G and Suetens P 2001 An iterative maximum-likelihood polychromatic algorithm for CT *IEEE Trans Med Imaging* **20** 999-1008
- De Visschere P, Oosterlinck W, De Meerleer G and Villeirs G 2010 Clinical and imaging tools in the early diagnosis of prostate cancer, a review *JBR-BTR* **93** 62-70
- Deloar H M, Fujiwara T, Shidahara M, Nakamura T, Watabe H, Narita Y, Itoh M, Miyake M and Watanuki S 1998 Estimation of absorbed dose for 2-[F-18]fluoro-2-deoxy-D-glucose using whole-body positron emission tomography and magnetic resonance imaging *Eur J Nucl Med* **25** 565-74
- DeMarco J J, Cagnon C H, Cody D D, Stevens D M, McCollough C H, Zankl M, Angel E and McNitt-Gray M F 2007 Estimating radiation doses from multidetector CT using Monte Carlo simulations: effects of different size voxelized patient models on magnitudes of organ and effective dose *Phys Med Biol* **52** 2583-97
- Dizendorf E, Hany T F, Buck A, von Schulthess G K and Burger C 2003 Cause and magnitude of the error induced by oral CT contrast agent in CT-based attenuation correction of PET emission studies *J Nucl Med* **44** 732-8
- Doost-Hoseini A M 1984 Signal processing in Dual Energy Computed Tomography (Beam Filter). In: *Electrical Engineering*: Stanford

University)

- Doot R K 2008 Factors affecting quantitative PET as a measure of cancer response to therapy. University of Washington, 2008.) pp viii, 139 leaves
- Eisenhauer E A, Therasse P, Bogaerts J, Schwartz L H, Sargent D, Ford R, Dancey J, Arbuck S, Gwyther S, Mooney M, Rubinstein L, Shankar L, Dodd L, Kaplan R, Lacombe D and Verweij J 2009 New response evaluation criteria in solid tumours: revised RECIST guideline (version 1.1) *Eur J Cancer* **45** 228-47
- Endo M, Tsunoo T, Nakamori N and Yoshida K 2001 Effect of scattered radiation on image noise in cone beam CT *Med Phys* **28** 469-74
- Flynn M J and Samei E 1999 Experimental comparison of noise and resolution for 2k and 4k storage phosphor radiography systems *Med Phys* **26** 1612-23
- Gingold E L and Hasegawa B H 1992 Systematic bias in basis material decomposition applied to quantitative dual-energy x-ray imaging *Med Phys* **19** 25-33
- Glover G H 1982 Compton Scatter Effects in Ct Reconstructions *Med Phys* **9** 860-7
- Goerres G W, Burger C, Kamel E, Seifert B, Kaim A H, Buck A, Buehler T C and Von Schulthess G K 2003a Respiration-induced attenuation artifact at PET/CT: technical considerations *Radiology* **226** 906-10
- Goerres G W, Ziegler S I, Burger C, Berthold T, Von Schulthess G K and Buck A 2003b Artifacts at PET and PET/CT caused by metallic hip prosthetic material *Radiology* **226** 577-84
- Goh K L, Liew S C and Hasegawa B H 1997 Correction of energy-dependent systematic errors in dual-energy x-ray CT using a basis material coefficients transformation method *Ieee T Nucl Sci* **44** 2419-24
- Greenfield M A 1992 Current status of physical measurements of the skeleton *Med Phys* **19** 1349-57
- Guckenberger M, Weininger M, Wilbert J, Richter A, Baier K, Krieger T, Polat B and Flentje M 2007 Influence of retrospective sorting on image quality in respiratory correlated computed tomography *Radiother Oncol* **85** 223-31
- Guy M J, Castellano-Smith I A, Flower M A, Flux G D, Ott R J and Visvikis D 1998 DETECT - Dual energy transmission estimation CT - for improved attenuation correction in SPECT and PET *Ieee T Nucl Sci* **45** 1261-7
- Halpern B S, Dahlbom M, Quon A, Schiepers C, Waldherr C, Silverman D H, Ratib O and Czernin J 2004 Impact of patient weight and emission scan duration on PET/CT image quality and lesion detectability *J Nucl Med* **45** 797-801
- Hanbidge A E 2002 Cancer of the pancreas: the best image for early

- detection--CT, MRI, PET or US? *Can J Gastroenterol* **16** 101-5
- Harewood G C and Wiersema M J 2002 A cost analysis of endoscopic ultrasound in the evaluation of esophageal cancer *Am J Gastroenterol* **97** 452-8
- Hasegawa B H, Lang T F, Brown J K, Gingold E L, Reilly S M, Blankespoor S C, Liew S C, Tsui B M W and Ramanathan C 1993 Object-Specific Attenuation Correction of Spect with Correlated Dual-Energy X-Ray Ct *IEEE T Nucl Sci* **40** 1242-52
- Hays M T, Watson E E, Thomas S R and Stabin M 2002 MIRD dose estimate report no. 19: radiation absorbed dose estimates from (18)F-FDG *J Nucl Med* **43** 210-4
- Herrmann K, Krause B J, Bundschuh R A, Dechow T and Schwaiger M 2009 Monitoring response to therapeutic interventions in patients with cancer *Semin Nucl Med* **39** 210-32
- Heusner T A, Kuemmel S, Umutlu L, Koeninger A, Freudenberg L S, Hauth E A, Kimmig K R, Forsting M, Bockisch A and Antoch G 2008 Breast cancer staging in a single session: whole-body PET/CT mammography *J Nucl Med* **49** 1215-22
- Hoekstra C J, Stroobants S G, Smit E F, Vansteenkiste J, van Tinteren H, Postmus P E, Golding R P, Biesma B, Schramel F J, van Zandwijk N, Lammertsma A A and Hoekstra O S 2005 Prognostic relevance of response evaluation using [18F]-2-fluoro-2-deoxy-D-glucose positron emission tomography in patients with locally advanced non-small-cell lung cancer *J Clin Oncol* **23** 8362-70
- Hoffman E J, Huang S C, Phelps M E and Kuhl D E 1981 Quantitation in Positron Emission Computed-Tomography .4. Effect of Accidental Coincidences *J Comput Assist Tomo* **5** 391-400
- Houssami N, Irwig L and Ung O 2005 Review of complex breast cysts: implications for cancer detection and clinical practice *ANZ J Surg* **75** 1080-5
- Houston S J and Rubens R D 1995 The systemic treatment of bone metastases *Clin Orthop Relat Res* 95-104
- Hsiao I T and Gindi G 2002 Noise propagation from attenuation correction into PET reconstructions *IEEE T Nucl Sci* **49** 90-7
- Hsieh J 1998 Adaptive streak artifact reduction in computed tomography resulting from excessive x-ray photon noise *Med Phys* **25** 2139-47
- Hsieh J 2009 *Computed tomography : principles, design, artifacts, and recent advances* (Bellingham, Wash., Hoboken, N.J.: SPIE ; J. Wiley & Sons)
- Hsieh J, Gurmen O E and King K F 2000 Investigation of a solid-state detector for advanced computed tomography *IEEE Trans Med Imaging* **19** 930-40
- ICRP 1998 Radiation Dose to Patients from Radiopharmaceuticals. In:

- Publication 80*, (New York: International Commission on Radiological Protection)
- ICRP 2007 The 2007 Recommendations of the International Commission on Radiological Protection. ICRP publication 103 *Ann ICRP* **37** 1-332
- Iyer V R and Lee S I 2010 MRI, CT, and PET/CT for ovarian cancer detection and adnexal lesion characterization *AJR Am J Roentgenol* **194** 311-21
- Jensen J A 2007 Medical ultrasound imaging *Prog Biophys Mol Biol* **93** 153-65
- Kachelriess M, Watzke O and Kalender W A 2001 Generalized multi-dimensional adaptive filtering for conventional and spiral single-slice, multi-slice, and cone-beam CT *Med Phys* **28** 475-90
- Kalender A W ed 2000 *Computed Tomography: Fundamentals, System Technology, Image Quality, Applications*: Wiley-VCH)
- Kamby C, Rasmussen B B and Kristensen B 1991 Prognostic indicators of metastatic bone disease in human breast cancer *Cancer* **68** 2045-50
- Kamel E, Hany T F, Burger C, Treyer V, Lonn A H R, von Schulthess G K and Buck A 2002 CT vs Ge-68 attenuation correction in a combined PET/CT system: evaluation of the effect of lowering the CT tube current *Eur J Nucl Med Mol I* **29** 346-50
- Kawano T, Ohtake E and Inoue T 2008 Deep-inspiration breath-hold PET/CT of lung cancer: maximum standardized uptake value analysis of 108 patients *J Nucl Med* **49** 1223-31
- Keter D and Melzer E 2008 Endoscopic ultrasound in clinical practice *Acta Gastroenterol Latinoam* **38** 146-51
- Kherlopian A R, Song T, Duan Q, Neimark M A, Po M J, Gohagan J K and Laine A F 2008 A review of imaging techniques for systems biology *BMC Syst Biol* **2** 74
- Kim J H, Czernin J, Allen-Auerbach M S, Halpern B S, Fueger B J, Hecht J R, Ratib O, Phelps M E and Weber W A 2005 Comparison between 18F-FDG PET, in-line PET/CT, and software fusion for restaging of recurrent colorectal cancer *J Nucl Med* **46** 587-95
- Kim J W and Dang C V 2006 Cancer's molecular sweet tooth and the Warburg effect *Cancer Res* **66** 8927-30
- Kinahan P E, Alessio A M and Fessler J A 2006a Dual energy CT attenuation correction methods for quantitative assessment of response to cancer therapy with PET/CT imaging *Technol Cancer Res Treat* **5** 319-27
- Kinahan P E, Hasegawa B H and Beyer T 2003 X-ray-based attenuation correction for positron emission tomography/computed tomography scanners *Semin Nucl Med* **33** 166-79
- Kinahan P E, MacDonald L, Ng L, Alessio A, Segars P, Tsui B M W and Pathak S D 2006b Compensating for patient respiration in PET/CT

- imaging with the registered and summed phases (PASP) procedure. In: *3rd IEEE International Symposium on Biomedical Imaging: Nano to Macro*, pp 1104-7
- Kinahan P E, Townsend D W, Beyer T and Sashin D 1998 Attenuation correction for a combined 3D PET/CT scanner *Med Phys* **25** 2046-53
- Krestel E 1990 *Imaging systems for medical diagnostics : fundamentals and technical solutions : X-ray diagnostics, computed tomography, nuclear medical diagnostics, magnetic resonance imaging, sonography, biomagnetic diagnostics* (Berlin: Siemens Aktiengesellschaft)
- Kusaba H and Saijo N 2000 [A summary report of response evaluation criteria in solid tumors (RECIST criteria)] *Gan To Kagaku Ryoho* **27** 1-5
- La Riviere P J 2005 Penalized-likelihood sinogram smoothing for low-dose CT *Med Phys* **32** 1676-83
- La Riviere P J, Bian J and Vargas P A 2006 Penalized-likelihood sinogram restoration for computed tomography *IEEE Trans Med Imaging* **25** 1022-36
- Lacroix K J, Tsui B M W, Hasegawa B H and Brown J K 1994 Investigation of the Use of X-Ray Ct Images for Attenuation Compensation in Spect *IEEE T Nucl Sci* **41** 2793-9
- Lamare F, Ledesma Carbayo M J, Cresson T, Kontaxakis G, Santos A, Le Rest C C, Reader A J and Visvikis D 2007 List-mode-based reconstruction for respiratory motion correction in PET using non-rigid body transformations *Phys Med Biol* **52** 5187-204
- Legmann P, Vignaux O, Dousset B, Baraza A J, Palazzo L, Dumontier I, Coste J, Louvel A, Roseau G, Couturier D and Bonnin A 1998 Pancreatic tumors: comparison of dual-phase helical CT and endoscopic sonography *AJR Am J Roentgenol* **170** 1315-22
- Lehmann L A, Alvarez R E, Macovski A, Brody W R, Pelc N J, Riederer S J and Hall A L 1981 Generalized image combinations in dual KVP digital radiography *Med Phys* **8** 659-67
- Li T, Thorndyke B, Schreiber E, Yang Y and Xing L 2006 Model-based image reconstruction for four-dimensional PET *Med Phys* **33** 1288-98
- Liu C, Pierce L A, 2nd, Alessio A M and Kinahan P E 2009 The impact of respiratory motion on tumor quantification and delineation in static PET/CT imaging *Phys Med Biol* **54** 7345-62
- Loveday E J, Bleach N R, Van Hasselt C A and Metreweli C 1994 Ultrasound imaging in laryngeal cancer: a preliminary study *Clin Radiol* **49** 676-82
- Mandard A M, Dalibard F, Mandard J C, Marnay J, Henry-Amar M, Petiot J F, Roussel A, Jacob J H, Segol P, Samama G and et al. 1994 Pathologic assessment of tumor regression after preoperative chemoradiotherapy of esophageal carcinoma. Clinicopathologic correlations *Cancer* **73** 2680-6

- McNitt-Gray M F 2002 AAPM/RSNA physics tutorial for residents: Topics in CT - Radiation dose in CT1 *Radiographics* **22** 1541-53
- Messa C, Bettinardi V, Picchio M, Pelosi E, Landoni C, Gianolli L, Gilardi M C and Fazio F 2004 PET/CT in diagnostic oncology *Quarterly Journal of Nuclear Medicine and Molecular Imaging* **48** 66-75
- Mettler F A, Jr., Thomadsen B R, Bhargavan M, Gilley D B, Gray J E, Lipoti J A, McCrohan J, Yoshizumi T T and Mahesh M 2008 Medical radiation exposure in the U.S. in 2006: preliminary results *Health Phys* **95** 502-7
- Miura F, Takada T, Amano H, Yoshida M, Furui S and Takeshita K 2006 Diagnosis of pancreatic cancer *HPB (Oxford)* **8** 337-42
- Muller M F, Meyenberger C, Bertschinger P, Schaer R and Marincek B 1994 Pancreatic tumors: evaluation with endoscopic US, CT, and MR imaging *Radiology* **190** 745-51
- Nakamoto Y, Chin B B, Kraitchman D L, Lawler L P, Marshall L T and Wahl R L 2003 Effects of nonionic intravenous contrast agents at PET/CT imaging: phantom and canine studies *Radiology* **227** 817-24
- Nakamoto Y, Osman M, Cohade C, Marshall L T, Links J M, Kohlmyer S and Wahl R L 2002 PET/CT: comparison of quantitative tracer uptake between germanium and CT transmission attenuation-corrected images *J Nucl Med* **43** 1137-43
- NCRP 2009 NCRP Report No. 160: Ionizing Radiation Exposure of the Population of the United States. PMID: 19690356) p 465
- Nehmeh S A and Erdi Y E 2008 Respiratory motion in positron emission tomography/computed tomography: a review *Semin Nucl Med* **38** 167-76
- Nehmeh S A, Erdi Y E, Kalaigian H, Kolbert K S, Pan T S, Yeung H, Squire O, Sinha A, Larson S M and Humm J L 2003 Correction for oral contrast artifacts in CT attenuation-corrected PET images obtained by combined PET/CT *Journal of Nuclear Medicine* **44** 1940-4
- Nehmeh S A, Erdi Y E, Meirelles G S, Squire O, Larson S M, Humm J L and Schoder H 2007 Deep-inspiration breath-hold PET/CT of the thorax *J Nucl Med* **48** 22-6
- Nehmeh S A, Erdi Y E, Pan T, Pevsner A, Rosenzweig K E, Yorke E, Mageras G S, Schoder H, Vernon P, Squire O, Mostafavi H, Larson S M and Humm J L 2004a Four-dimensional (4D) PET/CT imaging of the thorax *Med Phys* **31** 3179-86
- Nehmeh S A, Erdi Y E, Pan T, Yorke E, Mageras G S, Rosenzweig K E, Schoder H, Mostafavi H, Squire O, Pevsner A, Larson S M and Humm J L 2004b Quantitation of respiratory motion during 4D-PET/CT acquisition *Med Phys* **31** 1333-8
- Nelson D L, Cox M M and Lehninger A L 2000 *principles of biochemistry* (New York: Worth Publishers)

- Nielsen O S, Munro A J and Tannock I F 1991 Bone metastases: pathophysiology and management policy *J Clin Oncol* **9** 509-24
- Ning R, Chen B, Yu R, Conover D, Tang X and Ning Y 2000 Flat panel detector-based cone-beam volume CT angiography imaging: system evaluation *IEEE Trans Med Imaging* **19** 949-63
- Noh J, Fessler J A and Kinahan P E 2009 Statistical sinogram restoration in dual-energy CT for PET attenuation correction *IEEE Trans Med Imaging* **28** 1688-702
- Padhani A R 2002 Dynamic contrast-enhanced MRI in clinical oncology: current status and future directions *J Magn Reson Imaging* **16** 407-22
- Pan L, Han Y, Sun X, Liu J and Gang H 2010 FDG-PET and other imaging modalities for the evaluation of breast cancer recurrence and metastases: a meta-analysis *J Cancer Res Clin Oncol* **136** 1007-22
- Pan T, Lee T Y, Rietzel E and Chen G T 2004 4D-CT imaging of a volume influenced by respiratory motion on multi-slice CT *Med Phys* **31** 333-40
- Pan T, Mawlawi O, Luo D, Liu H H, Chi P C, Mar M V, Gladish G, Truong M, Erasmus J, Jr., Liao Z and Macapinlac H A 2006 Attenuation correction of PET cardiac data with low-dose average CT in PET/CT *Med Phys* **33** 3931-8
- Pan T, Sun X and Luo D 2007 Improvement of the cine-CT based 4D-CT imaging *Med Phys* **34** 4499-503
- Park S J, Ionascu D, Killoran J, Mamede M, Gerbaudo V H, Chin L and Berbeco R 2008 Evaluation of the combined effects of target size, respiratory motion and background activity on 3D and 4D PET/CT images *Phys Med Biol* **53** 3661-79
- Pevsner A, Nehmeh S A, Humm J L, Mageras G S and Erdi Y E 2005 Effect of motion on tracer activity determination in CT attenuation corrected PET images: a lung phantom study *Med Phys* **32** 2358-62
- Pfau P R, Ginsberg G G, Lew R J, Brensinger C M and Kochman M L 2001 EUS predictors of long-term survival in esophageal carcinoma *Gastrointest Endosc* **53** 463-9
- Phelps M E 2006 *PET : physics, instrumentation, and scanners* (New York ; Berlin: Springer)
- Phelps M E, Hoffman E J, Mullani N A and Ter-Pogossian M M 1975 Application of annihilation coincidence detection to transaxial reconstruction tomography *J Nucl Med* **16** 210-24
- Poludniowski G, Landry G, DeBlois F, Evans P M and Verhaegen F 2009 SpekCalc: a program to calculate photon spectra from tungsten anode x-ray tubes *Phys Med Biol* **54** N433-8
- Poludniowski G G 2007 Calculation of x-ray spectra emerging from an x-ray tube. Part II. X-ray production and filtration in x-ray targets *Med Phys* **34** 2175-86

- Powles T, Murray I, Brock C, Oliver T and Avril N 2007 Molecular positron emission tomography and PET/CT imaging in urological malignancies *Eur Urol* **51** 1511-20; discussion 20-1
- Qi J and Huesman R H 2005 Effect of errors in the system matrix on maximum a posteriori image reconstruction *Phys Med Biol* **50** 3297-312
- Qiao F, Pan T, Clark J W, Jr. and Mawlawi O 2007 Joint model of motion and anatomy for PET image reconstruction *Med Phys* **34** 4626-39
- Qiao F, Pan T, Clark J W, Jr. and Mawlawi O R 2006 A motion-incorporated reconstruction method for gated PET studies *Phys Med Biol* **51** 3769-83
- Rahmim A and Zaidi H 2008 PET versus SPECT: strengths, limitations and challenges *Nucl Med Commun* **29** 193-207
- Robinson P J and Kreel L 1979 Pulmonary Tissue Attenuation with Computed-Tomography - Comparison of Inspiration and Expiration Scans *J Comput Assist Tomo* **3** 740-8
- Rosch T 1995 Endosonographic staging of esophageal cancer: a review of literature results *Gastrointest Endosc Clin N Am* **5** 537-47
- Saha G B 2006 *Physics and radiobiology of nuclear medicine* (New York: Springer)
- Samei E and Flynn M J 2003 An experimental comparison of detector performance for direct and indirect digital radiography systems *Med Phys* **30** 608-22
- Schirrmeister H, Guhlmann A, Kotzerke J, Santjohanser C, Kuhn T, Kreienberg R, Messer P, Nussle K, Elsner K, Glatting G, Trager H, Neumaier B, Diederichs C and Reske S N 1999 Early detection and accurate description of extent of metastatic bone disease in breast cancer with fluoride ion and positron emission tomography *J Clin Oncol* **17** 2381-9
- Schneider W, Bortfeld T and Schlegel W 2000 Correlation between CT numbers and tissue parameters needed for Monte Carlo simulations of clinical dose distributions *Phys Med Biol* **45** 459-78
- Segars W P 2001 Development of a new dynamic NURBS-based cardiac torso (NCAT) phantom. The University of North Carolina)
- Segars W P, Mahesh M, Beck T J, Frey E C and Tsui B M W 2008 Realistic CT simulation using the 4D XCAT phantom *Med Phys* **35** 3800-8
- Shah S K and Greatrex K V 2005 Current role of magnetic resonance imaging in breast imaging: a primer for the primary care physician *J Am Board Fam Pract* **18** 478-90
- Siewerdsen J H and Jaffray D A 2001 Cone-beam computed tomography with a flat-panel imager: magnitude and effects of x-ray scatter *Med Phys* **28** 220-31

- Stafford S E, Gralow J R, Schubert E K, Rinn K J, Dunnwald L K, Livingston R B and Mankoff D A 2002 Use of serial FDG PET to measure the response of bone-dominant breast cancer to therapy *Acad Radiol* **9** 913-21
- Storm E 1972a Calculated Bremsstrahlung Spectra from Thick Tungsten Targets *Phys Rev A* **5** 2328-&
- Storm E 1972b Emission of Characteristic L and K Radiation from Thick Tungsten Targets *J Appl Phys* **43** 2790-&
- Tagliabue L and Schillaci O 2007 SPECT/CT in oncology: the fusion of two imaging modalities is a new standard of care *Q J Nucl Med Mol Imaging* **51** 285-9
- Thielemans K, Manjeshwar R M, Xiaodong T and Asma E 2006 Lesion detectability in motion compensated image reconstruction of respiratory gated PET/CT. In: *Nuclear Science Symposium Conference Record, 2006. IEEE*, pp 3278-82
- Tong S, Alessio A M and Kinahan P E 2010a Image reconstruction for PET/CT scanners: past achievements and future challenges *Imaging Med* **2** 529-45
- Tong S, Alessio A M and Kinahan P E 2010b Noise and signal properties in PSF-based fully 3D PET image reconstruction: an experimental evaluation *Phys Med Biol* **55** 1453-73
- Turner A C, Zhang D, Khatonabadi M, Zankl M, DeMarco J J, Cagnon C H, Cody D D, Stevens D M, McCollough C H and McNitt-Gray M F 2011 The feasibility of patient size-corrected, scanner-independent organ dose estimates for abdominal CT exams *Med Phys* **38** 820-9
- van den Brekel M W 2000 Lymph node metastases: CT and MRI *Eur J Radiol* **33** 230-8
- Visvikis D, Costa D C, Croasdale I, Lonn A H, Bomanji J, Gacinovic S and Ell P J 2003 CT-based attenuation correction in the calculation of semi-quantitative indices of [18F]FDG uptake in PET *Eur J Nucl Med Mol Imaging* **30** 344-53
- Wahl R L, Jacene H, Kasamon Y and Lodge M A 2009 From RECIST to PERCIST: Evolving Considerations for PET response criteria in solid tumors *J Nucl Med* **50 Suppl 1** 122S-50S
- Walker A J, Spier B J, Perlman S B, Stangl J R, Frick T J, Gopal D V, Lindstrom M J, Weigel T L and Pfau P R 2010 Integrated PET/CT Fusion Imaging and Endoscopic Ultrasound in the Pre-operative Staging and Evaluation of Esophageal Cancer *Mol Imaging Biol*
- Wallis F and Gilbert F J 1999 Magnetic resonance imaging in oncology: an overview *J R Coll Surg Edinb* **44** 117-25
- Warburg O 1956 [Origin of cancer cells.] *Oncologia* **9** 75-83
- Watanabe H, Okada M, Kaji Y, Satouchi M, Sato Y, Yamabe Y, Onaya H,

- Endo M, Sone M and Arai Y 2009 [New response evaluation criteria in solid tumours-revised RECIST guideline (version 1.1)] *Gan To Kagaku Ryoho* **36** 2495-501
- Weber W A 2005 Use of PET for monitoring cancer therapy and for predicting outcome *Journal of Nuclear Medicine* **46** 983-95
- Weber W A 2006 Positron emission tomography as an imaging biomarker *J Clin Oncol* **24** 3282-92
- Weber W A, Avril N and Schwaiger M 1999 Relevance of positron emission tomography (PET) in oncology *Strahlenther Onkol* **175** 356-73
- Weber W A, Grosu A L and Czernin J 2008 Technology Insight: advances in molecular imaging and an appraisal of PET/CT scanning *Nat Clin Pract Oncol* **5** 160-70
- Weidenmaier W and Christ G 1985 [The effect of beam hardening on CT values] *Rofo* **143** 697-701
- Wernick M N and Aarsvold J N 2004 *Emission Tomography: The Fundamentals of PET and SPECT*: Elsevier Academic Press)
- Whiting B R, Massoumzadeh P, Earl O A, O'Sullivan J A, Snyder D L and Williamson J F 2006 Properties of preprocessed sinogram data in x-ray computed tomography *Med Phys* **33** 3290-303
- Willmann J K, Kimura R H, Deshpande N, Lutz A M, Cochran J R and Gambhir S S 2010 Targeted contrast-enhanced ultrasound imaging of tumor angiogenesis with contrast microbubbles conjugated to integrin-binding knottin peptides *J Nucl Med* **51** 433-40
- Xia T, Alessio A and Kinahan P E 2009 Limits of Ultra-Low Dose CT Attenuation Correction for PET/CT. In: *Proceedings of IEEE medical imaging conference (IEEE NSS/MIC)*, (Orlando, Florida: IEEE NSS/MIC'09) pp 3074-9
- Xia T, Alessio A and Kinahan P E 2010a Spectral Shaping for Ultra-Low Dose CT Attenuation Correction in PET/CT. In: *The First International Meeting on Image Formation in X-Ray Computed Tomography*, (Salt Lake City, Utah
- Xia T, Alessio A M and Kinahan P E 2010b Limits of Ultra-Low Dose CT Attenuation Correction for PET/CT *IEEE Nucl Sci Symp Conf Rec* **2009** 3074-9
- Xia T, Alessio A M, Man B D, Manjeshwar R, Asma E and Kinahan P E 2012 Ultra-low dose CT attenuation correction for PET/CT *Physics in Medicine and Biology* **57** 309
- Zhuang H, Chacko T K, Hickeson M, Stevenson K, Feng Q, Ponzo F, Garino J P and Alavi A 2002 Persistent non-specific FDG uptake on PET imaging following hip arthroplasty *Eur J Nucl Med Mol Imaging* **29** 1328-33
- Zhuang H, Duarte P S, Pourdehnad M, Maes A, Van Acker F, Shnier D,

Garino J P, Fitzgerald R H and Alavi A 2001 The promising role of 18F-FDG PET in detecting infected lower limb prosthesis implants *J Nucl Med* **42** 44-8

Appendix A: Calculation and generation of CT contrast agent material files

Commonly used CT contrast agent is Omnipaque300 (iohexol) diluted with varying concentrations.

Iohexol, *N,N'*-Bis(2,3 - dihydroxypropyl)- 5- [N - (2,3 - dihydroxypropyl)- acetamido] - 2,4,6 - triiodoisophthalamide, is a nonionic, water-soluble radiographic contrast medium with a molecular weight of 821.138 (C₁₉H₂₆I₃N₃O₉, iodine content 46.36%). In aqueous solution each triiodinated molecule remains undissociated. The chemical structure for iohexol is illustrated in the Figure 3.1 as shown in Chapter III.

Each 1ml of Omnipaque300 contains 647.1 mg of iohexol (300 mg organically bound iodine), 1.21 mg tromethamine ((HOCH₂)₃CNH₂, with molecular weight 121.14) and 0.1 mg edentate calcium disodium (EDTA: C₁₀H₁₂CaN₂Na₂O₈).

In order to study the CTAC of contrast at different concentration, we dilute the Omnipaque300 according to Table 3.1. For clinical CT usage, the dosage of Omnipaque300 ranges from 15g I to 60g I. The iodine concentration in the body varies with injection rate, imaging organ and renal clearance rate. Contrast enhancement appears to be greatest immediately after bolus administration (15 seconds to 120 seconds).

Table A.1 Contrast agent Omnipaque300 diluted in water solution with varying concentrations

Solution	Solution #1	Solution #2	Solution #3	Solution #4	Solution #5	Solution #6	Solution #7	Solution #8
	(pure)	(1:5)	(1:10)	(1:20)	(1:50)	(1:100)	(1:500)	(1:1000)
Iodine								
Concentration	300	60	30	15	6	3	0.6	0.3
(mg l/ml)								

For different solutions, the weight fraction of the same atomic constituent in the mixture is different. So we need to calculate the mass fraction of the respective components for each solution. The material files for the above solutions are ASCII-files and have no extension. The first line specifies the number of elemental components and the second line specifies the mass density (g/cm³), and the third line through end contain the atomic number and the mass fraction of the respective components.

As an example, we will show how we calculate the mass fraction for solution #2. The calculation for the 8 solutions is provided in matlab file as Omnipaque.m.

Solution #2 is obtained by dilute 1ml pure solution of Omnipaque300 with 4 ml pure water.

For 1 ml Omnipaque300, there are:

647.1 mg iohexol (C₁₉H₂₆I₃N₃O₉, molecular weight 821.138g/mol);

1.21 mg tromethamine (C₄H₁₁O₃N, molecular weight 121.14g/mol);

0.1 mg EDTA (C₁₀H₁₂CaN₂Na₂O₈, molecular weight 374.27g/mol)

So, in 1ml Omnipaque300, there are:

Iohexol (C₁₉H₂₆I₃N₃O₉):

$$\frac{647.1 \text{ mg / ml}}{821.138 \text{ g / mol}} = 7.8805 \times 10^{-4} \text{ mol / ml}$$

Tromethamine ($C_4H_{11}O_3N$):

$$\frac{1.21mg/ml}{121.14g/mol} = 9.9884e-6 mol/ml$$

EDTA ($C_{10}H_{12}CaN_2Na_2O_8$):

$$\frac{0.1mg}{374.27g/mol} = 2.6719e-7 mol/ml$$

Suppose the remaining components in Omnipaque300 are all water, and since the specific gravity of Omnipaque300 at 37° is 1.349, so the mass of water in the pure solution is:

$$1.349 - 0.6471 - 0.00121 - 0.0001 = 0.7006g/ml$$

So Water (H_2O):

$$\frac{0.7006g/ml}{18g/mol} = 3.8922e-2 mol/ml$$

So the mole contents of H, C, N, O, I, Ca and Na in 1ml pure solution are:

For H:

$$(7.8805e-4) \times 26 + (9.9884e-6) \times 11 + (2.6719e-7) \times 12 + (3.8922e-2) \times 2 = 9.8446e-2 mol/ml$$

For C:

$$(7.8805e-4) \times 19 + (9.9884e-6) \times 4 + (2.6719e-7) \times 10 = 1.5016e-2 mol/ml$$

For N:

$$(7.8805e-4) \times 3 + (9.9884e-6) \times 1 + (2.6719e-7) \times 2 = 2.3747e-3 mol/ml$$

For O:

$$(7.8805e - 4) \times 9 + (9.9884e - 6) \times 3 + (2.6719e - 7) \times 8 + (3.8922e - 2) \times 1 \\ = 4.6117e - 2 \text{ mol / ml}$$

For I:

$$(7.8805e - 4) \times 3 = 2.3641e - 3 \text{ mol / ml}$$

For Ca:

$$(2.6719e - 7) \times 1 = 2.6719e - 7 \text{ mol / ml}$$

For Na:

$$(2.6719e - 7) \times 2 = 5.3438e - 7 \text{ mol / ml}$$

When 1ml Omnipaque300 diluted with 4ml water, for the new solution, we have approximately:

$$\text{density} = \frac{1.349 \text{ g / ml} \times 1 \text{ ml} + 1 \text{ g / ml} \times 4 \text{ ml}}{(1 + 4) \text{ ml}} = 1.0698 \text{ g / ml}$$

and the constituent elements in the 5ml solution are

For H:

$$(9.8446e - 2 \text{ mol} + \frac{1 \text{ g / ml} \times 4 \text{ ml}}{18 \text{ g / mol}} \times 2) \times 1 \text{ g / mol} = 0.5429 \text{ g}$$

For C:

$$(1.5016e - 2 \text{ mol}) \times 12.011 \text{ g / mol} = 0.1804 \text{ g}$$

For N:

$$2.3747e - 3 \text{ mol} \times 14.00674 \text{ g / mol} = 3.3262e - 2 \text{ g}$$

For O:

$$(4.6117e - 2 \text{ mol} + \frac{1 \text{ g / ml} \times 4 \text{ ml}}{18 \text{ g / mol}} \times 1) \times 15.9994 \text{ g / mol} = 4.2933 \text{ g}$$

For I:

$$(2.3641e - 3 \text{ mol}) \times 126.9045 \text{ g / mol} = 0.3 \text{ g}$$

For Ca:

$$(2.6719e - 7 \text{ mol}) \times 40.08 \text{ g/mol} = 1.0709e - 5 \text{ g}$$

For Na:

$$(5.3438e - 7 \text{ mol}) \times 22.98977 = 1.2285e - 5 \text{ g}$$

So, the mass percentages for the constituent elements are:

H:

$$\frac{0.5429 \text{ g}}{1.349 \text{ g/ml} \times 1 \text{ ml} + 1 \text{ g/ml} \times 4 \text{ ml}} = 0.1015$$

C:

$$\frac{0.1804 \text{ g}}{1.349 \text{ g/ml} \times 1 \text{ ml} + 1 \text{ g/ml} \times 4 \text{ ml}} = 0.03372$$

N:

$$\frac{3.3262e - 2 \text{ g}}{1.349 \text{ g/ml} \times 1 \text{ ml} + 1 \text{ g/ml} \times 4 \text{ ml}} = 0.006218$$

O:

$$\frac{4.2933 \text{ g}}{1.349 \text{ g/ml} \times 1 \text{ ml} + 1 \text{ g/ml} \times 4 \text{ ml}} = 0.8024$$

I:

$$\frac{0.3 \text{ g}}{1.349 \text{ g/ml} \times 1 \text{ ml} + 1 \text{ g/ml} \times 4 \text{ ml}} = 0.05608$$

Ca:

$$\frac{1.0709e-5g}{1.349g/ml \times 1ml + 1g/ml \times 4ml} = 2.002e-6$$

Na:

$$\frac{1.2285e-5g}{1.349g/ml \times 1 + 1g/ml \times 4ml} = 2.2967e-6$$

So the material files generated with varying solution are as follows:

Calculated material component files:

1. Solution #1. (filename: Iohexol)

%%%%%%%%%

7

1.349

1 0.07299

6 0.133712

7 0.024660

8 0.546191

11 9.10807e-006

20 7.93943e-006

53 0.22243

%%%%%%%%%

2. Solution #2. (filename: iohexol_dilute_5)

%%%%%%%%%

7

1.0698

1 0.101497

6 0.033717

7 0.006218

8 0.802440

11 2.29671e-006

20 2.00203e-006

53 0.056089

%%%%%%%%%

3. Solution #3. (filename: iohexol_dilute_10)

%%%%%%%%%

7

1.0349

1 0.106144

6 0.017427

7 0.003214

8 0.844205

11 1.187083e-006

20 1.034771e-006

53 0.028990

%%%%%%%%%

4. Solution #4. (filename: iohexol_dilute_20)

%%%%%%%%
7
1.01745
1 0.108587
6 0.008863
7 0.001635
8 0.866162
11 6.037213e-007
20 5.262591e-007
53 0.014744

5. Solution #5. (filename: iohexol_dilute_50)

%%%%%%%%
7
1.00698
1 0.110093
6 0.003582
7 6.606196e-004
8 0.879701
11 2.439994e-007
20 2.126923e-007
53 0.005959

6. Solution #6. (filename: iohexol_dilute_100)

%%%%%%%%
7
1.00349
1 0.110602
6 0.001797
7 3.314586e-004
8 0.884277
11 1.224234e-007
20 1.067160e-007
53 0.002990

7. Solution #7. (filename:iohexol_dilute_500)

%%%%%%%%
7
1.000698
1 0.111012
6 3.604538e-004
7 6.647667e-005
8 0.887961
11 2.455311e-008
20 2.140275e-008
53 5.996260e-004

8. Solution #8.(filename:iohexol_dilute_1000)

%%%%%%%%
7
1.000349
1 0.111063
6 1.802898e-004
7 3.324993e-005

8 0.888423
11 1.228084e-008
20 1.070511e-008
53 2.999176e-004
%%%%%%%%%

Appendix B: Modified water-only beam hardening correction for multi-row CT detector

One of the most important CT physical effects is beam hardening, which has been reviewed in Chapter II. There are two causes for beam hardening effects: 1) X-ray beam is polychromatic; 2) Attenuation coefficient of material (μ) is energy-dependent. Beam hardening effect could induce artifacts in the reconstructed images, such as cupping, if no correction is applied. The energy composition of the beam after passing through an object of given material, e.g. water, depends on the object thickness. In other words, the linear attenuation coefficient measured for the same material varies with the object (It decreases with the increasing object thickness).

There are many sophisticated beam hardening correction algorithms. However, a simple, water-only beam hardening correction code used in CATSIM for multi-row CT detector is provided here.

Compared to the original beam hardening correction routine provided in the version of Catsim 3.20, the modified version has three major improvements

- 1) It could work for bowtie and flat filters
- 2) It enables beam hardening correction for multiple detector rows
- 3) For extreme values obtained at photon starvation case, it forces the attenuation values larger than 70 cm (bore size) water attenuation to be fixed to 70 cm water attenuation (clipped).

The following is an example showing beam hardening effect for an

elliptical water phantom of size 40 cm x 26 cm x 50 cm, if no beam hardening correction is applied.

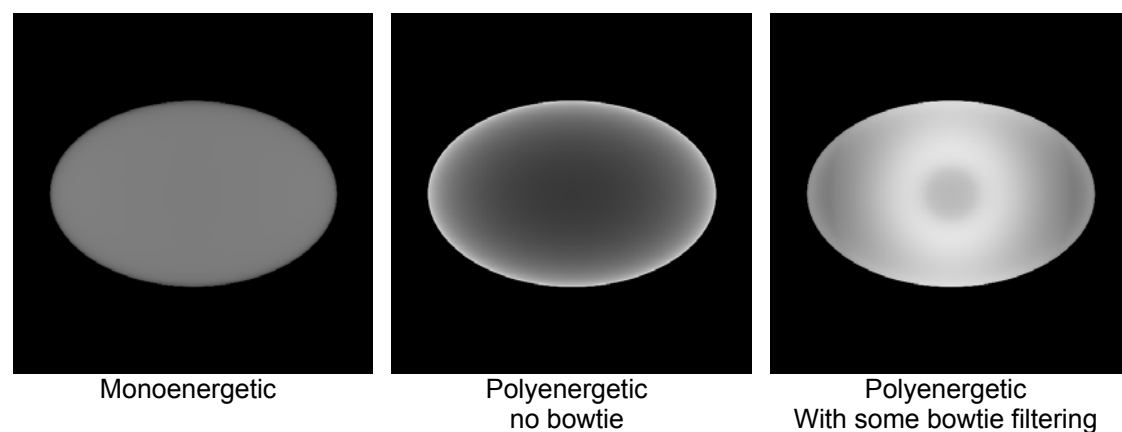


Figure B.1 Effects of CT beam hardening.

There are several observations:

- a) Bowtie filter can be used to partially correct beam hardening effects.
- b) After bowtie filter filtration, soft beams are filtered out and the averaged spectral energy is increased, so the average measured linear attenuation coefficient decreased.
- c) For different diameter phantoms with same tube voltage, the effects of beam hardening corrected by bowtie filter are related to phantom diameter, phantom location in the FOV and the shape and size of the bowtie filter used.

However, with the modified water-only beam hardening correction code developed in this study, we can see the improvements.

Beam Hardening Correction using new routine. This routine works with bowtie and flat filters.

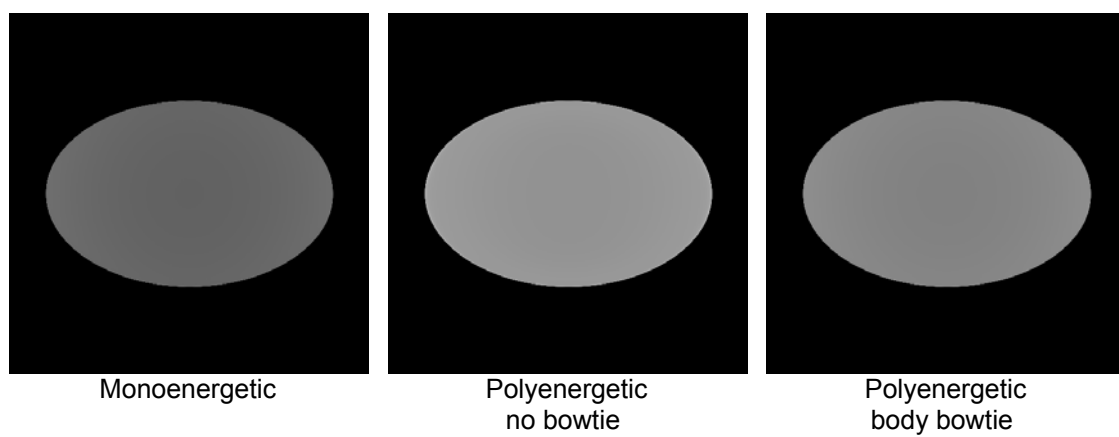


Figure B.2 Effects of CT beam hardening correction with the improved code.

Appendix C: Measured experiments on low dose CT noise characterization

From 2010 to 2012, we performed several phantom based measured experiments on GE DSTE PET/CT scanner (General Electric Healthcare, WI) at medical center in University of Washington. Those experiments were aimed to characterize the noise behavior of the CT scanner in the PET/CT system at low dose CT acquisitions.

1. *CT images acquired on DSTE PET/CT scanner for a 30 cm ×20 cm PMMA elliptical water phantom with axial scanning mode*

Techniques used

Axial mode CT acquisition on DSTE PET/CT scanner; elliptical water phantom (30 cm ×20 cm PMMA) with a 10 mm scanning length; 16 slices × 0.625 mm/slice.

For each acquisition, scan rotation time was 0.5 s. A body bowtie filter was used for data collection. Then the filtered back projection (FBP) algorithm was used for the reconstruction of the 16 CT images of size 512× 512, with slice thickness 0.625 mm each. The protocol was repeated for four different tube voltages: 80 kVp, 100 kVp, 120 kVp and 140 kVp. For each kVp scan, four tube currents were selected from the range of the highest mA the scanner could provide down to the lowest mA the scanner allows. Thus, a total of 16 acquisitions were obtained, with each acquisition containing 16 CT images with 0.625 mm slice thickness, covering 10 mm scan length.

Table C.1 Summary of axial mode CT acquisition protocols

Tube Voltage (kVp)	Tube Current (mA) (tube rotation time 0.5 s)			
	10	40	160	400
80	10	40	160	400
100	10	40	160	420
120	10	40	160	440
140	10	40	160	380

Results

We studied both image bias and noise on the reconstructed images as a function of tube current for the different tube voltages. For each reconstructed image, 18 2D ROIs with radius of 2 cm each are drawn on the 30 cm × 20 cm cross-section of the elliptical cylinder as shown in Figure 5.4. Figures C.1 and Figure C.2 show the experiment measured results in the reconstructed CT image.

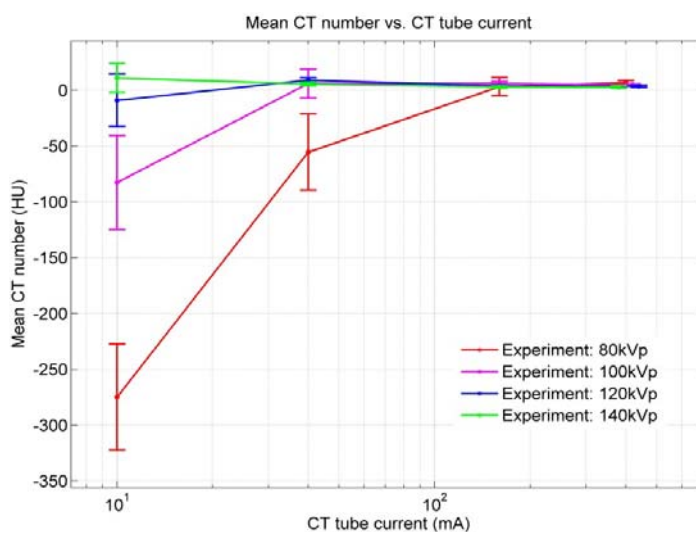


Figure C.1 For the axial mode CT acquisition, mean CT number vs. CT tube current for the selected four different CT tube voltages. The error bar at each measured data point shows the background variability.

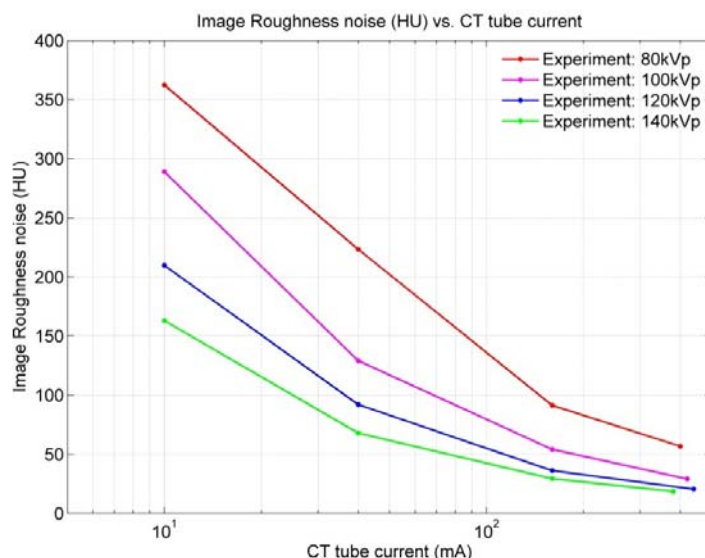


Figure C.2 CT image roughness noise as a function of the tube current for selected four different CT tube voltages. CT images are acquired using axial mode, the minimum tube current is 10 mA. Slice thickness 0.625 mm, and the tube parameters are listed in Table 1.

As expected, Figures C.1 and C.2 show that reducing tube current could increase image noise and bias.

From experiments, we notice that the detector gain may change automatically to compensate for different exposure level. **To make the detector gain fixed for analysis, it is necessary to collect data in service mode.**

2. *CT image reconstructed with data collected in service mode with fixed gain*

Techniques used

DSTE PET/CT scanner; elliptical water phantom (30 cm × 20 cm)

PMMA).

The tube voltage was fixed at 120 kVp, and tube current was repeated from 440 mA down to 10 mA. With rotating X-ray on, the scan time was still 0.5 s, with large focal spot size and body bowtie filter. The slice collimation was chosen to be 4×0.625 mm, and the DAS gain was fixed at 5 for all acquisitions in this study.

Table C.2 Summary of CT techniques used (with varying tube current and fixed gain to collect data in service mode).

Parameters	Value or Status
Scan type	Rotating X-ray on
Scan time (s)	0.5
Gantry velocity (s/rot)	0.5
DAS gain	5
Filter	Body
Slice collimation (mm)	4×0.625
Calibration vector	Full
Tube voltage (kVp)	120
Tube current (mA)	440, 320, 240, 160, 80, 40, 20, 10

Results

Figure C.3 presents reconstructed images of data collected with service mode of fixed gain, with parameter settings listed in Table 4.8. As expected, image acquired at reduced tube current suffers more noise, which is visually apparent by comparison.

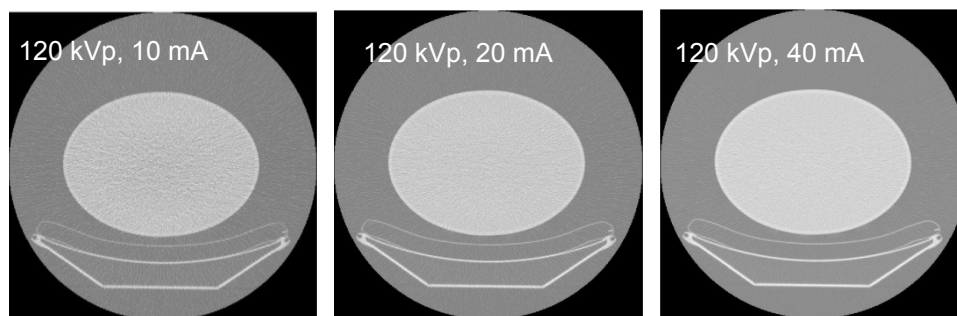


Figure C.3 Phantom based measured experiment result: Reconstructed CT images with data acquired in fixed gain service mode. (Left) 120 kVp, 10 mA; (Middle) 120 kVp, 20 mA; (Right) 120 kVp, 40 mA. From right to left, increased noise are visible with decreasing tube current. All images are reconstructed with slice thickness 0.625 mm, tube rotation time 0.5 s, and other tube parameters are listed in Table C.2.

3. *CT electronic noise measurement in service mode with fixed gain*

We were able to collect data of electronic noise on the DSTE PET/CT scanner and VCT scanner with water phantom and without phantom. More phantom-based measured experiments are needed for characterizing electronic noise and quantum noise model at low CT dose cases.

VITA

Ting Xia was born in Nanjing, Jiangsu Province, China. She obtained both of her Bachelor's and Master's degree in Biomedical Engineering in Southeast University, China. Her master's thesis was titled "Moment Functions and Their Applications in Image Analysis". In September 2006, she came to USA and began her Ph.D study at Bioengineering Department in University of Washington. She spent about 2 years in ultrasound imaging before she studied PET/CT imaging under supervision of Professor Paul Kinahan in Imaging Research Laboratory, Department of Radiology. In 2012, she earned a Doctor of Philosophy at University of Washington in Bioengineering. She now works as a reconstruction scientist in Toshiba Medical Research Institute USA, Inc. immediately after graduation.